

THE VIEWS AND CONCLUSIONS CONTAINED IN THIS DOCUMENT ARE THOSE OF THE AUTHORS AND SHOULD NOT BE INTERPRETED AS NECESSARILY REPRESENTING THE OFFICIAL POLICIES, EITHER EXPRESSED OR IMPLIED, OF THE DEFENSE ADVANCED RESEARCH PROJECTS AGENCY OR THE U. S. GOVERNMENT

EXCIMER LASER RESEARCH

J.H. Parks
AVCO EVERETT RESEARCH LABORATORY, INC.
2385 Revere Beach Parkway
Everett, MA 02149

Final Technical Report for Period 15 August 1974 to 29 September 1979

APPROVED FOR PUBLIC RELEASE; DISTRIBUTION UNLIMITED.

Sponsored by
DEFENSE ADVANCED RESEARCH PROJECTS AGENCY
ARPA Order No. 1806

Monitored by
OFFICE OF NAVAL RESEARCH
DEPARTMENT OF THE NAVY
Arlington, VA 22217

80 6 12 008

FOREWORD

DARPA Order No.: 1806

Program Code No.: 5E20

Name of Contractor: Avco Everett Research Laboratory, Inc.

Effective Date of Contract: 15 August 1974

Contract Expiration Date: 29 September 1979

Amount of Contract: \$1,146,990

Contract No.: N00014-75-C-0063

Principal Investigator and Phone No.: J.H. Parks
(617) 389-3000 Ext. 323

Scientific Officer: Director, Physics Program
Physical Sciences Division
Office of Naval Research
Department of the Navy
800 North Quincy Street
Arlington, VA 22217

Short Title of Work: Excimer Laser Research

UNCLASSIFIED

SECURITY CLASSIFICATION OF THIS PAGE (When Data Entered)

REPORT DOCUMENTATION PAGE		READ INSTRUCTIONS BEFORE COMPLETING FORM
1 REPORT NUMBER	2 GOVT ACCESSION NO.	3 RECIPIENT'S CATALOG NUMBER
	AD-A085520	
4 TITLE (and Subtitle)	5 TYPE OF REPORT & PERIOD COVERED	
EXCIMER LASER RESEARCH.	Final Technical Report. 15 Aug 74-29 Sep 79	
6 AUTHOR(s)	7 PERFORMING ORG. REPORT NUMBER	
J.H. Parks		
8 CONTRACT OR GRANT NUMBER(s)	9 PERFORMING ORGANIZATION NAME AND ADDRESS	
NO0014-75-C-0063, DARPA Order-1806	Avco Everett Research Laboratory, Inc. 2385 Revere Beach Parkway Everett, MA 02149	
10 PROGRAM ELEMENT, PROJECT, TASK AREA & WORK UNIT NUMBERS	11 CONTROLLING OFFICE NAME AND ADDRESS	
(11) 1979	Defense Advanced Research Projects Agency DARPA Order No. 1806	
12 REPORT DATE	13 NUMBER OF PAGES	
	147	
14 MONITORING AGENCY NAME & ADDRESS (if different from Controlling Office)	15 SECURITY CLASS. (of this report)	
Office of Naval Research Department of the Navy Arlington, VA 22217	Unclassified	
15a DECLASSIFICATION/DOWNGRADING SCHEDULE	16 DISTRIBUTION STATEMENT (of this Report)	
	Approved for public release; distribution unlimited.	
	17 DISTRIBUTION STATEMENT (of the abstract entered in Block 20, if different from Report)	
	18 SUPPLEMENTARY NOTES	
	19 KEY WORDS (Continue on reverse side if necessary and identify by block number)	
	Excimer Lasers Electron Beams Rare Gas Halides Mercury Halides Mercury Halide Radiative Lifetimes Interhalogens Rare Gas Metastable Photoionization Exciplex Laser Kinetics	
	20 ABSTRACT (Continue on reverse side if necessary and identify by block number)	
	This final report describes theoretical and experimental investigations of the rare gas monohalides, halogens, mercury monohalides and interhalogen molecules. These molecules show great promise for achieving high power scalable laser action in the near UV and visible portion of the spectrum. The report includes a description of fluorescence and lasing	

DD FORM 1473

EDITION OF 1 NOV 65 IS OBSOLETE

UNCLASSIFIED

SECURITY CLASSIFICATION OF THIS PAGE (When Data Entered)

048450

SECURITY CLASSIFICATION OF THIS PAGE(When Data Entered)

experiments for these molecules; an analysis of formation kinetics; and theoretical calculations of rare gas metastable photoionization and the mercury halide radiative lifetimes. A theoretical model has been developed to describe the excited ion-pair state structure of the rare gas halides and interhalogens. The predictions of this theory are borne out by fluorescence experiments.

Accession Per
NTIS GRA&I
DOI NTIS
Unannounced
JAN

1985
10/16/85
Special

A

SECURITY CLASSIFICATION OF THIS PAGE(When Data Entered)

TABLE OF CONTENTS

<u>Section</u>	<u>Page</u>
List of Illustrations	3
I. INTRODUCTION	7
II. RARE GAS HALIDE RESEARCH	13
A. Experimental Apparatus	13
B. Rare Gas Halide Spectroscopy	19
1. Fluorescence Spectra	19
2. Laser Spectra	28
C. Structure of the Rare Gas Halides	31
D. Rare Gas Halide Kinetics	40
III. HALOGEN RESEARCH	47
A. Iodine	47
IV. MERCURY HALIDE RESEARCH	55
A. Experimental Apparatus	55
B. Mercury Halide Spectroscopy	62
C. Halogen Donor Selection	68
D. Mercury Halide Lasers	72
1. Mercury Chloride	72
2. Mercury Bromide	77
E. HgX* Formation Kinetics	83
1. Ion-Ion Recombination	83
2. Exchange Reactions and Interception	83
3. Neutral Channels	87
4. HgX* Intrinsic Efficiency	88
V. THEORETICAL EFFORT	91
A. Rare Gas Metastable Photoionization	91
B. Mercury Halide Radiative Lifetimes	101

<u>Section</u>	<u>Page</u>
VI. INTERHALOGEN RESEARCH	109
A. Criteria for Laser Candidates	109
B. Interhalogen Spectroscopy	119
C. Interhalogen Kinetics	132
1. Ion Formation Channel	132
2. Neutral Formation Channel	135

LIST OF ILLUSTRATIONS

<u>Figure</u>		<u>Page</u>
1	Molecular Energy Level Diagram Illustrating the Principle of an Excimer Laser	8
2	Photograph of the AERL High Intensity E-Beam Gun	14
3	Cross-Sectional View of the High Intensity E-Beam Gun and Laser Cell	15
4	Schematic Diagram of Emission Diagnostics for Fluorescence Experiments	16
5	Microdensitometer Tracing of Spectral Plate of Spontaneous Emission Spectrum of XeI	20
6	Densitometer Trace of XeBr ($^2\Sigma \rightarrow ^2\Sigma$) Emission Spectrum	21
7	Densitometer Trace of XeCl ($^2\Sigma \rightarrow ^2\Sigma$) Emission Spectrum	22
8	Densitometer Trace of XeF ($^2\Sigma \rightarrow ^2\Sigma$) Emission Spectrum	23
9	Potential-Energy Curves for Xenon Fluoride	26
10	Comparison of Spontaneous and Laser Emission Spectra from KrF	29
11	Comparison of Spontaneous and Laser Emission Spectra from XeCl	30
12	Schematic of Rare Gas Monohalide Potential Energy Curves	32
13	Potential Energy Diagram Showing the Structure of Xenon Iodide	34
14	Estimated Potential Curves for XeBr Showing the Possibility of Strong Absorption Band Overlapping the Lasing Transition	38

<u>Figure</u>		<u>Page</u>
15	Potential Curves for I_2 Showing Electronic States Relevant to the Laser Transition	48
16	Densitometer Tracings of I_2 Emission Produced when Ar/HI Mixtures are Excited with an E-Beam	50
17	Oscillograms of the Photodiode Viewing the Laser Output and the Voltage Pulse Producing the E-Beam	51
18	E-Beam/Laser Cell Configuration Indicating Transverse Beam Excitation	56
19	Aluminum Laser Cell Showing Cartridge Heater Arrangement, Cavity and Window Configuration	57
20	Heated Mirror Assembly	58
21	Laser Gas Bottle Oven	59
22	Overview of Experimental Apparatus	60
23	E-Beam Cathode	61
24	$HgCl^*$ Fluorescence Spectrum	63
25	$HgBr^*$ Fluorescence Spectrum	64
26	Fluorescence Spectra for Various Rare Gas/ Hg/CCl_4 Mixture Compositions	65
27	Fluorescence Spectra for Various Rare Gas/ Hg/HBr Mixture Compositions	66
28	Fluorescence Spectra for Various Rare Gas/ Hg/HI Mixture Compositions	67
29	Discharge Pumping Donor Energetics - $HgCl^*$	70
30	Estimated Potential Curves for $HgCl$	73
31	Estimated Potential Curves for $HgBr$	74
32	Mercury Chloride Laser Emission and Spontaneous Emission Spectra	75
33	$HgCl$ Data Oscillogram Trace Showing the E-Beam Voltage Pulse and the Corresponding Photodiode Laser Signal for (a) Output Coupling $T = 50\%$; (b) Output Coupling $T = 0.35\%$	76

<u>Figure</u>		<u>Page</u>
34	Mercury Bromide Laser Emission and Spontaneous Emission Spectra	80
35	HgBr Data Oscillogram Trace Showing the E-Beam Voltage Pulse and the Corresponding Photodiode Laser Signal	81
36	Ion-Ion Recombination Channel Suggested for HgCl^* Formation in Ar/Xe/Hg/CCl_4 Mixtures	85
37	HgCl^{+*} Formation via Exchange Reactions in Ar/Xe/Hg/CCl_4 Mixtures	86
38	Suggested Formation Channels for Dominant Species which Absorb at the Laser Wavelength λ_L in Ar/Xe/Hg/CCl_4 Mixtures	89
39	Partial Energy Level Diagrams for Argon and Krypton	92
40	Photoionization Cross Sections for the Ar^* State, $\sigma(4s)$, and the Ar^{**} State, $\sigma(4p)$	96
41	Photoionization Cross Sections for the Kr^* State, $\sigma(5s)$ and the Kr^{**} State, $\sigma(5p)$	97
42	Absorption Length at $\lambda = 2486 \text{ \AA}$ vs Total Excited-State Number Density	100
43	$B \rightarrow X$ Radiative Lifetime of HgX^* as a Function of the Ionic Mixing Coefficient, β	107
44	Estimated Potential Curves for KrF	114
45	Estimated Potential Curves for HgCl	115
46	Estimated Potential Curves for ArI	117
47	Morse Potential Energy Functions for ICl	121
48	Morse Potential Energy Functions for BrCl	122
49	Approximate Potential Energy Curves for IBr	123
50	Estimated Potential Curves for ICl	129

<u>Figure</u>		<u>Page</u>
51	E-Beam Excited ICl* Fluorescence	130
52	E-Beam Excited BrCl* Fluorescence	131
53	Estimated Potential Curves for ArI	133
54	Predicted Neon Halide Predissociation	134

I. INTRODUCTION

The primary objective of the DARPA-sponsored laser research program at AERL (Contract No. N00014-75-C-0063) has been to identify lasers in the visible to near ultraviolet wavelength range which offer the capability for:

- long-range propagation
- volumetric scaling to high-average power
- high-efficiency operation ($\eta \gtrsim 5 - 10\%$)

In addition to long-range applications, improved visible and ultraviolet lasers would find a variety of other uses, both military and non-military. In fact, some of these uses would have much less severe performance requirements than those described above. Military applications include optical radar, remote atmospheric and meteorological measurements using Raman backscatter, and oceanographic measurements using wavelengths in the blue-green portion of the spectrum. Non-military applications include laser pellet fusion, isotope separation, and laser-induced chemistry.

Among the ideas which have been proposed, excimer lasers stand out since they offer rapid, volumetric removal of the lower laser level. The basic principle of a so-called excimer laser is illustrated in Figure 1. The two species A and B are repulsive or, at most, weakly bound in their ground states. However, when one of them (specie A) is raised to an electronically excited state it can combine with the other species to form an excited dimer (or "excimer") AB^* . This molecule can then radiate, or lase, to the ground state, as indicated, whereupon it immediately falls apart on time scales of the order 10^{-12} sec, removing the lower laser level and assuring an inversion from excimer transitions. If the lower laser

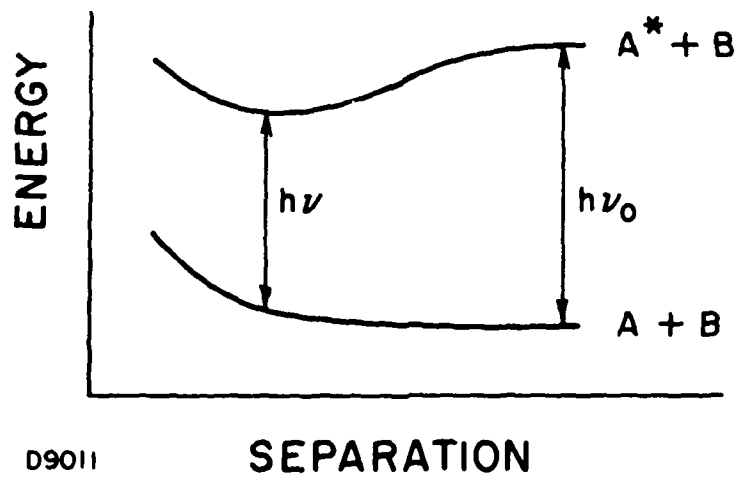


Figure 1. Molecular Energy Level Diagram Illustrating the Principle of an Excimer Laser

level is rapidly removed, large intra-cavity fluxes can be used to efficiently extract every upper laser level formed in the pumping sequence. In this fashion, maximum efficiency can be attained within the limits of kinetic branching ratios and quantum efficiencies with which the upper level is formed.

Ordinarily, excimer emission is rather broadband since it corresponds to a bound-free or bound-weakly bound transition. Consequently, the simulated emission cross section is relatively small ($\sim 10^{-18} - 10^{-19} \text{ cm}^2$), even for allowed transitions, and enormous pumping rates are required to achieve useful gain. The principal achievement in the DARPA-sponsored AERL laser research program has been the demonstration of a new class of excimer lasers. The excimer transition in these lasers is characterized by structured emission having strong stimulated emission cross sections ($\sim 10^{-16} \text{ cm}^2$) which provide the opportunity for efficient laser operation.

These new laser molecules have an excited state AB^* which is described physically as a bound ion pair A^+B^- in which the B atom is a halogen ($B = F, Cl, Br, I$). These characteristics have several important consequences which lead to potential high-efficiency, high-powered scalability of these lasers. To summarize, the ion pair A^+B^-

- can be selectively excited by direct e-beam or discharge pumping by efficient reaction kinetics, and
- can be formed in a discharge which is stabilized by the presence of the halogen atom B.

The possibility of pumping via a stabilized discharge allows

- optimum matching of electrical circuitry to the constant impedance laser load, thus optimizing overall efficiency,
- volumetric scalability which can be achieved utilizing e-beam ionization of the discharge medium,
- a greater pulse repetition frequency than a pure e-beam device.

Exploratory research at AERL has identified four new classes of lasers which have wavelengths in the 200-550 nm range. The lasers are based on molecules having excited ion pair states which serve as the upper laser level. Depending on the specific molecule, the lower laser level is either dissociative, weakly bound, or collisionally quenched. The four classes include:

- Rare Gas Halides
- Halogens
- Mercury Halides
- Interhalogens

This final report will review the research performed and accomplishments achieved for each class of laser molecule.

Lasers which have been demonstrated at AERL under this contract and in other laboratories are shown in Table 1. The AERL research effort has been three pronged. First, a basic theoretical and experimental understanding of the new molecules has been achieved under this contract by studying the kinetics and spectroscopy of these species. Second, lasing experiments, using e-beam excitation, have been performed under this contract to demonstrate laser candidates and optimize the laser efficiency. Thirdly, research on electric discharge pumping techniques under other AERL/DARPA contracts has been closely coupled with the molecular research to find scalable means to excite these systems. This approach has yielded the following significant results: laser action was first demonstrated on XeF (335 nm),⁽⁶⁾ XeCl (308 nm),⁽⁴⁾ KrF (248 nm),⁽⁴⁾ I₂ (342 nm),⁽¹⁰⁾ HgCl (558 nm)⁽¹²⁾ and HgBr (502 nm)⁽¹³⁾ at AERL; an accurate, predictive, experimentally verified model has been developed to describe the chemical binding and spectroscopy of the rare gas halides^(17,18) and the interhalogen transitions; the first electric discharge pumped KrF laser was developed at AERL;⁽¹⁹⁾ an accurate model has been developed

TABLE 1. A SUMMARY OF EXCIPLEX LASERS AND
THEIR LASING WAVELENGTHS

CLASS	MOLECULE	AERL	λ (nm)	REFERENCE
RARE GAS HALIDE	ArF		193	1
	KrCl		222	2, 3
	KrF	•	249	4
	XeBr		282	5
	XeCl	•	308	4
	XeF	•	351	6
			500	
HALOGEN	F ₂		158	8
	Br ₂	•	292	9
	I ₂	•	342	10
MERCURY HALIDE	HgI		440	11
	HgBr	•	502	12
	HgCl	•	558	13
INTERHALOGEN	ClF		284	14
	IF		491	15

J4217

to describe the KrF laser discharge;⁽²⁰⁾ an analysis of discharge stability in such systems has been given;⁽²¹⁾ high intrinsic efficiency has been demonstrated for KrF,⁽²²⁾ and more recently on XeF;⁽²³⁾ the scaling laws for the direct e-beam pumped KrF laser have been successfully demonstrated;⁽²⁴⁾ discharge pumping of the Br₂ laser has been demonstrated under IR&D funding⁽²⁵⁾ and a sound understanding of the kinetics for both rare gas halides and halogen lasers is emerging. Under this contract, theoretical calculations of photoabsorption loss processes in discharge excited noble gases; and radiative lifetimes of the mercury halides have been performed.

The significance of the AERL effort lies in the fact that this new class of lasers offers the potential of both high overall electrical efficiency ($\geq 10\%$) and high average laser power. It is relevant to indicate the utility which these lasers have shown to fulfill various DOD and DOE program requirements. The KrF* laser has demonstrated $\sim 10\%$ intrinsic efficiency and is currently under DOE development to satisfy laser fusion driver system requirements of 1-4 MJ energies at overall efficiencies of $\sim 5\%$. The XeF* laser has demonstrated $\sim 6\%$ intrinsic efficiency and is currently under DARPA technology development for scale-up to large single-pulse energies and repped-pulse operation. This work will be a significant stepping stone to the first high efficiency, high average power short wavelength laser. The HgBr* laser has demonstrated $\sim 1\%$ intrinsic efficiency and XeCl* $\sim 5\%$ intrinsic efficient; both are leading candidates in DARPA repped-pulse development programs for sea water propagation applications. High-repetition rate KrF* and XeF* lasers at $\sim 5-10$ kHz are under development for Los Alamos Scientific Laboratory and Lawrence Livermore Laboratory to provide laser capabilities for isotope separation.

II. RARE GAS HALIDE RESEARCH

A. EXPERIMENTAL APPARATUS

The experimental results observed at AERL were obtained with a high-intensity e-beam which was used to pump high-pressure mixtures of Ar, Xe and the halogens. The e-beam gun is shown in Figures 2 and 3. The e-beam produced by this gun has an energy of ~ 400 keV/electron, and an intensity of about 30 A/cm^2 passing through the foil, over an area of $\sim 1 \text{ cm}$ by 15 cm . For laser experiments the intensity is increased to about 150 A/cm^2 through the foil at the expense of lowering the energy to about 300 keV/electron. The duration of the e-beam pulse is $\sim 100 \text{ ns}$, with a 10 ns risetime and a 20 ns fall time. The gun has proved to be very reliable, and dozens or hundreds of shots are generally obtained between foil failures.

The cell is mounted directly on the e-beam gun as shown in Figure 4. Several cells are available, including stainless steel cells with brazed sapphire windows capable of operating at temperatures up to 900°F and pressures up to 100 psia . In the present experiment an aluminum cell is used which is compatible with fluorine. The valves are stainless steel and the windows are sapphire or quartz. For maximum reliability, a 0.001 in stainless steel foil is generally used. Titanium is corroded by the halogens and aluminum is not as strong as stainless steel. However, for maximum e-beam transmission, aluminized kapton films are used. The cell can be warmed up using built-in cartridge heaters to provide a mild bakeout. The cell can be pumped out to an ultimate vacuum of better than 10^{-5} Torr with a leak rate better than 10^{-4} Torr/hr. Therefore, purity is not a problem.

The gases, except I_2 vapor, are premixed in stainless steel tanks and allowed to stand for several hours, or even several days,

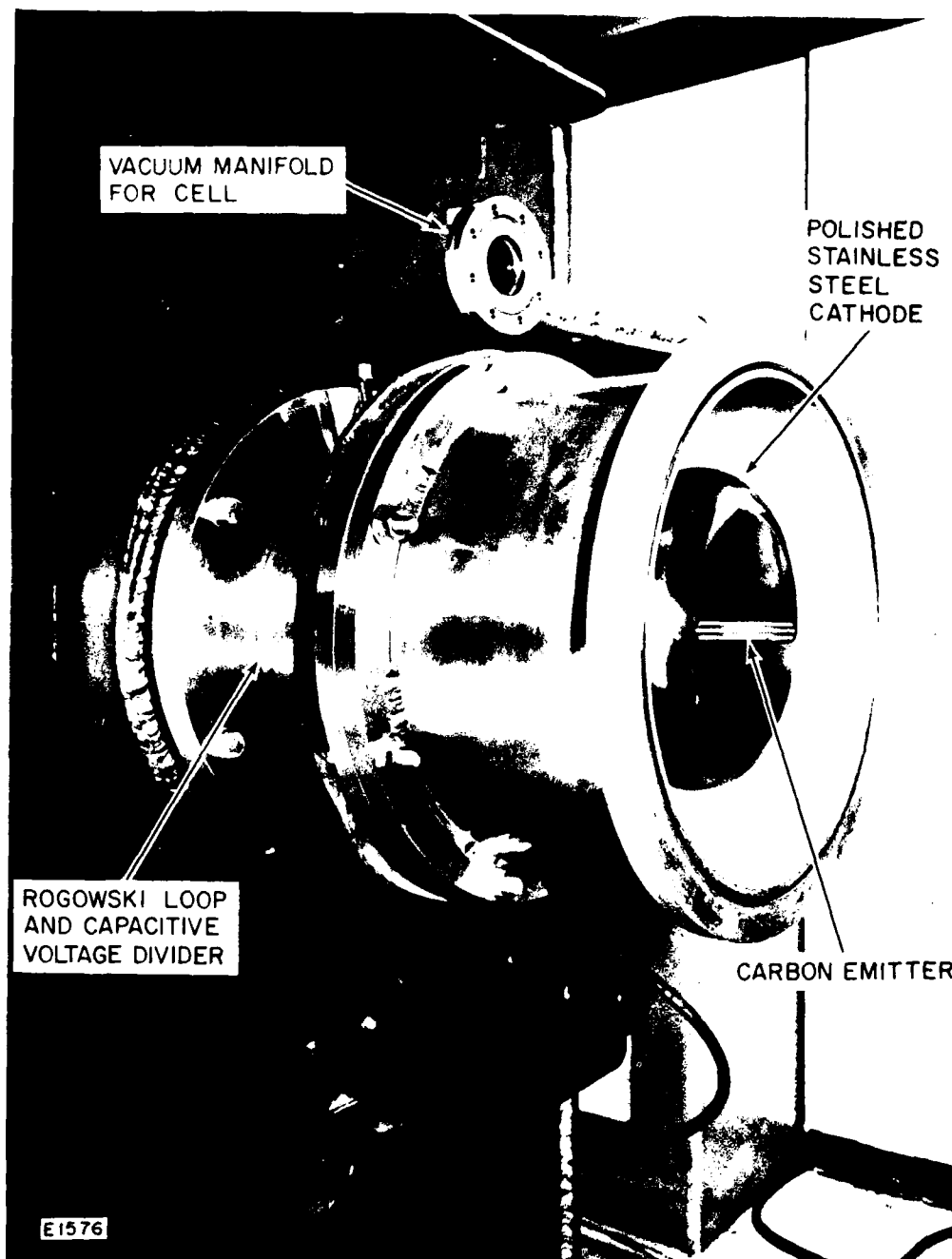


Figure 2. Photograph of the AERL High Intensity E-Beam Gun

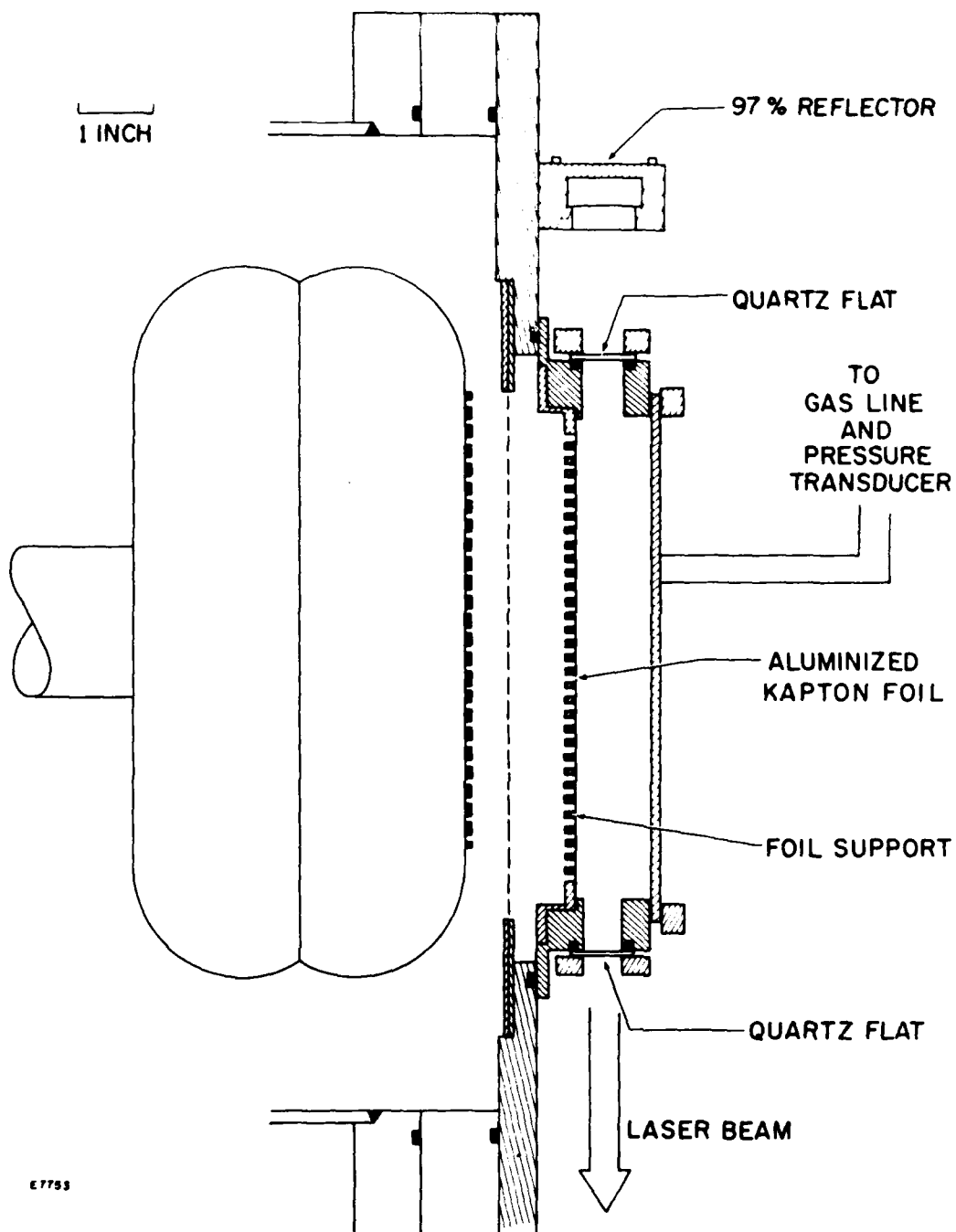


Figure 3. Cross-Sectional View of the High Intensity E-Beam Gun and Laser Cell

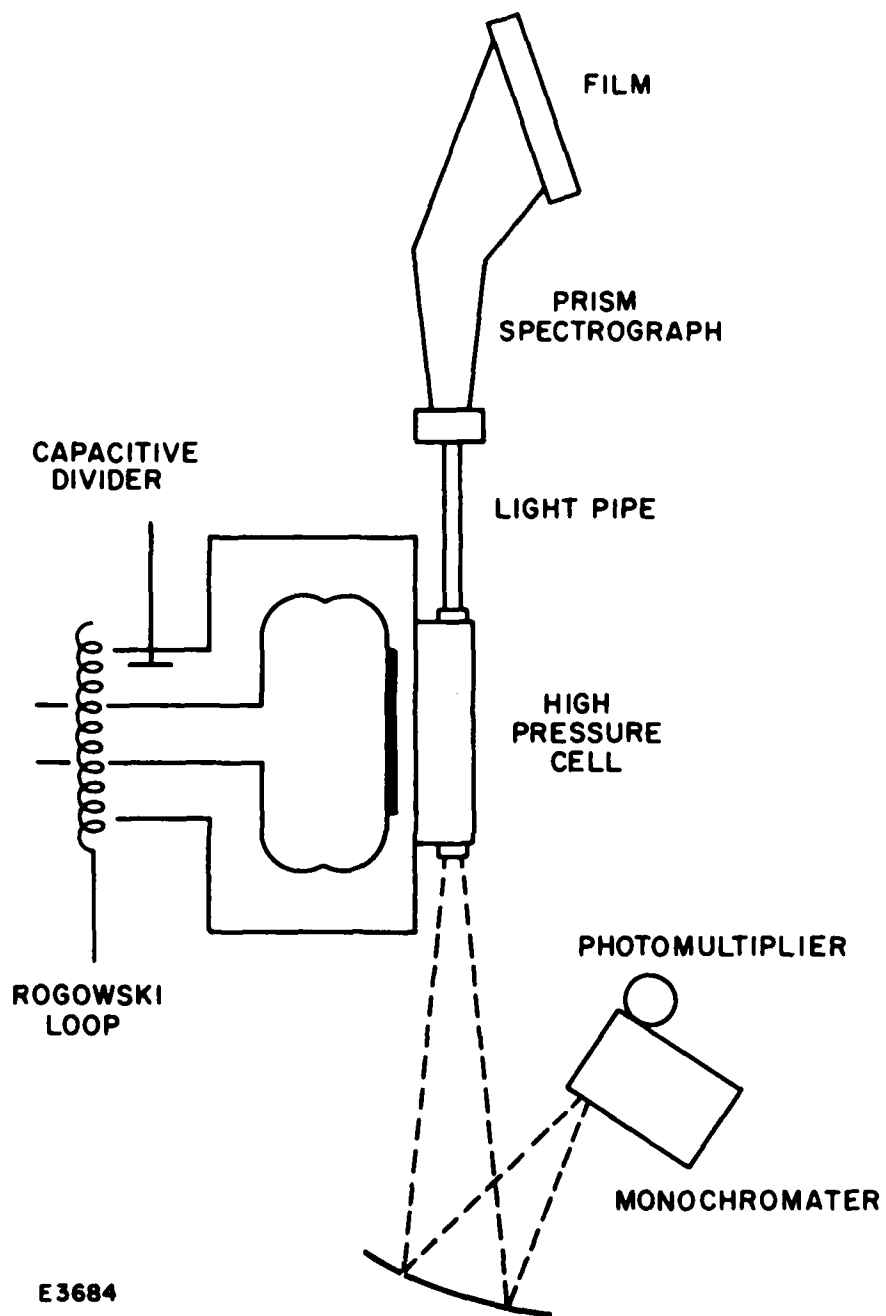


Figure 4. Schematic Diagram of Emission Diagnostics for Fluorescence Experiments

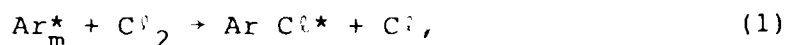
to assure that they are fully mixed when they are used. The iodine crystals were obtained from Merck and are claimed to be > 99% pure. They were placed in a small stainless steel sample cylinder attached to the cell through a stainless steel valve. The crystals and sample cylinder were repeatedly allowed to out-gas at room temperature (under vacuum but valved off) and then cooled with liquid N_2 and pumped out. The I_2 vapor is introduced directly into the evacuated cell and allowed to come into equilibrium. The rare gases are then admitted to the desired pressure and allowed to mix. Mixing is occasionally stimulated by firing the e-beam gun to warm the gas in the irradiated region. The liquid bromine was similarly outgassed by repeated freeze, pump, thaw cycles. Prior to making the measurements with F_2 , the cell and mixing manifold were passivated by filling them with an F_2 -rich mixture at low pressure (a few Torr to half an atmosphere) for several hours.

The diagnostics, shown in Figure 4 include time-integrated and time-resolved emission measurements, as well as laser absorption measurements. The time-integrated emission measurements are made with quarter-meter and half-meter Hilger quartz prism instruments, using film. Generally, at high pressures, one shot is sufficient to provide a medium resolution spectrum using 50 μm slits. This corresponds to a wavelength resolution of ~ 0.1 nm. The time-resolved emission measurements are made with a Jarrel-Ash one-quarter meter f/3.5 Ebert monochromator with a 1P28 photomultiplier tube, and Tektronix 551 oscilloscopes with type K and L preamps. The spectral resolution of this system is about 0.1 nm. The time resolution is limited by the oscilloscopes to ~ 10 ns. To provide an adequate signal-to-noise ratio, it has been found necessary to provide adequate lead shielding around the photomultiplier to screen out X-rays. In addition, it has been necessary to place the oscilloscopes in a screen room and provide careful grounding and shielding of the photomultiplier. Because of the intense emission observed from the rare gas halides it has been found necessary to take extreme care to prevent saturation of the photomultiplier.

Finally, laser optics and alignment equipment are available for laser experiments. The optical cavity consists of two high-reflectivity mirrors separated by about 25 cm. A stable resonator configuration is used in which one mirror has a 1 m radius of curvature and the other is flat. To reduce the losses, the normal incidence windows are aligned with the cavity. The alignment is carried out with a Davidson Optronics alignment telescope. Alignment accuracy of about 0.1 mrad is easily achieved, although much larger misalignments have no observable effect on the results.

B. RARE GAS HALIDE SPECTROSCOPY

The spectra of these molecules were first observed in low pressure flowing afterglows by Setser⁽²⁶⁾ and by Golde and Thrush.⁽²⁷⁾ In these experiments Cl_2 was mixed with Ar which had been previously excited by means of a microwave discharge. The rare gas halides were then formed by the reaction



where Ar_m^* is a metastable state of Ar. The emission from the excited ArCl^* was observed to be very bright, leading Golde and Thrush to estimate that the efficiency for producing the excited state was "more than, and possibly much more than, 10%." However, because of its short wavelength (170 nm) ArCl itself did not seem to be an interesting molecule. At this point, a theory was developed at AERL to predict the wavelengths at which the other rare gas halides should emit.⁽¹⁷⁾ Subsequent experiments carried out at AERL and elsewhere⁽²⁸⁾ substantially confirm the theoretical predictions. This section will review the spectroscopic measurements carried out under this contract which characterize the fluorescence and lasing spectra of the rare gas halide molecules.

1. Fluorescence Spectra

Some results of the time-integrated spectral measurements are shown in Figs. 5 through 8. In the XeI spectrum, Figure 5, we see the $^2\Sigma \rightarrow ^2\Sigma$ transition sharply peaked at about 254 nm, and shading off toward the blue with little structure. The broad, smooth $^2\Sigma \rightarrow ^2\Pi$ transitions are also evident at 325 and 360 nm. In the XeBr spectrum, Figure 6, we see the $^2\Sigma \rightarrow ^2\Sigma$ band sharply peaked at 282 nm. This band shades off toward the blue with a diffuse vibrational structure superimposed on the continuum. In the XeCl spectrum, Figure 7, the $^2\Sigma \rightarrow ^2\Sigma$ band peaks at 308 nm, and shades off toward the blue with a sharper vibrational structure. From the separation of the vibration peaks we find that

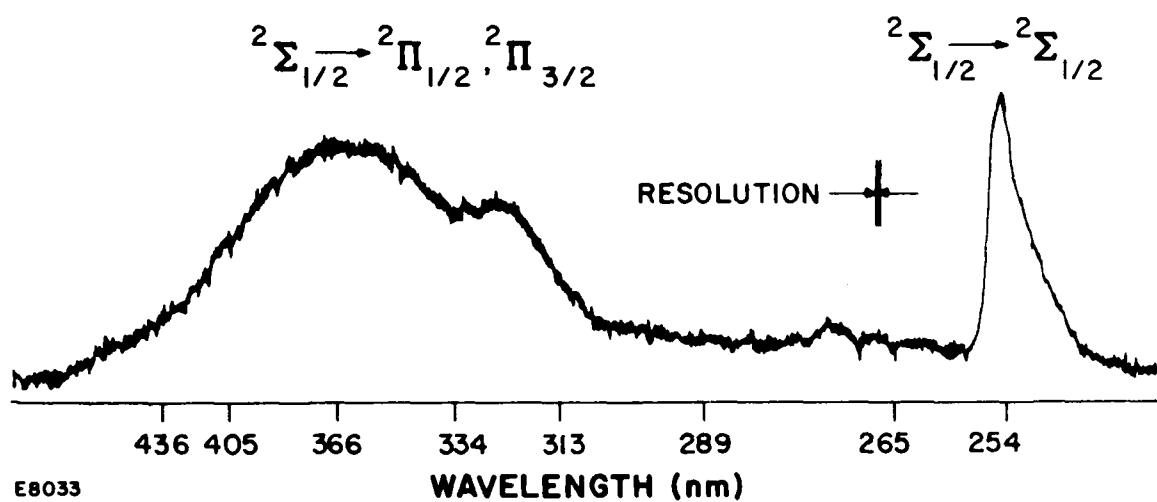


Figure 5. Microdensitometer Tracing of Spectral Plate of Spontaneous Emission Spectrum of XeI. The proposed broadband lasers for XeI would operate on the lower intensity bands assigned as $2\Sigma \rightarrow 2\Pi$.

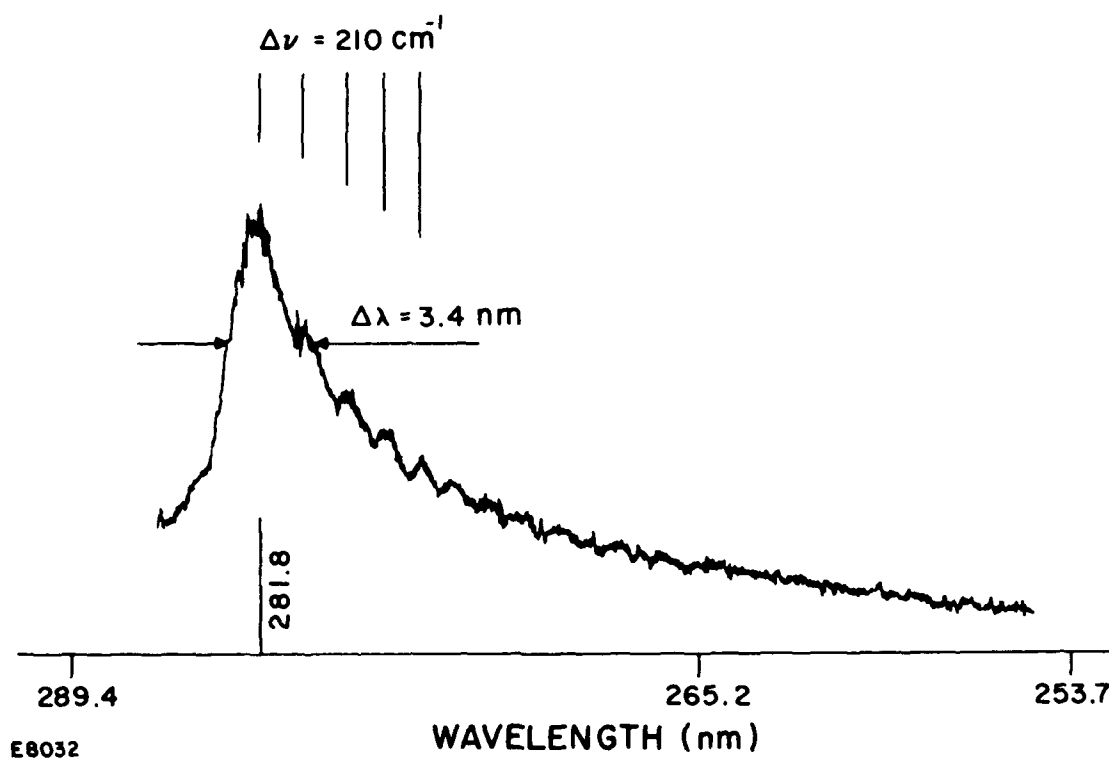
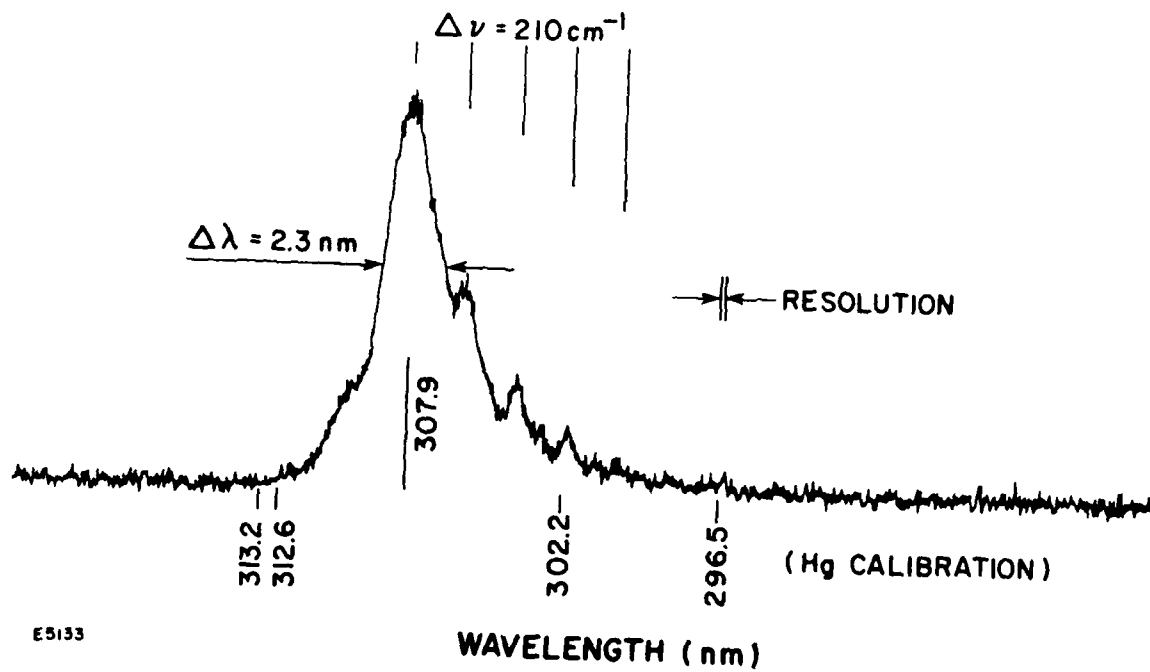


Figure 6. Densitometer Trace of XeBr ($^2\Sigma \rightarrow ^2\Sigma$) Emission Spectrum



E5133

Figure 7. Densitometer Trace of XeCl ($^2\Sigma \rightarrow ^2\Sigma$) Emission Spectrum

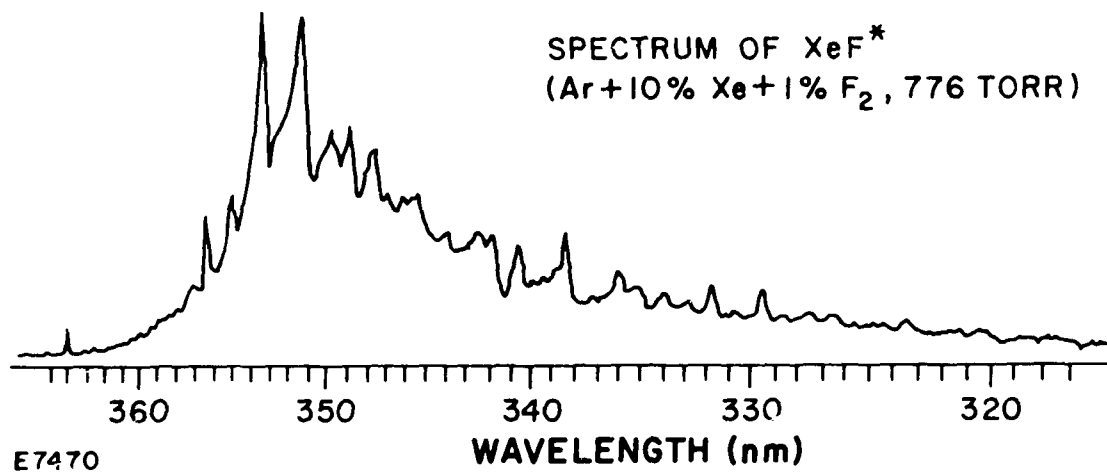


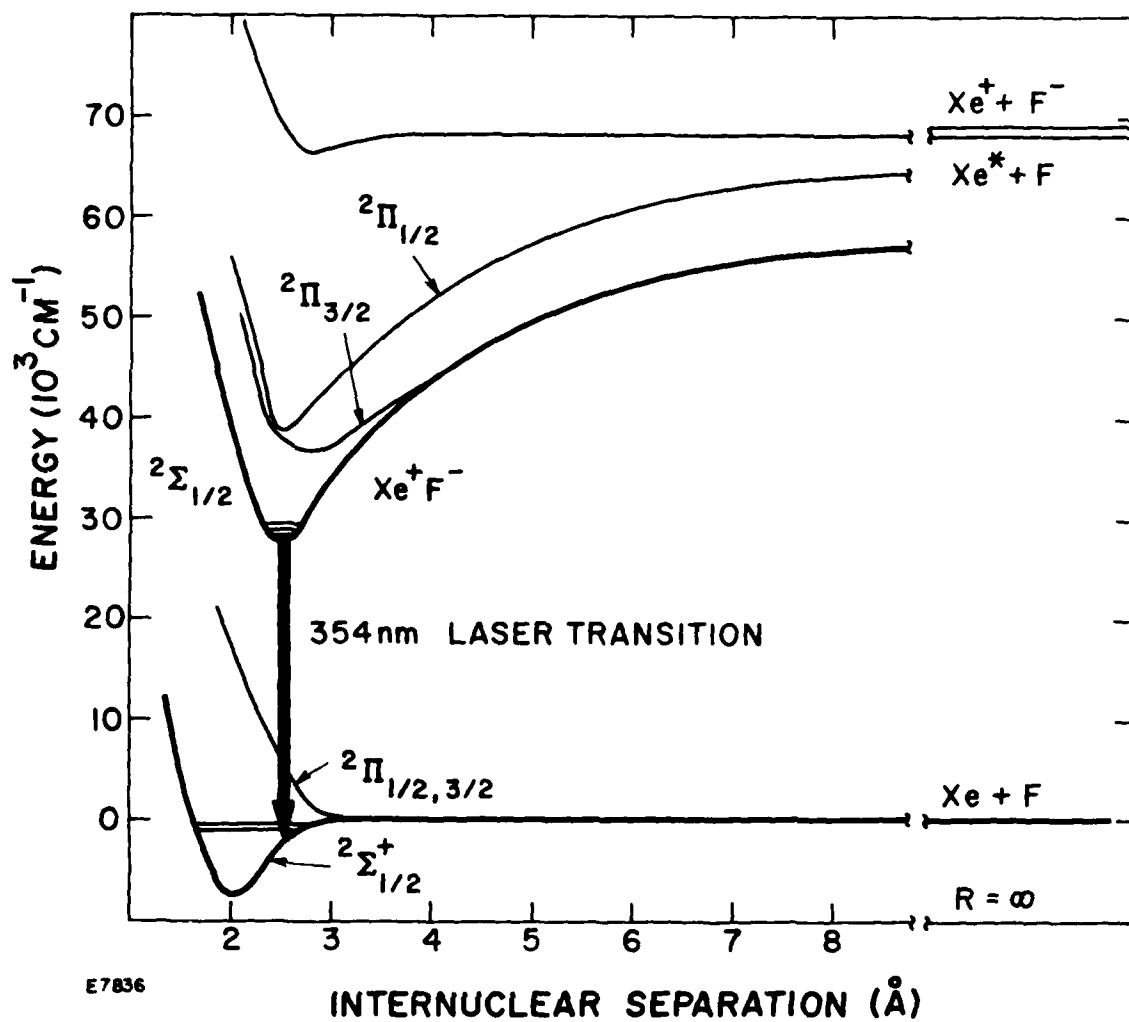
Figure 8. Densitometer Trace of XeF ($^2\Sigma \rightarrow ^2\Sigma$) Emission Spectrum

the vibrational spacing is $\sim 210 \text{ cm}^{-1}$. Since the vibrational spacing in cesium chloride is 209 cm^{-1} , this provides strong support for alkali halide model. The $2\Sigma \rightarrow 2\Sigma$ band of the XeF molecule, shown in Figure 8 peaks near 353 nm and shades off toward the blue. Although the broad structure of this band is similar to that of the $2\Sigma \rightarrow 2\Sigma$ bands of the other molecules, much more structure is evident. This is to be expected since XeF_2 , XeF_4 and XeF_6 are observed to be stable at room temperature.⁽²⁹⁾ Moreover, the predicted wavelength shown in Table 2 is too long for XeF. The shift corresponds to about 3000 cm^{-1} . This is less than the bond strength of XeF which is estimated to be between 3500 and 7000 cm^{-1} . The difference can be accounted for by assuming that the transition takes place to a high vibrational level of the ground electronic state, as shown in Figure 9. Further support for this conjecture comes from what is known, or can be estimated, regarding the bond lengths of the upper and lower electronic states. According to the alkali halide model, the bond length in the upper state should be about 2.3 \AA , whereas the observed bond length in XeF_2 is 2.0 \AA .⁽²⁹⁾ Because of its complexity, the vibrational structure of the $\text{XeF}(2\Sigma \rightarrow 2\Sigma)$ band emission is difficult to analyze. There appear to be two series of vibrational lines in XeF spectrum. Each series has a spacing of about 300 cm^{-1} and the two series are displaced with respect to each other by about 160 cm^{-1} . The conjecture is that the 300 cm^{-1} spacing represents the vibrational spacing of the excited XeF, while the 160 cm^{-1} spacing represents the vibrational spacing in the upper levels of the ground electronic state. The vibrational spacing in CsF is 365 cm^{-1} and the vibrational spacing in electronically excited XeF should be about the same, in fair agreement with the observed 399 cm^{-1} spacing. The vibrational level spacing of the $\text{XeF}_2(\nu_3)$ (asymmetric stretch) mode is 560 cm^{-1} .⁽²⁹⁾ However, the bond strength of XeF is expected to be quite a bit smaller and therefore the vibrational frequency should

TABLE 2. PREDICTED FEATURES OF INERT-GAS
MONOHALIDES FROM REF. 17

Molecule	$R_A(\text{\AA})^a$	$R_B(\text{\AA})^b$	$R_O(\text{\AA})$	$E_M(\text{cm}^{-1})$	$\lambda_1(\text{nm})$	$\lambda_2(\text{nm})$	$\lambda_3(\text{nm})^d$
XeI	19.2	6.3	3.3	39135	256	302	342
XeBr	32.0	15.9	3.	34272	292	354	407
NeCl	71.9	c	2.9	30860	324	402	417
NeF	39.6	c	2.35	25895	386	503	512
KrI	14.1	5.2	2.9	49353	302	231	252
KrCl	30.5	9.8	2.8	45592	219	253	258
KrF	22.7	c	2.27	39229	256	301	305
ArBr	17.0	3.2	2.8	62152	161	178	190
ArCl	24.1	4.5	2.7	58042	172	192	195
ArF	18.9	c	2.17	37484	190	214	218
NeF	9.6	2.6	1.93	93266	197	115	115

- R_A is the crossing radius of M^+X^- with $M^* + X$.
- R_B is the crossing radius of M^+X^- with $M + X^*$.
- These species have halogen excited-state levels only above the inert-gas excitation levels. Hence, no R_B crossing occurs.
- λ_3 is the predicted wavelength of the broadband terminating on the $2\pi 1/2$ lower state. For all but XeI, XeBr, KrBr, and KrI, the λ_2 and λ_3 bands are overlapped.
- For ArI, NeI, NeBr, NeCl, and the helium halides the inert-gas ionization potential is so large that the Coulomb curve does not made up sufficient energy to approach the low-lying halogen excited states. The compounds should only have small well depths and the molecular continua should be near the free atom lines. Possibly ionic states of opposite polarity, viz. $Ne^- + I^+$, could enter into the binding.



E7836

Figure 9. Potential-Energy Curves for Xenon Fluoride

be correspondingly smaller. Thus, the low value of the vibrational spacing in the ground electronic state may be accounted for by the relatively weak bond strength in XeF compared to XeF₂, and the high vibrational level to which the fluorescence takes place. The observed width of the vibrational peaks in the XeF spectrum is due to unresolved rotational structure. A theoretical rotational band profile corresponding to a single vibrational transition has been constructed using the estimated bond lengths for the upper and lower levels. Typically, near the center of the rotational band, the individual rotational lines are separated by $\sim 4 \text{ cm}^{-1}$. The pressure width of these lines at 1 atm is estimated to be $\sim 0.03 \text{ cm}^{-1}$, which is small compared to the rotational line spacing. However, the individual rotational levels will be split into six spin-orbit components. If the spin-orbit splitting is large compared to the pressure width of the lines, the resulting spectrum will be essentially a continuum. To estimate the stimulated emission cross section it will be assumed that the rotational band may be approximated by a structureless continuum. If the spin-orbit splitting is small compared with the pressure width of the rotational lines there will be spaces between the lines and the gain at the peak of the lines will be larger. Consequently, the gain calculated on the basis of a continuous rotation band provides a lower limit to the gain which might be expected.

A potential difficulty of the XeF system is the possibility of bottlenecking in the lower laser level. If the bond energy in the lower laser level is much greater than the temperature, dissociation from the lower laser level will not take place. On the other hand, if the emission takes place to a high vibrational level of the lower electronic state, vibrational relaxation to lower level vibrational levels may prevent bottlenecking. Using the semiempirical theory of Milikan and White⁽³⁰⁾ the relaxation time is estimated to be $\sim 30 \text{ ns-atm}$ for collisions with argon atoms. The vibrational relaxation time may be shorter than this

if vibration-rotation interaction is important. In fact, rotational relaxation itself may help relieve the bottlenecking problem.

2. Laser Spectra

The laser spectra and corresponding fluorescence spectra of KrF and XeCl are shown in Figures 10 and 11. The details of the laser characteristics are presented in Ref. 4.

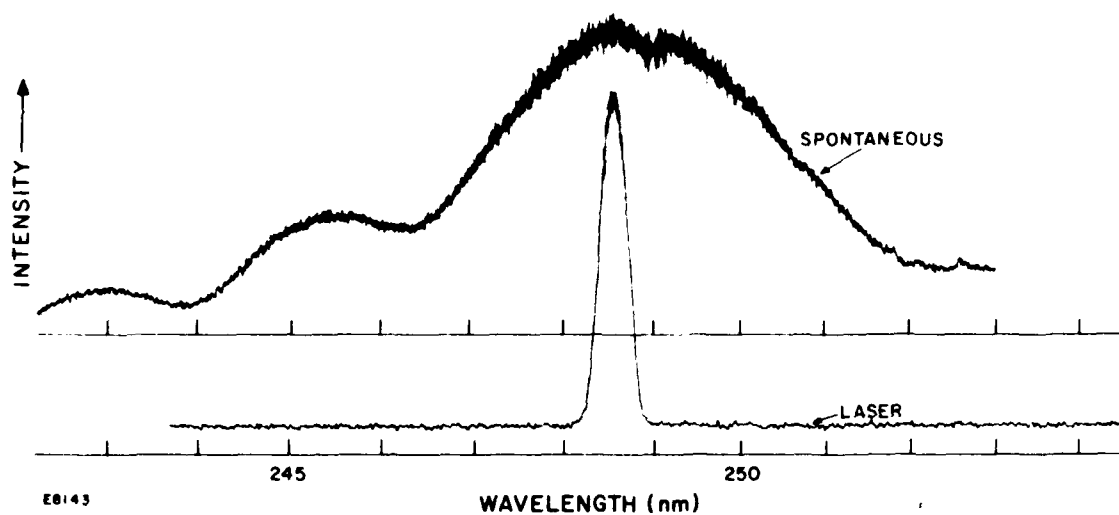


Figure 10. Comparison of Spontaneous and Laser Emission Spectra from KrF

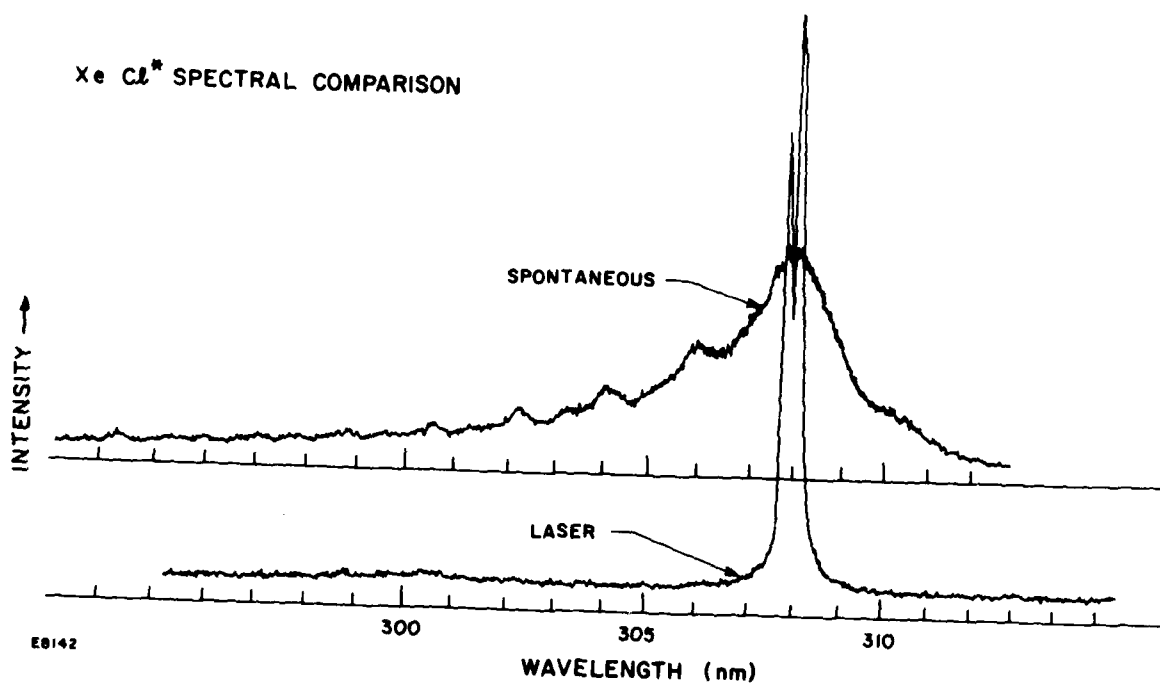


Figure 11. Comparison of Spontaneous and Laser Emission Spectra from XeCl

C. STRUCTURE OF THE RARE GAS HALIDES

Figure 12 shows a schematic molecular potential energy level diagram for a rare gas monohalide. One can see that these lasers utilize lower level dissociation. The upper laser level, denoted as MX^* , is bound with respect to dissociation into an inert gas atom M and an excited halogen atom, X^* . It is also bound with respect to $M^* + X$. The ionic nature of these excited states has been discussed. (17,18,28,31) The excited state is nothing more than a positively charged inert gas ion, M^+ , and a negative halogen ion, X^- , held together by coulombic rather than covalent forces. Predictions made at AERL under previous ARPA sponsorship of various properties of these excited species are based on the similarity of these excited states to the ionic ground states of the nearly isoelectric alkali halide ground states. (17) These predictions are accurate to within a few percent. (17,18,32) The similarity of the excited ionic states of the rare gas monohalides to ground state alkali halides derives from the fact that a rare gas halide ionic excited state differs by only one electron from an alkali halide. KrF^* is simply the ion pair Kr^+F^- . Kr^+ is only different by one electron from Rb^+ . Thus, the properties of KrF^* are very close to those of the ionic RbF molecule. A number of other useful analogies exist as well. For instance, the rare gas excited states, such as Kr^* , have low ionization potentials and as a result the chemistry of Kr^* , both kinetically and generically, is very similar to that of Rb .

MX^* has its potential minimum at a radius R_0 , and can radiate to lower states that derive from the collision of ground state M and X atoms. Predicted estimates of R_0 and other features of the class of rare gas halides are given in Table 2. For the schematic potential curve shown in Figure 12, emission is centered near two wavelengths, λ_1 and λ_2 . Two kinds of lower dissociative levels are shown, a $^2\Sigma$ state and a $^2\Pi$ state. This is the situation that applies for the collision of an atom with P symmetry and one atom

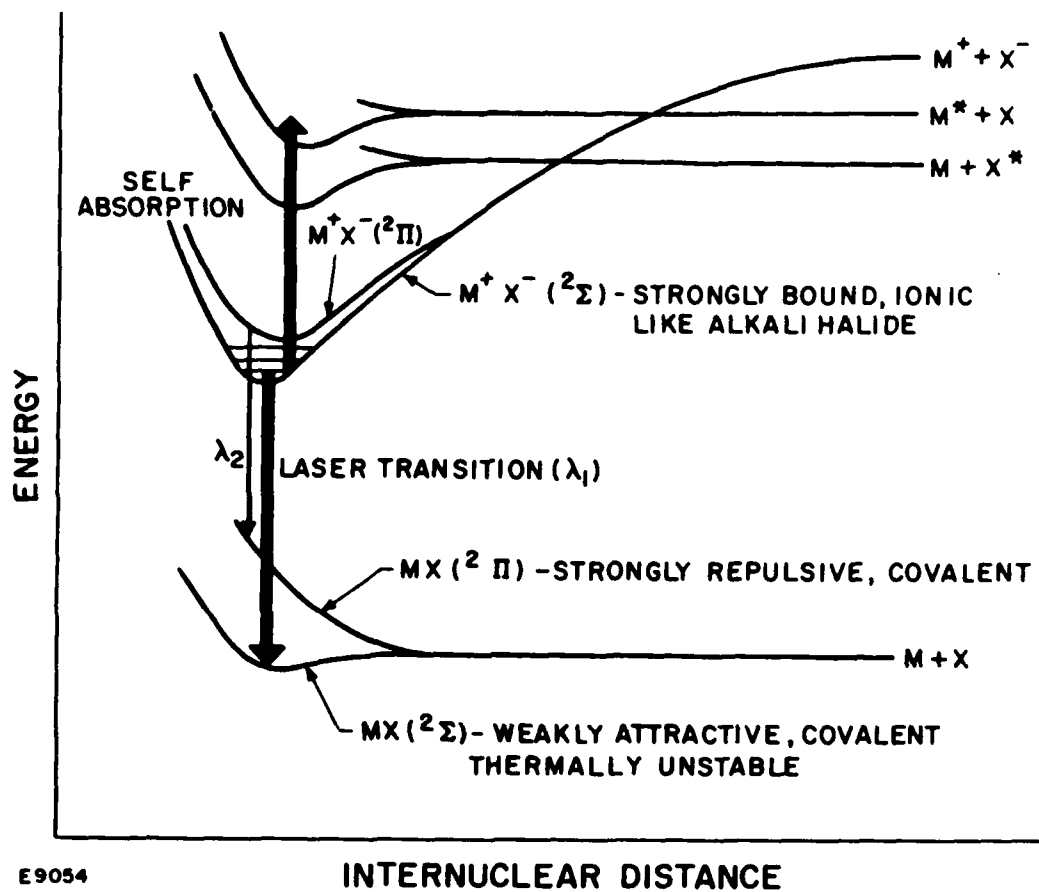


Figure 12. Schematic of Rare Gas Monohalide Potential Energy Curves

with S symmetry. Spin orbit effects are neglected but are important in rare gas bromides and iodides. The $^2\Sigma$ lower state corresponds to having one halogen "hole" in a p orbital on axis with the rare gas atom. The rare gas halide lasers demonstrated to date have terminated on this $^2\Sigma$ state. The $^2\Sigma$ state places the partially occupied p atomic orbital perpendicular to the molecular axis. The $^2\Pi$ state is strongly repulsive at the equilibrium internuclear configuration of MX^* , R_0 , because more electrons are between the halogen and rare gas nuclei. Emission terminating on the $^2\Pi$ states, near wavelength λ_2 , is characterized by a relatively broad continuum bandwidth. Figure 5 shows a microdensitometer trace of the XeI emission spectrum. Note the sharp $\Sigma \rightarrow \Sigma$ band and the two broad $\Sigma \rightarrow \Pi$ bands. Two broadbands are present because of the large spin orbit splitting of the low lying $^2\Pi$ states.

A potential energy diagram showing the structure of the XeI molecule is shown in Figure 13. It is typical of all the rare gas monohalides. At infinite internuclear separation the energy of $\text{Xe}^+ + \text{I} + e^-$ relative to $\text{Xe} + \text{I}$ is just the ionization potential of Xe, 12.127 eV. Due to the electron affinity of I_2 , 3.063 eV, the energy of $\text{Xe}^+ + \text{I}^-$ at infinite internuclear separation is 9.064 eV. As these particles approach one another they attract along a deeply descending coulomb curve which, as shown in Figure 13, crosses all the excited states of both Xe and I and is bound by 1.3 eV (relative to $\text{Xe} + \text{I}^*$) at an internuclear separation of 2.3 Å. On the other hand, the ground state of XeI is only weakly bound (XeF differs from the other monohalides in that its ground state is evidently more strongly bound). The strongest fluorescence band corresponds to the $^2\Sigma \rightarrow ^2\Sigma$ transition at 254 nm. This is an allowed transition with a lifetime estimated to be < 100 ns. This band is also the narrowest of the fluorescence bands since it corresponds to a bound-weakly bound transition. Since the lower level is split into Σ and Π branches broad, red-shifted bands appear at ~ 325 and 360 nm, corresponding to

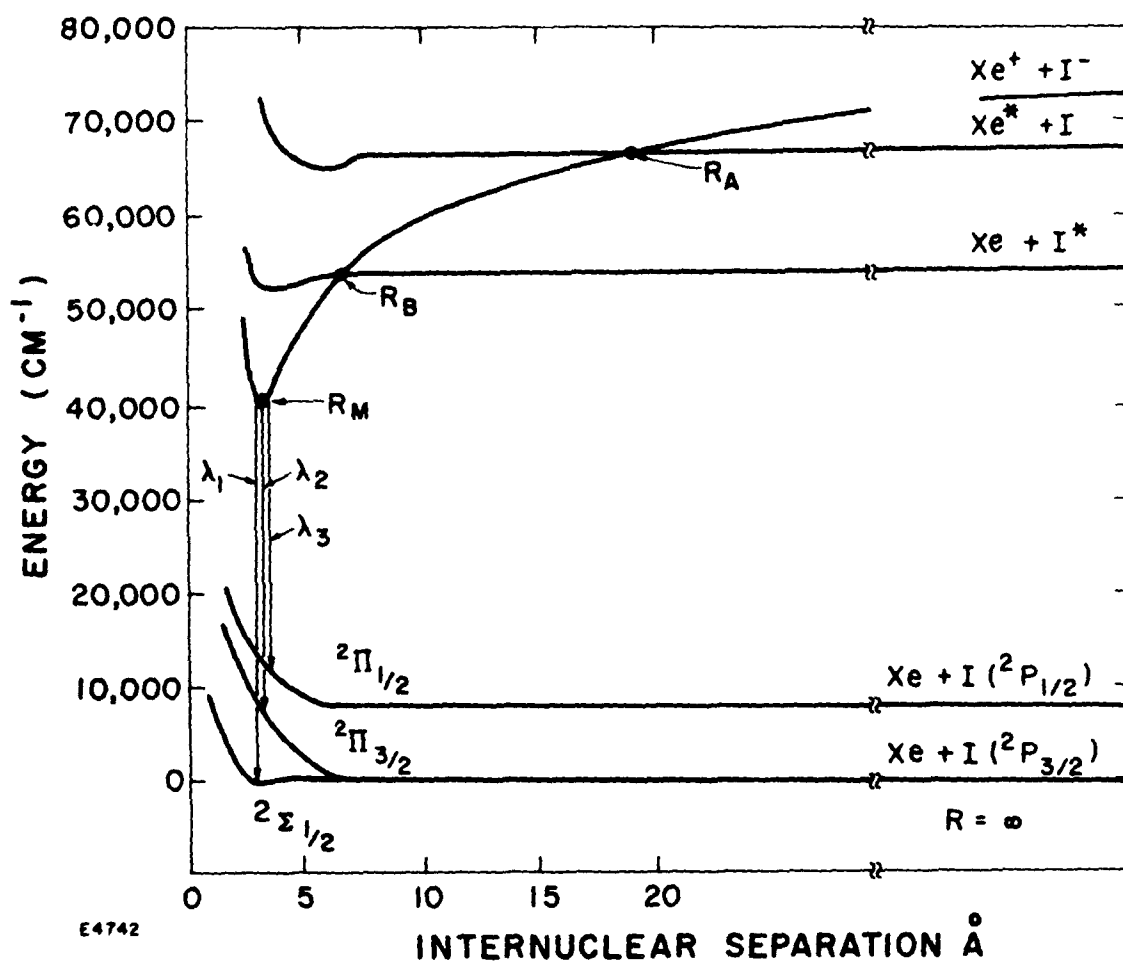


Figure 13. Potential Energy Diagram Showing the Structure of Xeon Iodide

the $2^1_1 \rightarrow 2^1_1$ transitions. Although it is not shown in Figure 2, the upper level is split in a manner similar to the lower level. This is because the Xe^+ ion has a 2^1P configuration similar to the ground state of the I atom. In the case of the Xe^+ ion, the $2^1\text{P}_{1/2}$ state lies ~ 1 eV above the $2^1\text{P}_{3/2}$ ground state. The 2^1_1 levels which arise from this splitting lead to emission which is blue shifted from the $2^1_1 \rightarrow 2^1_1$ transition. This emission has been observed weakly in XeF .

The success of the alkali halide model for the rare gas halides is shown by the comparison of existing data given in Table 3 to the predictions based on the model. Assuming comparable radiative transition rates to both states, the gain, assuming no excited state absorption on the transition near λ_1 will be higher on the $\Sigma \rightarrow \Sigma$ band because the bandwidth is narrower, explaining why existing rare gas monohalide lasers have operated on the sharper, higher gain bands.

The ionic excited state has 2^1_1 symmetry to a first approximation. Higher lying $2^1\Sigma$ ionic states are also present, and recent calculations by Dunning and Hay show that the substantial spin orbit coupling of Kr and Xe halides can mix these states with the lowest $2^1\Sigma_{1/2}$ ionic excited state.⁽³³⁾ Previously, concern that the upper laser level may not be the lowest ionic excited state had been expressed by several workers.^(34,35) A recent spectroscopic investigation⁽³⁶⁾ of the XeF 354 nm band has eliminated this earlier concern and now all workers in the field agree with the earlier assignments of high pressure rare gas halide spectra made at AERL.^(4,6,17,18)

The lowest $2^1\Sigma$ covalent state, the lower laser level for the existing lasers, is not truly dissociative for XeF and XeCl . The lasing transitions are, in fact, bound to bound^(18,36,37) for these species since these molecules have shallow wells in the lowest states. Recent molecular beam scattering experiments at Berkeley apparently show a chemical well depth in these species that is small but somewhat larger than that for a van der Waals interaction.⁽³⁷⁾ The binding of the XeF ground state was not

TABLE 3. COMPARISON OF SOME OBSERVED AND PREDICTED
FEATURES OF INERT GAS MONOHALIDES
(OBSERVED FEATURES SHOWN IN PARENTHESES)^a

Molecule	$R_M(\text{\AA})$	$E_M(\text{cm}^{-1})$	$\lambda_1(\text{nm})$	$\omega(\text{cm}^{-1})$
XeI	3.3	39135	256(254)	119
XeBr	3.1	34272	292(282)	150(180)
XeCl	2.9	30860	324(308)	214(210)
XeF	2.35	25195	397(353)	365
KrI	3.2	54000	185	138
KrBr	2.9	49353	203	170
KrCl	2.8	45592	219	233
KrF	2.27	39229	256(248)	370(400)
ArBr	2.8	62152	161	220
ArCl	2.7	58042	172(170)	280
ArF ^f	2.17	51679	193	430
NeF	1.93	93266	107	536

^aFrom Ref. 18.

anticipated theoretically.⁽³⁸⁾ However, recent calculations at NBS and IBM now give the slight binding ($\sim 700 \text{ cm}^{-1}$) observed in the beam experiments and derived from the XeF spectrum.⁽³⁹⁾

As seen in Figure 12, there are higher lying potential curves that derive from $M^* + X$ and $X^* + M$. Not drawn are the potential curves for the ion MX^+ , which are typically at higher energies. The exact energy and shape of the curves coming from $M^* + X$ has an important impact on the possibility of self absorption. Xenone bromide is probably a fine example of a rare gas halide that fluoresces very efficiently but lases very poorly.⁽⁴⁰⁾ This is probalby due to self absorption⁽²²⁾ as pictured in the potential curves given in Figure 14. Note that the self absorption is a photodissociation process rather than the photoionization which plagues the rare gas excimer lasers such as Xe_2^* . The positions of the upper and lower laser levels can be determined by the wavelength and shape of the XeBr^* emission bands. The exact R dependence of the upper potential curves and the wavelength dependence of the self absorption bands relative to the stimulated emission is not known. However, it is reasonably clear that absorption is possible in the XeBr^* case for the $2\pi \rightarrow 2\pi$ lasing transition. Rough consideration of the atomic orbitals that the electrons occupy in the various states suggests that absorption plays a major role in decreasing gain and efficiency in this system. Recall that the upper laser level is an ion pair Xe^+Br^- . In making a transition to the lower laser level, an electron hops out of a p orbital of Br^- into the lowest vacant orbital of Xe^+ , a 5 p orbital. This produces ground state Xe and Br atoms. However, in making a transition upward to $\text{Xe}^* + \text{Br}$, the electron hops from Br^- into a large 6s orbital of Xe. By virtue of the fact that the final electron orbitals centered on xenon for states of Xe^* are larger than those in which a ground state Xe atom is produced, one expects that the total transition dipole moment for absorption is larger than that corresponding

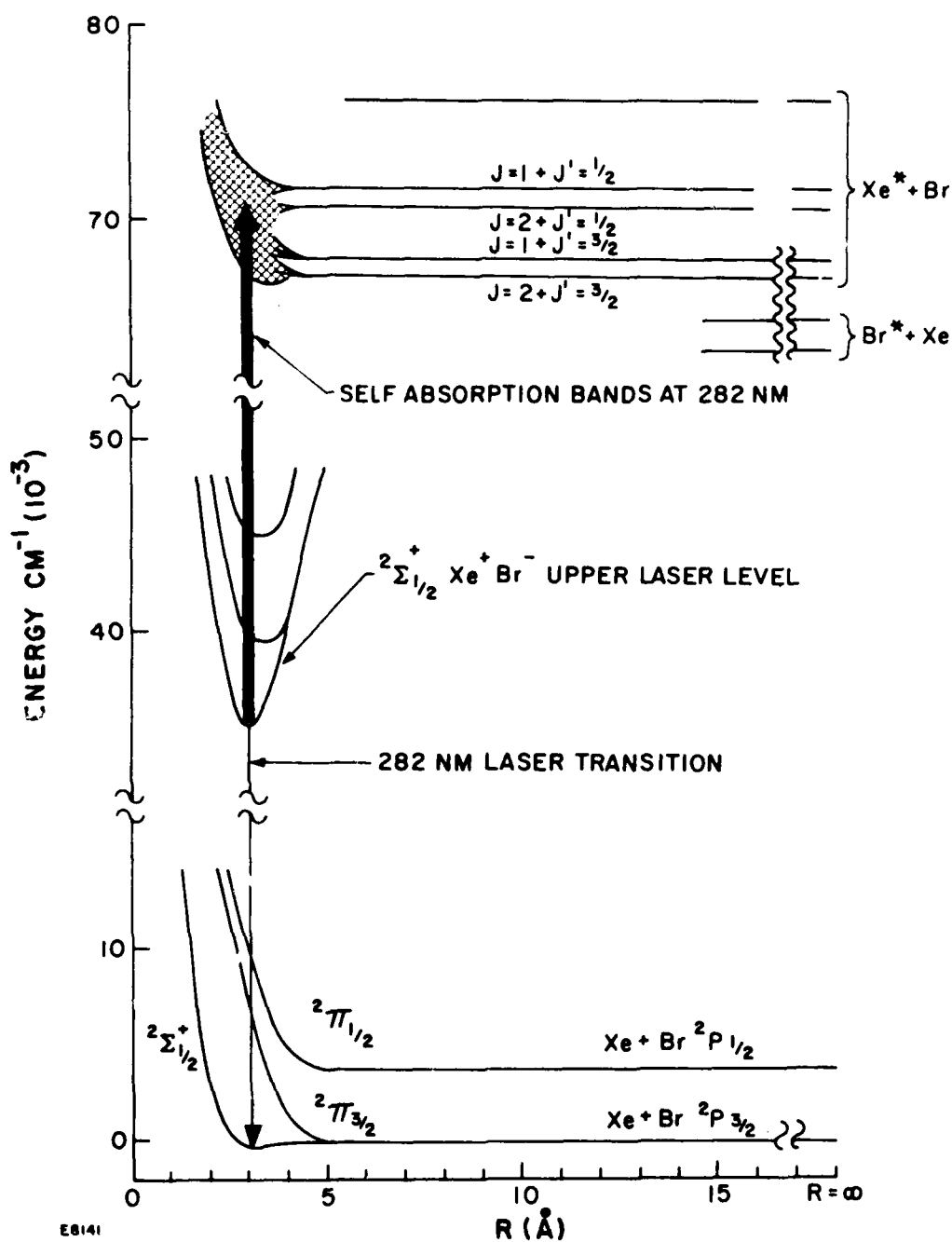


Figure 14. Estimated Potential Curves for XeBr Showing the Possibility of Strong Absorption Band Overlapping the Lasing Transition

to the lasing transition. The absorption is probably spread out over a broader band than the sharp laser transition, as in the alkali halides, ⁽⁴¹⁾ thus allowing for some net gain to occur.

One can see from the approximate potential curves for XeBr that emission on the broadband, near 400 nm, terminating on the $2\Pi_{1/2}$ state would not add sufficient energy to the XeBr* excited state to allow a transition up to states deriving from Xe* + Br. XeBr* is at about $35,000\text{ cm}^{-1}$ and addition of a $25,000\text{ cm}^{-1}$ photon to this species is not sufficient to produce an excited state which dissociates into Xe* + Br or Xe + Br*. This is the basis for our conjecture that the broadbands of XeBr could lead to a UV/visible laser. It must be noted here that Br would not be a good source for XeBr* for the broadband transition since Br₂ absorbs strongly in this band.

An important point to be made is that fairly high quantum efficiency is intrinsic to the rare gas monohalide lasers. Assuming the process begins with production of an excited metastable, such as Kr*, quantum efficiencies of order 50% can be achieved. The lost energy goes into chemical potential by dissociation of the weakly bound halogen molecules, such as F₂, and excess vibrational energy initially invested in producing the rare gas monohalide excited state. The latter loss, corresponding to about 2 eV per laser photon, goes into heavy particle translational energy of the laser mixture on a nanosecond time scale, whereas the energy stored in breaking halogen bonds does not appear as heat until a time scale greater than a microsecond. Neglecting heating due to recombination, a 1-μs laser pulse producing 30 J/liter specific output in KrF will heat the gas mixture the order of 30°C. The neglect of gas heating due to F atom recombination is valid because such recombination is very slow ⁽⁴²⁾ compared to the pulselength.

D. RARE GAS HALIDE KINETICS

The excited-state chemistry that leads to excited rare gas halogen molecules involves a set of competing kinetic paths. The importance of each mechanism can vary with the means of excitation, pressures and mixture mole fractions. In certain mixtures, the rare gas halide emission is dominant. In other mixtures emission on certain bands of halogen molecules is derived or dominates. This brief discussion and the accompanying tables will show the similarities and complementarities of the kinetic chains that can lead to various emission spectra. Detailed modeling of these lasers is currently under way in several laboratories, and a thorough review of this is premature and not given here.

Table 4 gives an overview with short comments on the various reactions which can produce the upper laser levels. Table 5 gives an overall kinetic mechanism for rare gas halides. The principal reaction mechanisms are the alkali-like direct reactions, displacement reactions and ion reactions. The other mechanisms are listed for completeness.

As pointed out above, species such as KrF^* are nothing more than short-lived "pseudo-alkali halides," i.e., diatomic molecules in which one electrical charge has been transferred from the rare gas atom to the halogen. The halogen lasers also operate on transitions from ionic excited states. That is, the upper laser level Br_2^* is the ion pair Br^+Br^- . The formation of alkali halide molecules, halogen ionic excited states and rare gas halide excited states can all proceed along chemically similar pathways. This similarity derives from the fact that metastable rare gas atoms, Kr^* for example, or highly excited halogen atoms have low ionization potentials and chemically behave like ground-state atoms that have low ionization potentials, viz., the alkali atoms. (25,28,31,43) The chemical kinetics of alkalis reacting with halogen molecules has a long

TABLE 4. SIMPLIFIED KINETICS FOR FORMING EXCITED STATES OF RARE GAS HALIDES OR HALOGEN LASERS

<u>Rare Gas Halides</u>	<u>Halogens</u>
<u>Metastable Reactions</u>	
1a $\text{Ar} + \text{X}_2 \rightarrow \text{ArX} + \text{X}$ 1b $\quad \quad \quad \rightarrow \text{Ar} + \text{X}^* + \text{X}$	Ia $\text{X} + \text{X}_2 \rightarrow \text{X}_2 + \text{X}$
Branching can lead to either a rare gas halide laser via 1a or a halogen laser via 1b followed by 1a. Large rate constants measured.	Could also branch to lower states of X_2 causing inefficiencies. Large rate constants predicted.
<u>Ion Reactions</u>	
2a $\text{Ar}^+ + \text{F}^- + \text{M} \rightarrow \text{ArF}^* + \text{M}$	II $\text{I}^+ + \text{I}^- + \text{M} \rightarrow \text{I}_2^* + \text{M}$
2b $\text{Ar}^+ + \text{Br}^- + \text{M} \rightarrow \text{Ar} + \text{Br}^* + \text{M}$	
Extremely rapid and of utmost importance in pure e-beam excited mixtures with rapidly attaching halogens.	Extremely rapid, and could be important in systems in which positive halogen ions are formed.
<u>Displacement Reactions</u>	
3 $\text{ArF}^* + \text{Kr} \rightarrow \text{KrF}^* + \text{Ar}$	III $\text{X}_2 + \text{Y} \rightarrow \text{XY} + \text{X}$
Exothermic ionic displacement in which Kr^+ ion replaces Ar^+ ion. A major channel in e-beam sustained discharges. Large rates estimated.	For exothermic reaction combination could lead to inner halogen emission viz: (ClBr) . Probably not important since large density of free atoms hard to come by.
<u>Recombination of Excited Halogens</u>	
4 $\text{Br}^* + \text{Xe} + \text{M} \rightarrow \text{XeBr}^* + \text{M}$	IV $\text{I}^* + \text{I} + \text{M} \rightarrow \text{I}_2^* + \text{M}$
Reactions such as this important in Ar/Xe/ X_2 mixtures where reactions 1b or 2b are fast and produce the excited halogen rather than the rare gas halide.	Rate of this reaction limited in a halogen laser by smaller amounts of I present. Obviously important when source of I atoms is completely dissociated.
<u>Direct Pumping-Electrons or Energy Transfer</u>	
5 $\text{e} + \text{XeF}_2 \rightarrow \text{XeF}^* + \text{F}$ $\quad \quad \quad \rightarrow \text{XeF}^* + \text{F}^-$ $\text{Xe} + \text{XeF}_2 \rightarrow \text{XeF}^* + \text{Xe} + \text{F}$ Potential limited.	V $\text{e} + \text{X}_2 \rightarrow \text{X}_2^* + \text{e}$ $\text{Ar}_2 + \text{X}_2 \rightarrow \text{X}_2^* + 2\text{Ar}$ Possibly important in certain rare gas halogen mixtures.

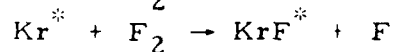
TABLE 5. SIMPLIFIED MECHANISM/RARE GAS HALIDE LASERS

Discharge Pumping/Mixture

o Metastable Formation



o Reaction with Halogen



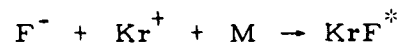
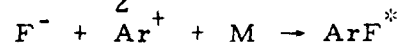
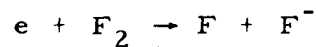
o Displacement



E-Beam Pumping

o All of the Above

o Ion Recombination



history and this chemistry is understood in much detail. The mechanism for such alkali/halogen reactions is discussed in detail elsewhere.⁽⁴³⁾ The reaction of a Kr^* or Br^* with a halogen containing molecule should produce an ionic species. Reactions 1a, 1b and 1c of Table 3 are examples of such reactions. These reactions are thought to proceed by way of an ionic covalent curve crossing, often called the "harpooning" mechanism.^(28,31,43) In such reactions, the low ionization potential of the alkali or excited species and the high electron affinity of the halogen molecules allows an ionic potential curve of the form $M^+ + X_2^-$ to cross that of $M^* + X_2$ at fairly large internuclear separations, distances of order 5 \AA . The X_2^- ion formed by an electron hop, when the ionic and covalent potentials become degenerate, is unstable with respect to dissociation into $X^- + X$ in the presence of the large electric field of the M^+ ion. As a result, the $M^+ X_2^-$ temporary triatomic species falls apart into an ion pair $M^+ X^-$ leaving behind an X atom. The term "harpooning" mechanism derives from considering the electron that hops from the M^* over to X_2 molecule apart and forms the new ionic, $M^+ X^-$ species. The prime difference between reactions of halogen molecules with alkali metal atoms and the corresponding chemistry with excited states such as Kr^* or Br^* is that in the alkali reactions only one electronic state can be formed whereas several potential product channels can exist in certain excited state/halogen molecule reactions. A similar multiple product channel situation exists in the reaction of halogen atoms with diatomic alkali molecules. In this case, usually several low lying states of alkali atoms are produced by the chemical reaction.⁽⁴⁴⁾

The cross sections and exit channel branching ratios for a number of excited metastable inert gas atoms reacting with halogens are now being measured.⁽⁴⁵⁾ The bulk of this work is being done at low pressures. The spectra observed are similar

but not identical to those at high pressure as in e-beam or discharge excited lasers. A brief compendium of some of the published relevant reaction rates for reaction of metastable inert gases with halogen containing compounds is given in Table 6.

TABLE 6. SOME KINETIC RATE CONSTANTS FOR
RARE GAS METASTABLE/HALOGEN REACTIONS

	a. k_Q	b. σ_C	Comments
Xe (3P_2) +	HBr	6.1	173 ^(a)
	HCl	5.6	110 ^(a)
	Cl ₂	6.5	193 ^(a)
	Br ₂	6.0	202 ^(b)
	CF ₃ I		184 ^(b)
	F ₂	7.3	156 ^(c)
			Should produce XeF [*] with near unit quantum yield
Kr (3P_2) +	NF ₃	0.86	23 ^(c)
	F ₂	8.1	163 ^(c)
			Should produce KrF [*] with near unit yield
	Cl ₂	6.0	147 ^(c)
	NF ₃	1.6	39 ^(c)
Ar (3P_2) +	Xe	1.6	46 ^(c)
	Br ₂	6.5	147 ^(d)
			Produces Br
	Cl ₂	4.7	95 ^(e)
		7.1	142 ^(d)
	F ₂	8.5	148 ^(c)
			Should produce ArF [*] with near unit yield
	NF ₃	1.4	28 ^(c)
	Kr	0.06	1.3 ^(f)
	Xe	1.8	40 ^(f)

a. Rate constants, k_Q , given in units of 10^{-10} cm/molecule sec.

b. Cross sections, σ_Q , given in units of 10^{-16} cm².

(a) = Reference 46

(b) = Reference 28

(c) = D. Setser, Private Communication

(d) = Reference 45

(e) = Reference 31

(f) = Reference 47

III. HALOGEN RESEARCH

A. IODINE

E-beam-pumped UV lasing was observed on the molecular iodine bands $1432, 2g^3\pi \rightarrow 2431 2u^3\pi$ at 342 nm. Figure 15 shows the electronic potential curves for states relevant to the laser transition. This identification of the laser transition states is different from the original designation⁽¹⁰⁾ and follows from Ref. 48. This laser was obtained by pulsed e-beam irradiation of noble gas mixtures containing primarily Ar buffer gas and trace amounts of iodine containing species HI and CF_3I . Laser action was also obtained from mixtures of $Ar/Xe/RI$ ($R=H, CF_3$). Xe was initially added to the gas mixtures in an attempt to lase the xenon iodide bands^(10,48) in analogy to the previously reported lasers. Addition of Xe to these mixtures decreases the I_2 spontaneous and lasing intensities while bringing out the expected xenon halide spectra. The highest I_2 laser output occurs with no xenon present. Very weak laser action has also been observed in Ar/I_2 mixtures utilizing room-temperature iodine vapor. The possibility of e-beam-pumped laser action on this molecular iodine band has been suggested by Wilkerson and Tisone⁽⁴⁹⁾ and by McCusker, et al.⁽⁵⁰⁾

The broad-banded I_2 emission spectrum, extending from 300 to 345 nm, has been the subject of numerous investigations.⁽⁴⁹⁻⁵³⁾ Mulliken's classic paper thoroughly reviews the spectroscopy of I_2 ,⁽⁵²⁾ and it seems to be agreed that this I_2 transition has an excited state which dissociates to the separated ion pair $I^+ + I^-$. The identification of the 342-nm emission observed from e-beam-excited Ar/RI mixtures with the I_2 342-nm band is clear from a comparison of our spontaneous emission spectra with the spectra described by previous

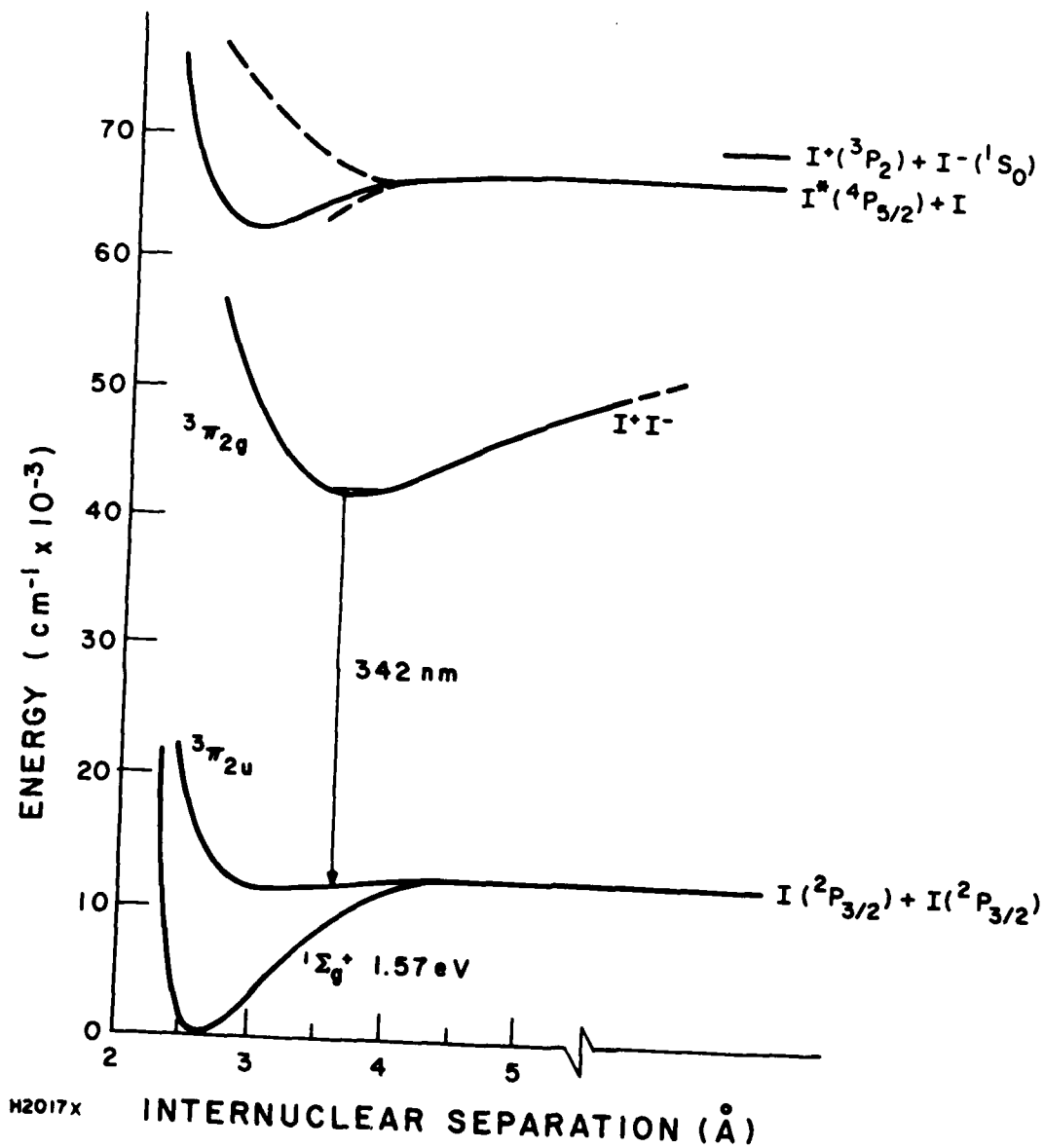
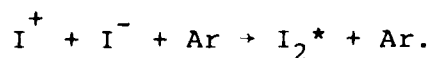


Figure 15. Potential Curves for I_2 Showing Electronic States Relevant to the Laser Transition

workers. (28,49-53) The prominent 342-nm band with its regularly spaced fluctuations and the weaker I_2 bands at 287, 430, and 450 nm are clearly seen on our plates. Figure 16 shows densitometer traces of the 340-nm band under conditions of spontaneous and stimulated emission. The laser spectrum shows definite narrowing of the band. More than one vibrational band appears to be oscillating, and the laser wavelength could presumably be discretely tuned. The spectra and laser action were obtained in a device previously described in Section II. Peak laser powers of the order of 1 kW have been obtained from 50 psia Ar/HI mixtures containing 0.3% HI. Figure 17 shows a sample oscillogram of the photodiode signal. Typically, the laser turns on about 40 ns after the e-beam. The turn-on time is not strongly dependent on the pressure and lasts for about 80-100 ns. Since this time is longer than the estimated radiative lifetime, (49) this suggests that lower-level relaxation is fast and that quasi-cw operation is possible. The total energy output corresponds to an efficiency of $10^{-3}\%$ for converting deposited e-beam energy into laser light through the 1/2% transmitting mirrors. If the lasing transition is saturated and there are losses in the gas, greater powers and laser efficiencies could be obtained by coupling more light out of the cavity. McCusker, et al., project considerably higher efficiencies for the e-beam pumped Ar/ I_2 systems. (50) However, we have observed only weak laser action in Ar/ I_2 , possibly because of the low vapor pressure of I_2 at room temperature.

The formation of excited state I_2^* in Ar/RI mixtures was described in Ref. 10 as the result of the ion-ion recombination of I^+ and I^- intermediaries



In addition to this mechanism, the following formation pathways should also be considered.

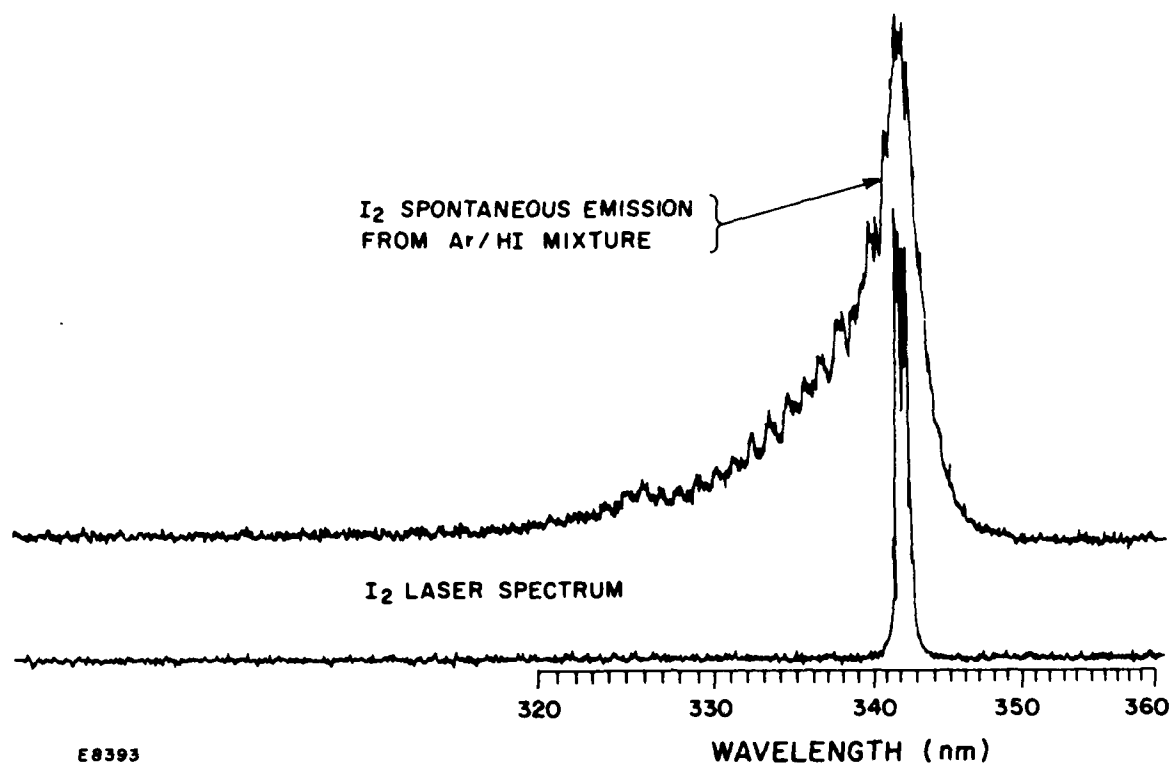


Figure 16. Densitometer Tracings of I₂ Emission Produced when Ar/HI Mixtures are Excited with an E-Beam

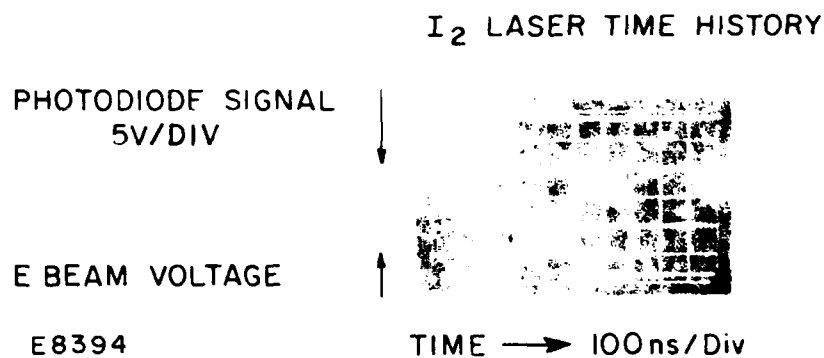
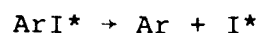
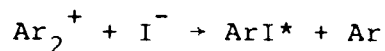
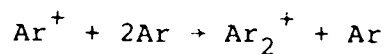
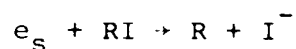
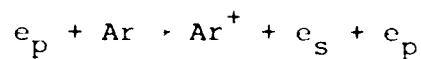
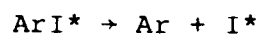
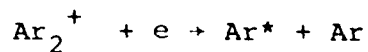


Figure 17. Oscillograms of the Photodiode Viewing the Laser Output and the Voltage Pulse Producing the E-Beam. The laser intensity was attenuated by a factor of 160 before striking the photodiode. The signal corresponds to a peak power of about 1 kW.

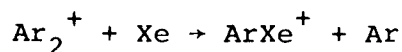
1. Argon Ion Channel



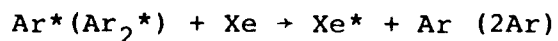
2. Argon Metastable Channel



These ion and metastable channels have also been suggested⁽⁵⁴⁾ as the formation kinetics for Br_2^* in Ar/ Br_2 and Ar/ BrI mixtures. These additional channels are also consistent with the reduced laser output observed when Xe is added to the gas mixture. In Ar/Xe mixtures it is expected that fast reactions such as



and



would reduce the ArI^* and hence I^* formation, as well as generate competing channels to form XeI^* .

As discussed above, observation of the fluorescence emanating from e-beam-pumped Ar/I₂ mixtures has been determined⁽⁵⁰⁾ that I₂ is the best donor. The fluorescence efficiency using I₂ as the donor was reported⁽⁵⁰⁾ to be about 20%; however, the laser efficiency with Ar/HI mixes was only about 1%. The possibility of increasing the laser efficiency by using higher density I₂ mixtures has been considered to obtain the required vapor pressure of I₂, the laser mixture would have to be heated to about 100°C.

Another possible reason for the relatively low laser efficiency is that Ar₂⁺, the major positive ion in the lasing medium, has a large photoabsorption cross section at the lasing wavelength.⁽⁵⁵⁾ By replacing Ar with Ne, the I₂ laser efficiency could improve as was observed in XeF laser studies.⁽⁵⁷⁻⁵⁹⁾

These changes of iodine donor and rare gas species did not achieve significant improvement.

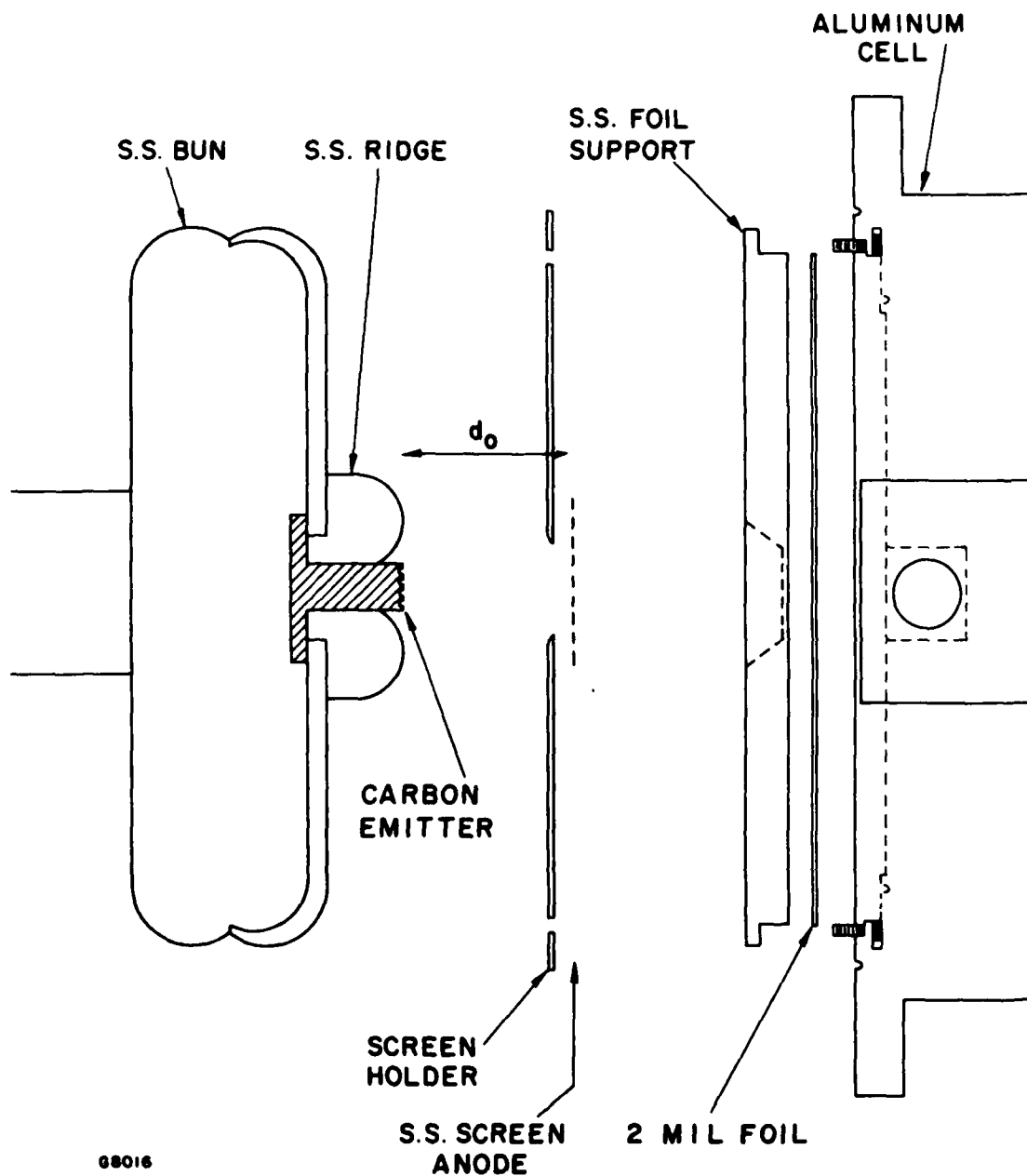
IV. MERCURY HALIDE RESEARCH

The mercury halides, like the rare gas halides, have ionic upper levels. Hence the formation kinetics of the upper laser level should be rapid and efficient. Because the ionization energy of mercury is lower than the rare gases, the mercury halides radiate at longer wavelengths than the rare gas halides. The mercury halide lasers demonstrated at AERL are $\text{HgCl}^{(12)}$ (558 nm) and $\text{HgBr}^{(13)}$ (502 nm).

A. EXPERIMENTAL APPARATUS

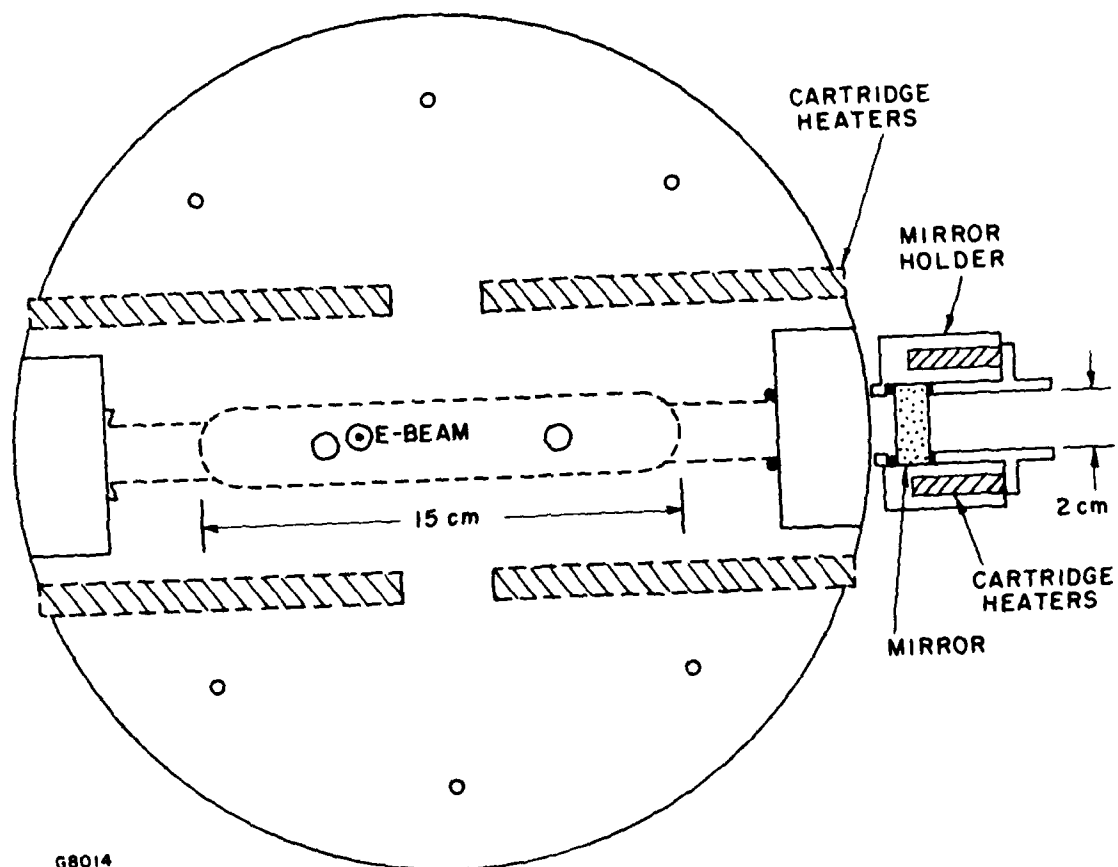
The lasing and spontaneous emission experiments were carried out in an aluminum cell, shown schematically in Figures 18 and 19, in which the pressure could be varied up to pressures in range of 7 atm. The cell temperature was controlled by cartridge heaters positioned to uniformly heat the gas cavity and this temperature was kept below 300°C to allow the use of Viton and Teflon O-rings. Laser mirrors are housed in heated aluminum holders providing an optical aperture of about 2 cm in diameter and sealed directly to the cell. The cavity mirrors are separated by 24 cm. The heated mirror assembly is shown in Figure 20. The high pressure rare gases (Ar/Xe) are heated in S.S sample bottles within an oven shown in Figure 21. An overview of the experimental apparatus is shown in Figure 22.

A Marx generator is used to impulse charge a cold-cathode e-gun to about 300 kV for about 150 ns providing a current density of about 100 A/cm² in the cell. The e-beam of roughly 1 x 15 cm² cross section was injected into the gas transverse to the laser cavity optical axis through a 2-mil cell foil and irradiated a gas volume of about 85 cm³. Figure 23 shows the e-beam diode including the graphite cathode. This design was upgraded for these experiments to increase reliability and run time. The e-beam energy deposition in the gas mixture was deduced from differential pressure measurements.



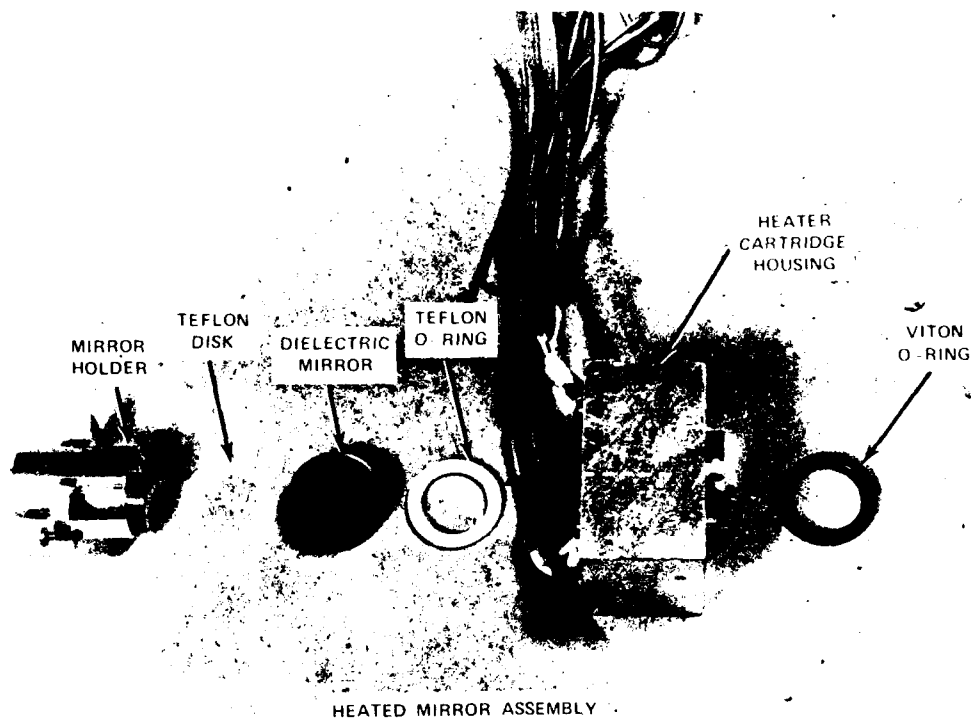
68016

Figure 18. E-Beam/Laser Cell Configuration Indicating Transverse Beam Excitation



G8014

Figure 19. Aluminum Laser Cell Showing Cartridge Heater Arrangement, Cavity and Window Configuration



J4960

Figure 20. Heated Mirror Assembly

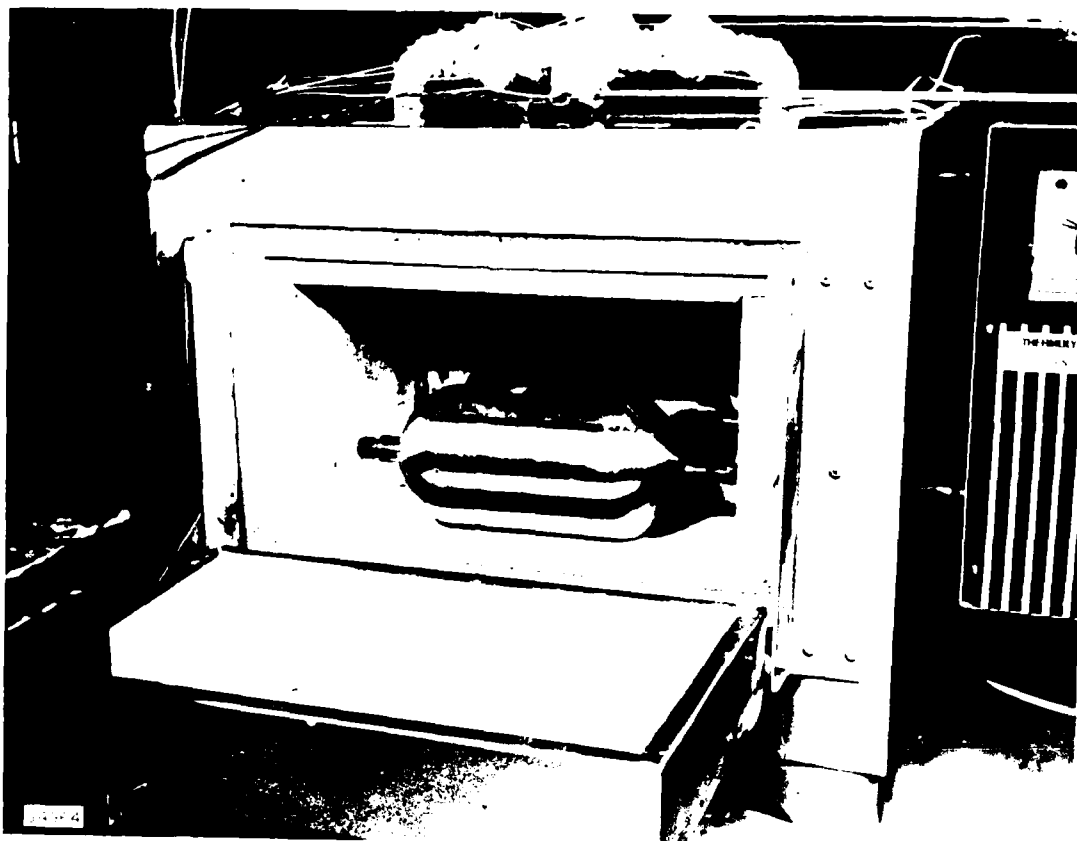


Figure 21. Laser Gas Bottle Oven



Figure 22. Overview of Experimental Apparatus

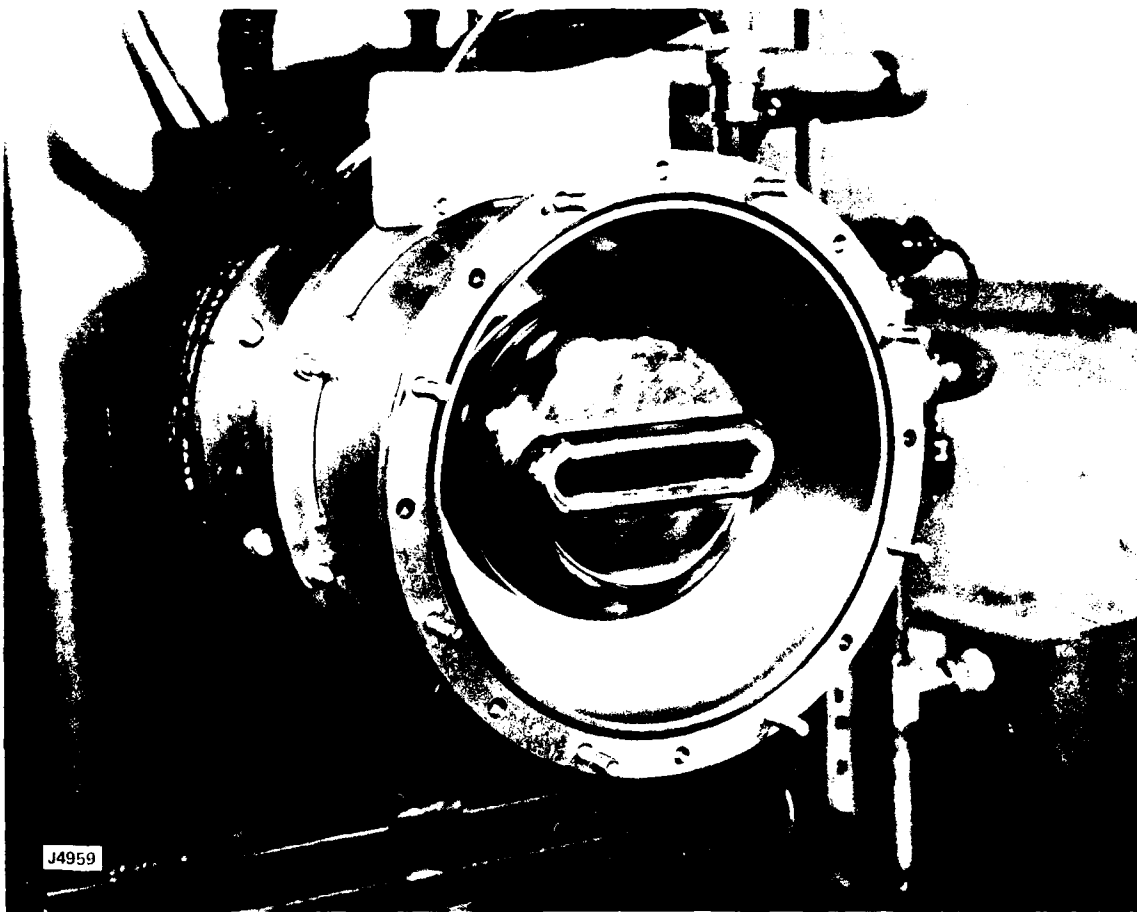
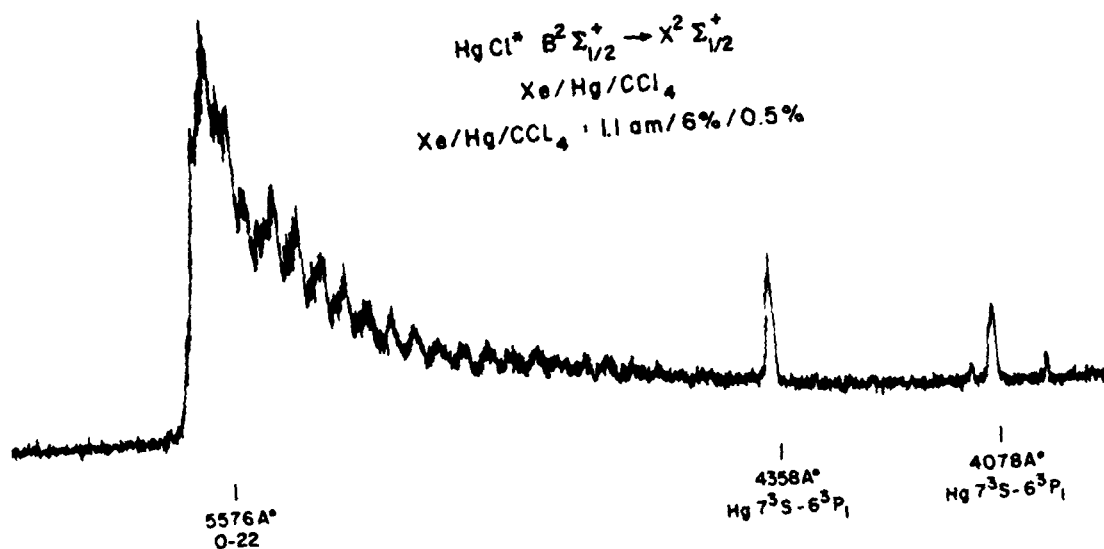


Figure 23. E-Beam Cathode

B. MERCURY HALIDE SPECTROSCOPY

The fluorescence spectra of HgCl and HgBr are shown in Figures 24 and 25, respectively. These spectra were taken using photographic plates. The gas mixture composition and total pressure were similar to those observed under strong lasing conditions.

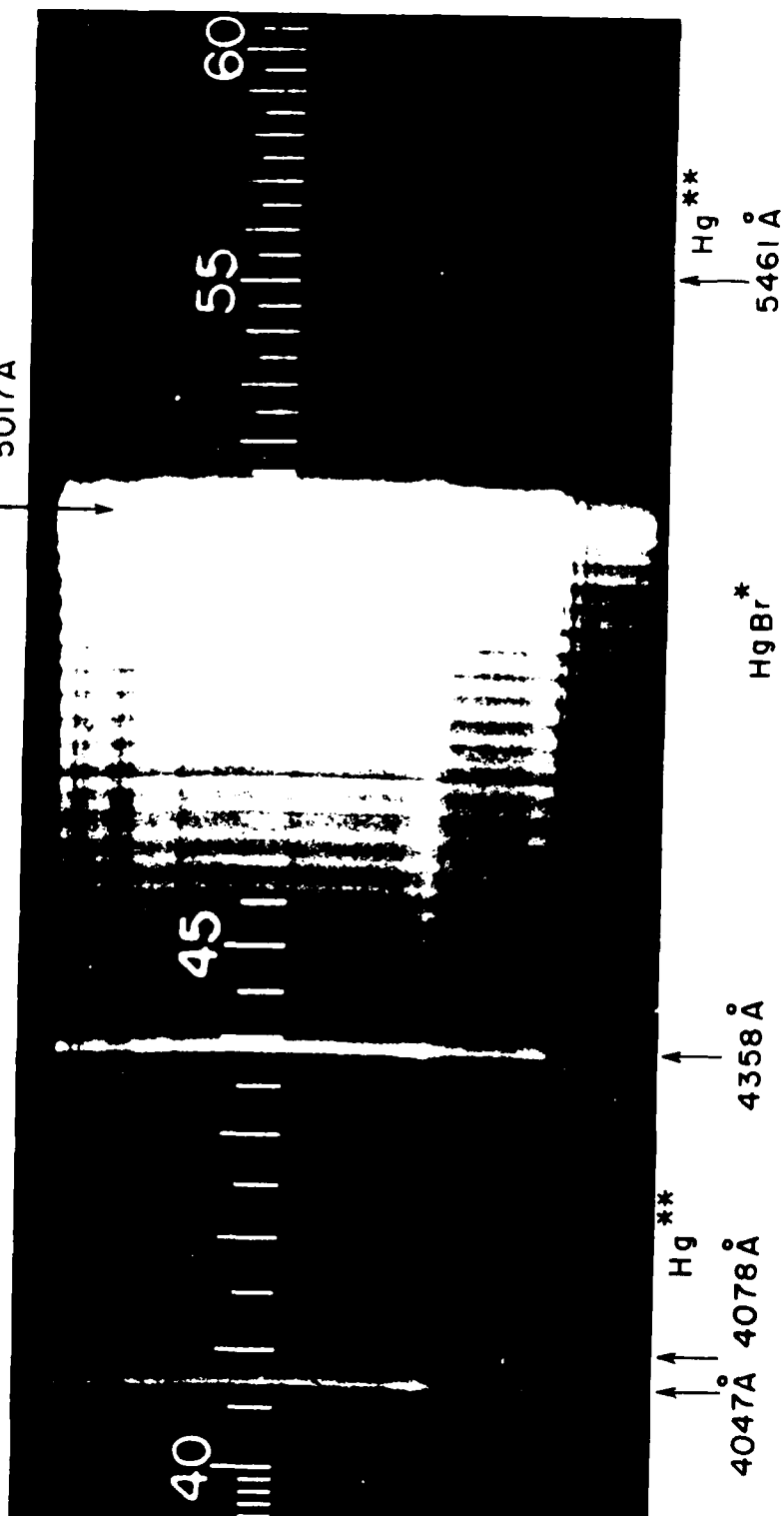
The fluorescence spectra for different HgCl , HgBr and HgI mixtures are shown in Figures 26, 27, and 28, respectively. The mixture composition of rare gas/mercury/halogen donor is varied in each case to show the competing formation channels which are occurring in these mixtures.



H2672

Figure 24. HgCl^* Fluorescence Spectrum

$\text{Hg Br}^* \text{ B}^2\Sigma \rightarrow \text{X}^2\Sigma$ FLUORESCENCE
Ar/Xe/Hg/HBr



J4961

Figure 25. HgBr^* Fluorescence Spectrum

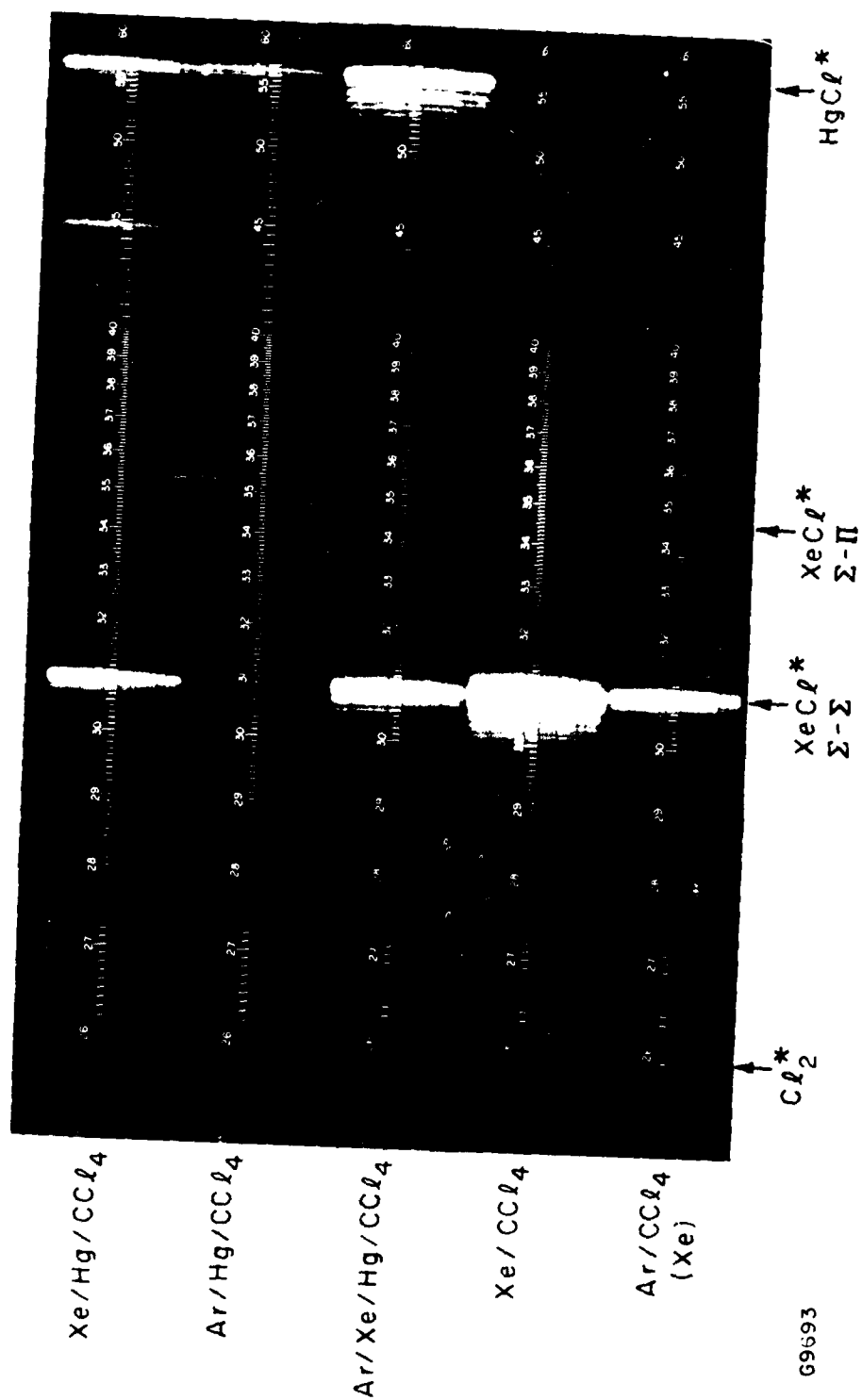
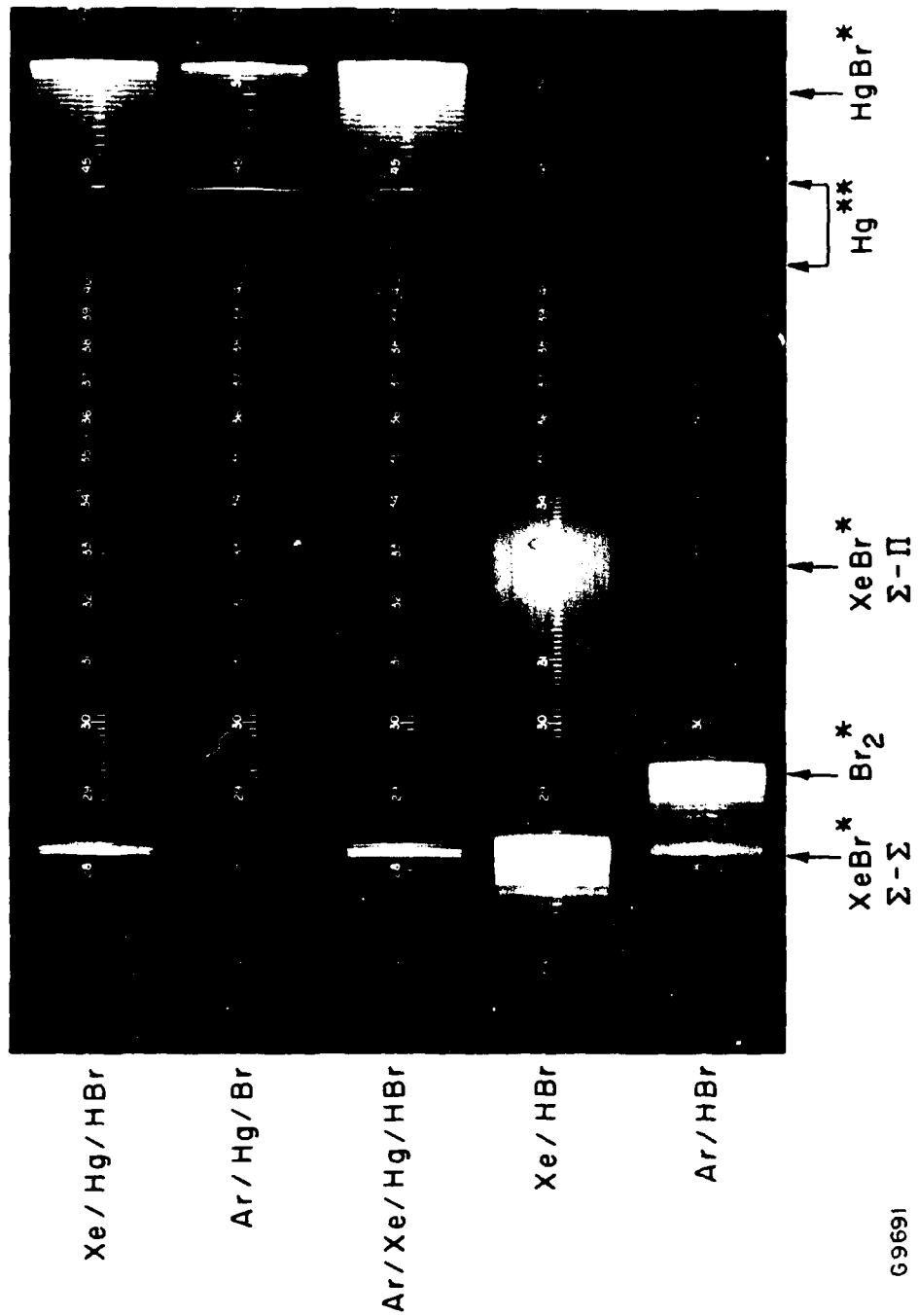


Figure 26. Fluorescence Spectra for Various Rare Gas/Hg/CCl₄ Mixture Compositions



G9691

Figure 27. Fluorescence Spectra for Various Rare Gas/Hg/HBr* Mixture Compositions

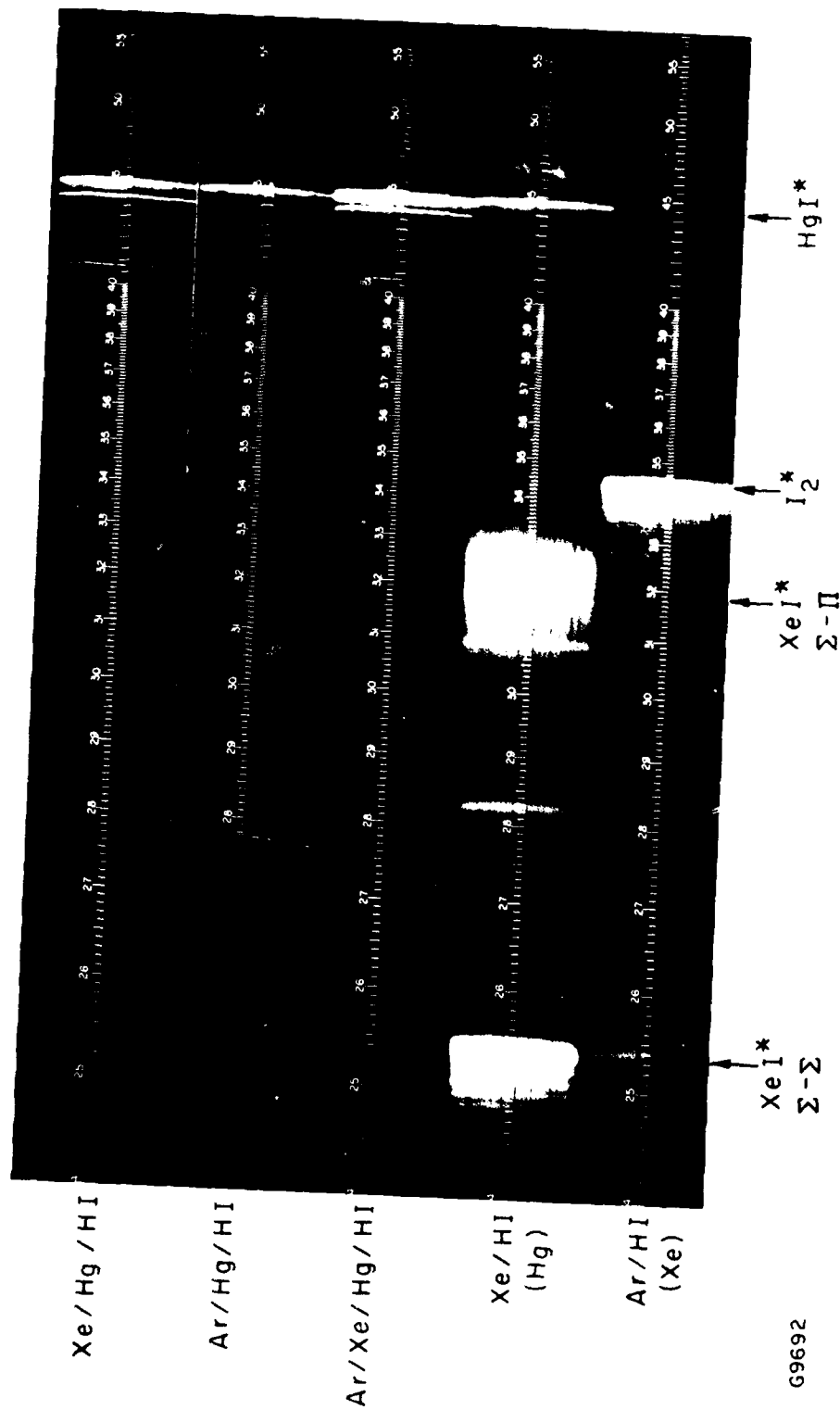
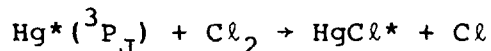


Figure 28. Fluorescence Spectra for Various Rare Gas/Hg/HI Mixture Compositions

C. HALOGEN DONOR SELECTION

In e-beam-pumped mixtures, the halogen donor selection has a wide range of possibilities. In this case donors are chosen from simple halogen bearing molecules which do not absorb at the laser wavelength and in addition provide adequate rates for dissociative attachment near electron energies of ~ 1 eV.

Halogen donor selection is one of the more critical issues of discharge pumped lasing since the $\text{Hg}^*(^3\text{P}_0)$ metastable energy (~ 4.7 eV) is close to the average A-Cl bond strength (~ 3 eV). However, calculations⁽⁶⁰⁾ substantiated by measurements⁽⁶¹⁾ in Ar-Hg discharges indicate that electron collisional mixing of the three metastables $\text{Hg}^*(^3\text{P}_{0,1,2})$ has a large enough cross section ($\sim 19 \text{ \AA}^2$) to maintain the largest population in the highest $\text{Hg}^*(^3\text{P}_2)$ metastable at 5.43 eV. This may ease halogen donor selection, and in addition, provide more flexibility to tailor the choice of halogen donor to the needs of discharge stability. A list of halogen donor candidates is given in Table 7. Figure 29 emphasizes the energetics required by the donor selection and Table 8 indicates the branching ratio for formation of HgCl^* from collisions



from each level $J = 0,1,2$.

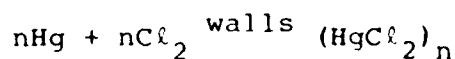
Finally, the selection of a halogen donor requires a consideration of possible surface catalyzed reactions which may be accelerated at the $\sim 300^\circ\text{C}$ gas mixture temperatures. Considering the advantages indicated by Figure 29 and Table 8 most e-beam discharge experiments to date have explored the use of molecular chlorine, Cl_2 .

Unfortunately, early attempts to produce efficient lasing were not very successful, in that the reactants were rapidly disappearing upon entering the heated laser cavity before any exciting e-beam sustained discharge could be applied.

TABLE 7. CROSS SECTIONS FOR REACTION OF SOME HALOGEN SPECIES WITH $\text{Hg}^* ({}^3\text{P}_0)$ and $({}^3\text{P}_2)$

	$\frac{{}^3\text{P}_0}{\sigma (\text{Å}^2) (62)}$	$\frac{{}^3\text{P}_2}{\sigma (\text{Å}^2) (63)}$
CCl_4	46	34
CHCl_3	42	8
CH_2Cl_2	31	--
CH_3Cl	28	--
CH_3Br	24	--
CH_3I	39	--
Cl_2	--	90

Experiments⁽⁶⁵⁾ showed the reaction as proceeding on the walls of the container with a stoichiometric loss of Hg and Cl₂, e.g.,



Data were collected in Inconel, quartz, stainless steel, and Teflon-coated stainless steel reaction cells. The results of these experiments in turn prompted the laser experiments to decrease the residence time in the cavity to times < 10 s. Subsequently, intrinsic laser efficiencies in excess of 3% were obtained for HgCl* lasers compared to the earlier efficiencies reported of < 1%.

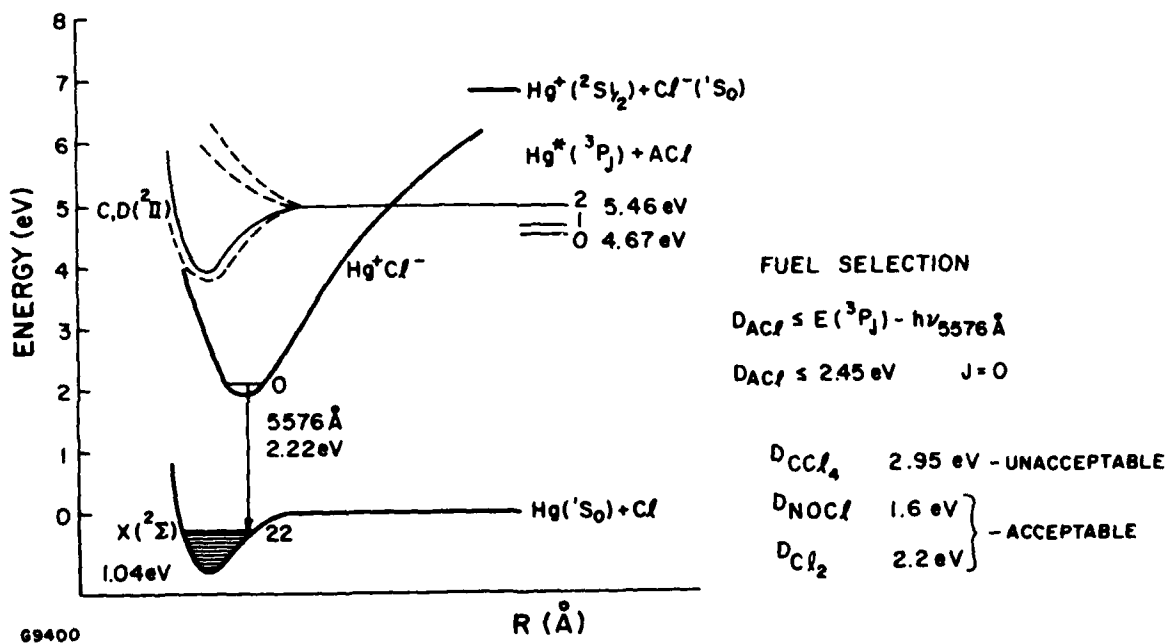
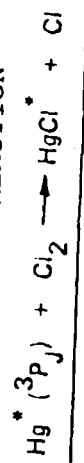


Figure 29. Discharge Pumping Donor Energetics - HgCl*

TABLE 8. CROSS SECTIONS AND BRANCHING RATIOS FOR
THE NEUTRAL REACTION



<u>Hg[*] STATE</u>	<u>REACTIVE CROSS SECTION (Å²)</u>	<u>BRANCHING RATIO (%)</u>	<u>REFERENCE</u>
$^3\text{P}_2$	90	~90	(63)
$^3\text{P}_1$	1.2	~4	AERL (1978)
$^3\text{P}_0$	0.4	~1	(64)

H8484

D. MERCURY HALIDE LASERS

This section summarizes the characteristics of the new high-power visible lasers operating on the $B^2\Sigma^+_{1/2} \rightarrow X^2\Sigma^+_{1/2}$ transition of HgCl at 5576 Å and the same molecular electronic transition of HgBr at 5018 Å and 4984 Å. The upper laser state is ionic in nature and is formed directly by chemical reactions in an e-beam excited mixture of high pressure Ar/Xe and small amounts of Hg, CCl₄ and HBr. The lower laser level is the molecular ground state which is covalent in nature and bound by the order of 1 eV. The potential curves for HgCl and HgBr, shown in Figures 30 and 31, respectively, indicate the laser transitions. The ionic character of the upper laser level provides the opportunity to utilize the highly efficient formation processes important in lasers such as KrF.

1. Mercury Chloride

Laser action from HgCl was obtained in a typical mixture of Ar, Xe, Hg and CCl₄ in the ratio 85.7%/11.1%/2.1%/1.1% respectively at an Ar density of 3 amagats. The cell and Hg reservoir temperatures were 275°C and 260°C respectively. The laser output was viewed at one end with a calibrated planar photodiode (ITT F4000-S5) and at the other end with a 1/2 m Hilger quartz spectrograph. The HgCl spontaneous emission spectrum, shown in Figure 32, obtained in the presence of these high-pressure rare gas mixtures indicates that the most intense transitions occur between $v' = 0$ and high v'' ground state levels. The laser transition is identified as $v' = 0 \rightarrow v'' = 22$ (HgCl³⁵) which corresponds to the strongest transition observed in spontaneous emission.

The peak laser power obtained in these experiments was about 1.7 MW with 50% output cooling as shown on the oscillogram trace in Figure 33(a). The associated pulse energy of 175 mJ corresponds to an intrinsic laser efficiency of about 3.5% considering the e-beam energy deposited in the laser volume was about 4.8 J.

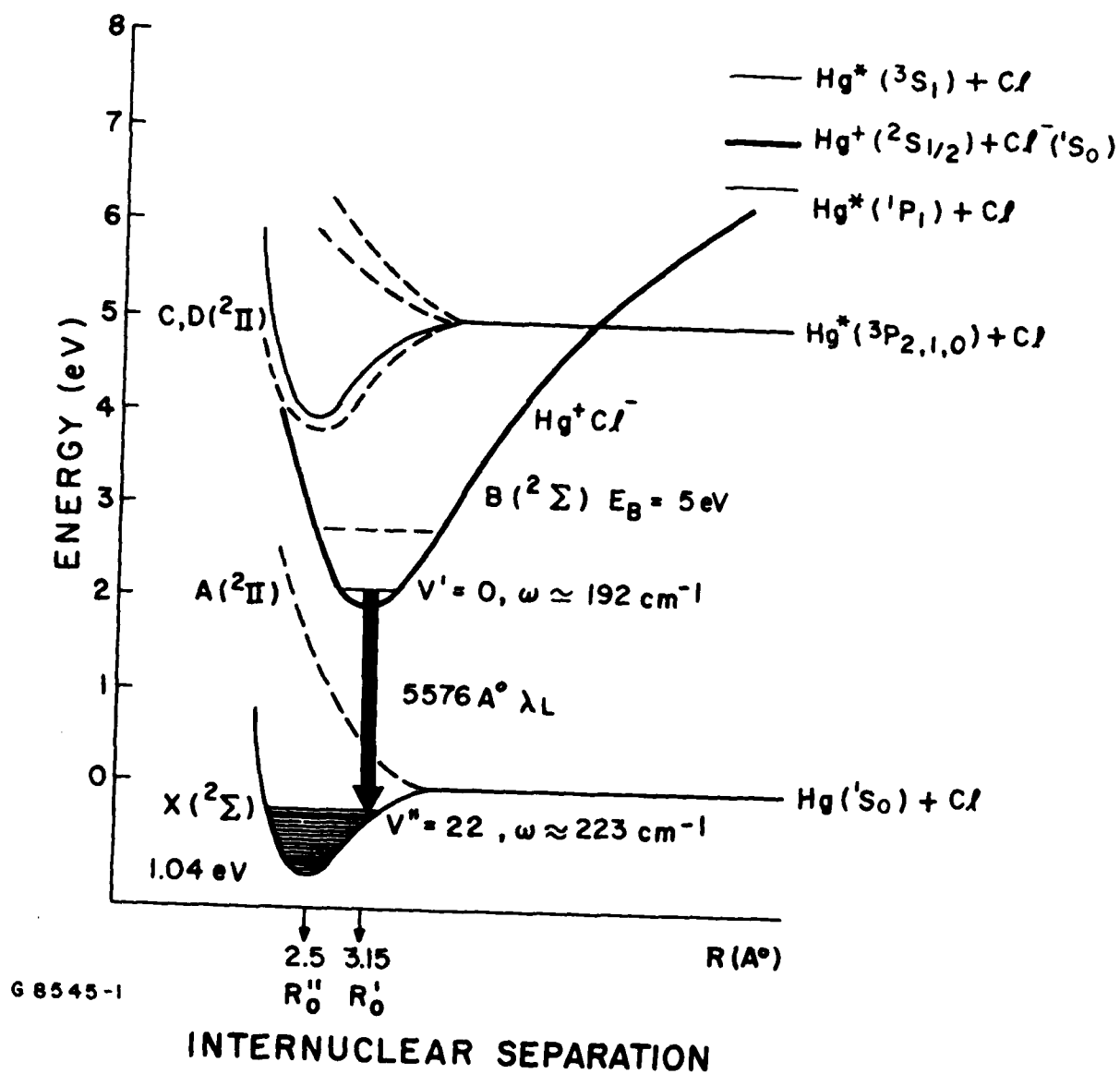


Figure 30. Estimated Potential Curves for HgCl

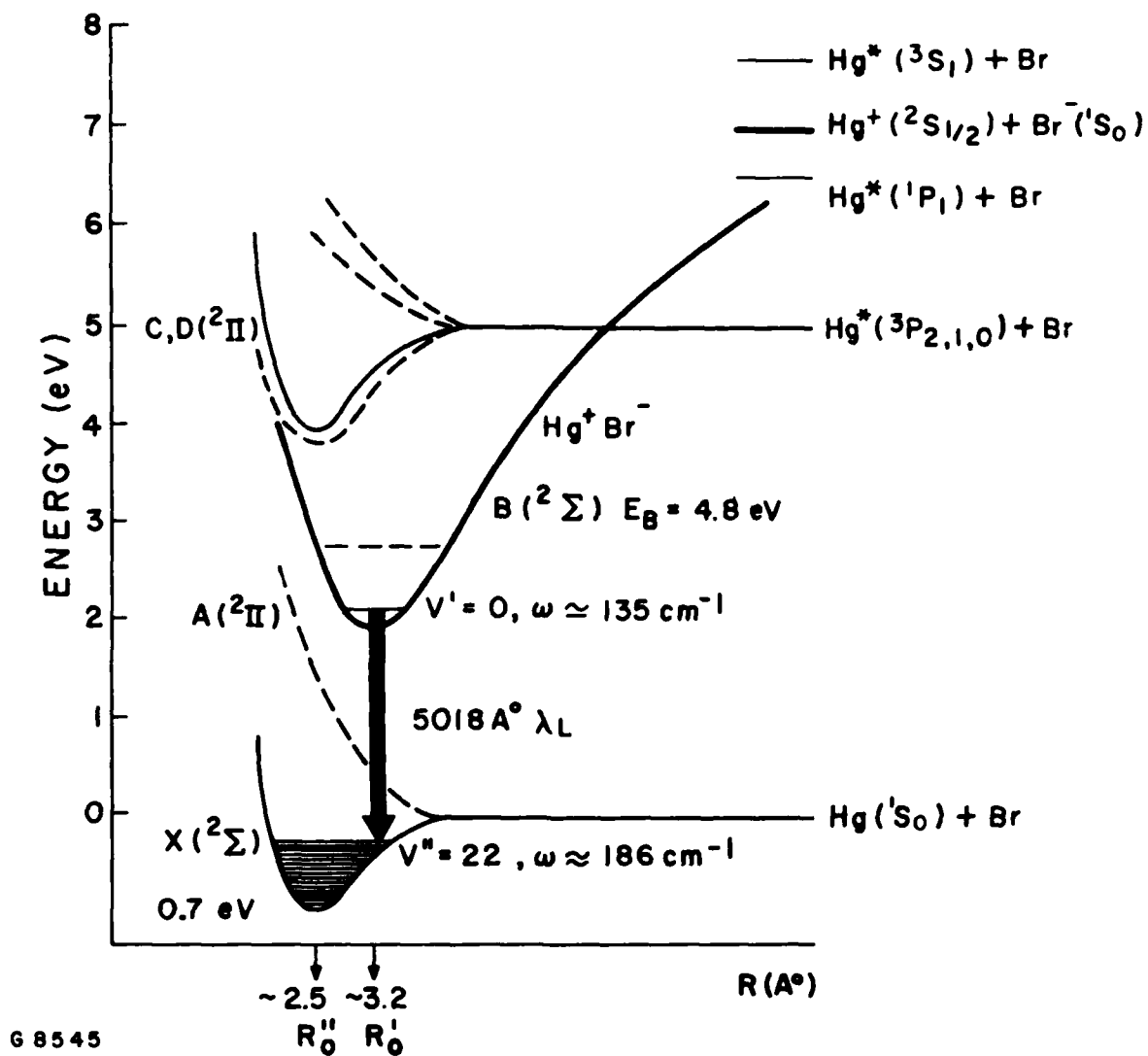


Figure 31. Estimated Potential Curves for HgBr

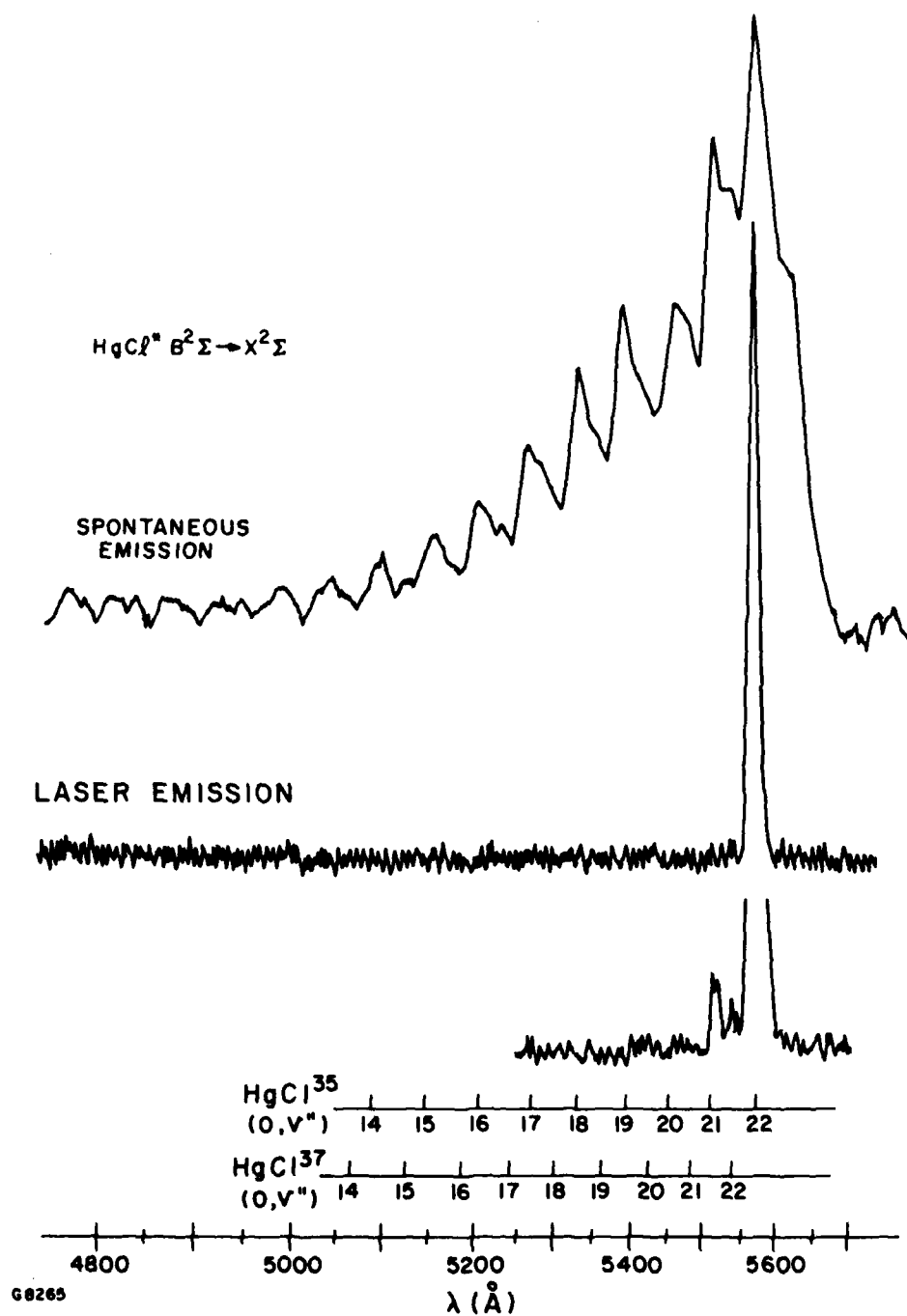


Figure 32. Mercury Chloride Laser Emission and Spontaneous Emission Spectra

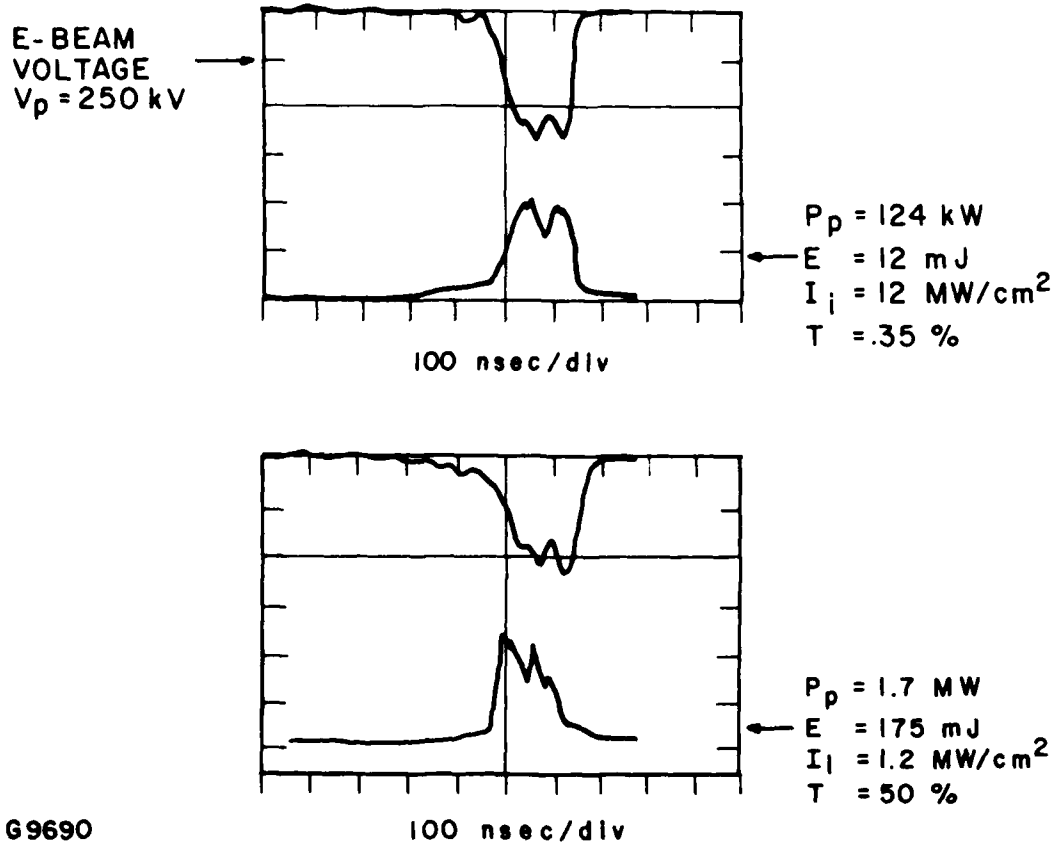


Figure 33. HgCl Data Oscillogram Trace Showing the E-Beam Voltage Pulse and the Corresponding Photodiode Laser Signal for (a) Output Coupling $T = 50\%$; (b) Output Coupling $T = 0.35\%$

Bottlenecking of the $v'' = 22$ lower level is not limiting the laser pulsewidth of about 100 ns. This has also been observed when the cavity flux was $\sim 12 \text{ MW/cm}^2$ as shown in Figure 33(b) which implies a very rapid relaxation of the lower laser level of roughly $\leq 1 \text{ ns}$. A summary of the results of these small scale experiments is shown in Table 9.

From the heavy body quenching rate constants given in Ref. 66 an estimate of the saturation flux can be obtained for arbitrary mixtures of Ar/Hg/Cl₂ and Ar/Xe/Hg/CCl₄ which have been used respectively in discharge and e-beam pumping of the HgCl* laser. The quenching of HgCl by Hg has recently been measured in a separate experiment as $k_{\text{Hg}} = 4 \times 10^{-11} \text{ cm}^3/\text{s}$. The saturation flux ϕ_s can be computed using the following expression

$$\sigma_s = \frac{h\nu}{\sigma_s \tau} \left\{ 1 + k_{\text{ACl}} \tau [\text{ACl}] + k_{\text{Ar}} \tau [\text{Ar}] + k_{\text{Xe}} \tau [\text{Xe}] + k_{\text{Hg}} \tau [\text{Hg}] \right\} \quad (2)$$

where σ_s is the stimulated emission cross section, $h\nu$ is the photon energy, τ is the HgCl* radiative lifetime, and k_i the quenching rate constant for each component. It should be noted that the saturation flux defined in Eq. (2) is applicable in the limit that the population of the lower laser level is negligible. From the HgCl* spontaneous spectra we have estimated $h\nu/\sigma_s \tau$ to be 0.16 MW/cm^2 . For typical laser mixes containing 1% Cl₂, 2% Hg and 97% Ar at a total pressure of 2 amagats one obtains $\phi_s = 0.45 \text{ MW/cm}^2$ and for 2% CCl₄, 2% Hg, 11% Xe and 86% Ar at 2 amagats one obtains $\phi_s = 0.31 \text{ MW/cm}^2$.

2. Mercury Bromide

Laser action from HgBr was obtained in a typical mixture of Ar, Xe, Hg and HBr in the ratio 86.4%/10.8%/2.0%/0.8% respectively at an Ar density of 3 amagats. The laser emission

TABLE 9. HgCl LASER CHARACTERISTICS

- WAVELENGTH 5576 Å
- GAS MIXTURE
 $\text{Ar/Xe/Hg/CCl}_4 = 84.7\%/11.1\%/2.1\%/1.1\%$
 $\text{Ar} \sim 3 \text{ AMAGATS}$
 CELL TEMPERATURE 275 °C
- E-BEAM ENERGY DEPOSITION 4.8 J
- INTRINSIC EFFICIENCY
 (50% COUPLING) 3.8%
- PEAK POWER 1.7 MW
- PULSEWIDTH 100 nsec

G9681

shown in Figure 34 is identified as the $v' = 0 \rightarrow v'' = 22$ and $v' = 0 \rightarrow v'' = 21$ bands which again correspond to the strongest transitions observed in spontaneous emission. The output coupling for each cavity mirror was 3%. Figure 35 shows an oscillogram of the photodiode signal from the HgBr laser in trace (b) and the e-beam voltage pulse monitor in trace (a). The peak laser power of about 50 kW and integrated pulse energy of 3.2 mJ correspond to a laser efficiency of about 0.25%. This is certainly a lower bound, and optimization of laser mixtures, pumping power, and output coupling should result in higher efficiency. The laser pulsewidth at half-peak intensity is about 60 ns and broadens to 130 ns near the base of the pulse which is comparable with the pulsewidth observed in spontaneous emission. Bottlenecking of the lower laser levels does not appear to be limiting the laser pulse length. A summary of the results of these small scale experiments is shown in Table 10.

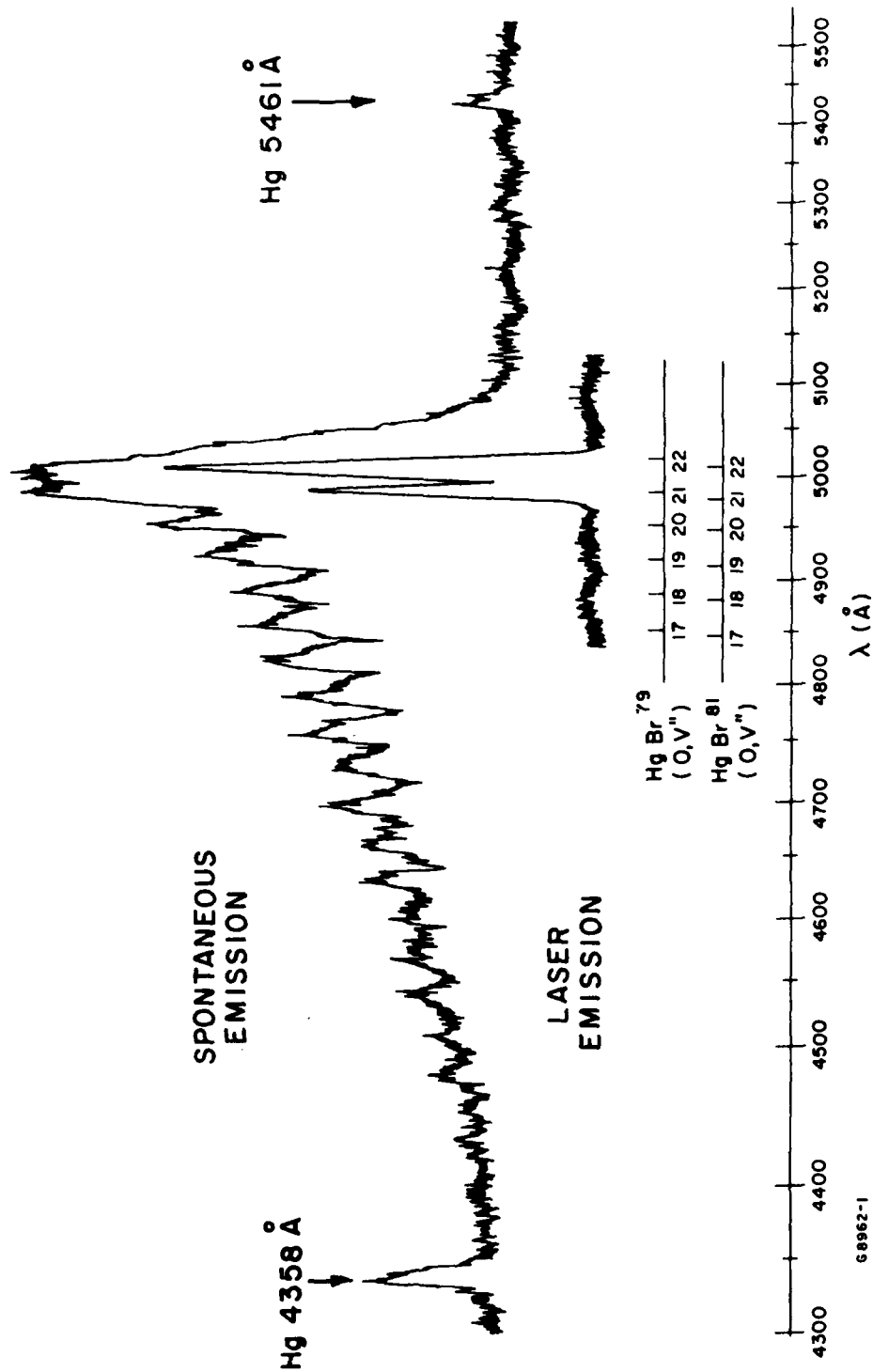
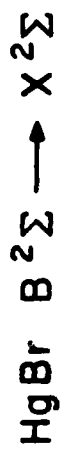


Figure 34. Mercury Bromide Laser Emission and Spontaneous Emission Spectra

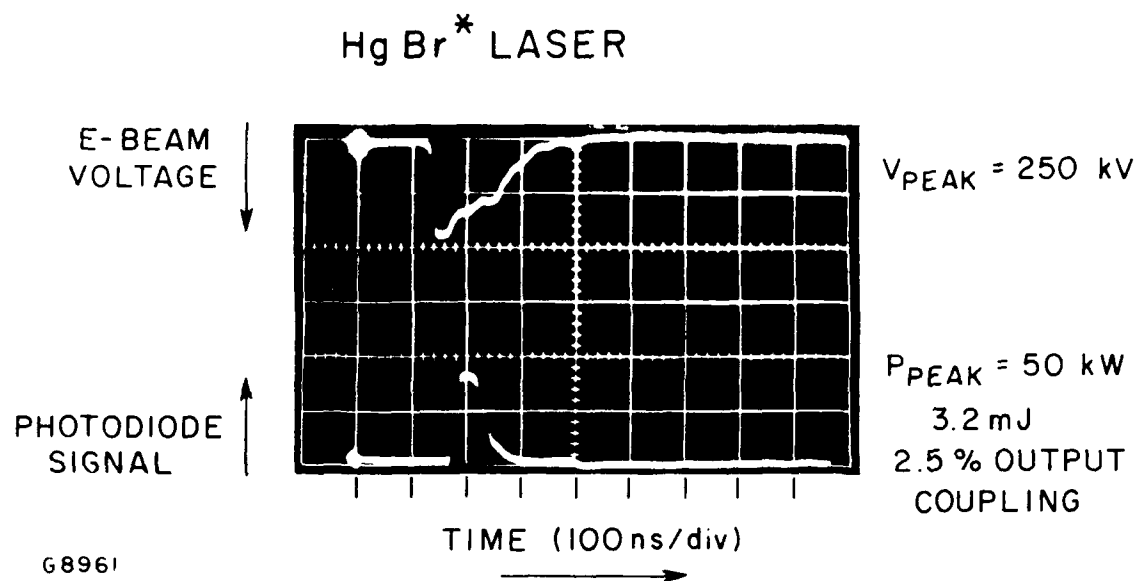


Figure 35. HgBr Data Oscillogram Trace Showing the E-Beam Voltage Pulse and the Corresponding Photodiode Laser Signal

TABLE 10. HgBr LASER CHARACTERISTICS

• WAVELENGTH	5018 Å
• GAS MIXTURE	
	Ar/Xe/Hg/HBr = 86.4%/10.8%/2.0%/.8%
	Ar -- 3 AMAGATS
CELL TEMPERATURE	275°C
• E-BEAM ENERGY DEPOSITION	3J
• INTRINSIC EFFICIENCY	0.25%
	(2.5% COUPLING)
• PEAK POWER	60 kW
• PULSEWIDTH	100 nsec

E. HgX* FORMATION KINETICS

A detailed study of the HgCl and HgBr molecular kinetics with e-beam excitation has not yet been performed. However, we will summarize the relative importance of several formation channels of HgCl* which are consistent with lasing and fluorescence data. These kinetics are summarized in Table 11.

1. Ion-Ion Recombination

The dominant formation channel of HgCl* under our excitation conditions is the rapid three-body recombination of Hg^+ ions with Cl^- ions. The suggested ion-ion kinetic channeling is outlined in Figure 36. In gas mixtures containing high-pressure xenon, the high-energy beam electrons deposit most of their energy into the formation of Xe^+ . The xenon ions and neutrals form Xe_2^+ with a three-body rate constant of $3.6 \times 10^{-31} \text{ cm}^6/\text{s}$.⁽⁶⁷⁾ The Xe_2^+ can then undergo charge transfer with Hg to form Hg^+ which is energetically near resonance, $\Delta E = 0.8 \text{ eV}$ (exothermic). This reaction may exhibit a comparable rate⁽⁶⁸⁾ to an analogous, near resonant charge transfer reaction involving Ar_2^+ and Kr which forms Kr^+ with a rate constant of $7.5 \times 10^{-10} \text{ cm}^3/\text{s}$.⁽⁶⁹⁾ The Cl^- ions is formed by rapid dissociative attachment⁽⁷⁰⁾ of secondary electrons to CCl_4 . The HgCl* ionic state is then formed by ion-ion recombination of Hg^+ and Cl^- which can have an effective two body rate constant of $10^{-6} \text{ cm}^3/\text{s}$ at pressure of interest.⁽⁷¹⁾ In the Ar/Xe gas mixtures, the observed increase in HgCl* fluorescence is consistent with an enhanced formation of Hg^+ . This could occur via additional charge transfer reactions involving Ar_2^+ and Xe which increase Xe_2^+ density and the Hg^+ as discussed above.

2. Exchange Reactions and Interception

Fluorescence spectra obtained from Ar/Hg/ CCl_4 and Xe/Hg/ CCl_4 mixtures clearly indicate the formation of ArCl* and XeCl*. Displacement reactions can follow in which mercury exchanges with these excited molecules to form HgCl* as shown in Figure 37.

TABLE 11. HgCl* KINETICS ACTIVE IN Ar/Xe/Hg/CCl₄
E-BEAM PUMPED MIXTURES

ION-ION RECOMBINATION

$e + Ar$	$\rightarrow Ar^+ + e + e_s$	$10^{23} cm^{-3} sec^{-1}$
$Ar^+ + 2Ar$	$\rightarrow Ar_2^+ + Ar$	$2.5 \times 10^{-31} cm^6 sec^{-1}$
$Xe^+ + 2Xe$	$\rightarrow Xe_2^+ + Xe$	$3.6 \times 10^{-31} cm^6 sec^{-1}$
$Ar_2^+ + Xe$	$\rightarrow ArXe^+ + Ar$	} $\sim 2 \times 10^{-10} cm^3 sec^{-1}$
$ArXe^+ + Xe$	$\rightarrow Xe_2^+ + Ar$	
$Xe_2^+ + Hg$	$\rightarrow Hg^+ + 2Xe$	$\sim 3 \times 10^{-10} cm^3 sec^{-1}$

$e_s + Ar_2^+$	$\rightarrow Ar^{**} + Ar$	$6 \times 10^{-7} cm^3 sec^{-1}$
$e_s + Xe_2^+$	$\rightarrow Xe^{**} + Xe$	$2 \times 10^{-7} cm^3 sec^{-1}$
$Ar^+ + 2Ar$	$\rightarrow Ar_2^+ + Ar$	$10^{-32} cm^6 sec^{-1}$
$Xe^+ + 2Xe$	$\rightarrow Xe_2^+ + Xe$	$5 \times 10^{-32} cm^6 sec^{-1}$

$e_s + CCl_4$	$\rightarrow Cl^- + CCl_3$	$10^{-7} cm^3 sec^{-1}$
$Hg^+ + Cl^- + Ar$	$\rightarrow HgCl^* + Ar$	$\sim 10^{-6} cm^3 sec^{-1}$
$HgCl^*$	$\rightarrow h\nu (5576 \text{ \AA}) + HgCl$	22 nsec

EXCHANGE REACTION

$Ar^+ + Cl^- + Ar$	$\rightarrow ArCl^* + Ar$	} $\sim 10^{-6} cm^3 sec^{-1}$
$Ar_2^+ + Cl^-$	$\rightarrow ArCl^* + Ar$	
$ArCl^*$	$\rightarrow h\nu (1750 \text{ \AA}) + Ar + Cl$	10 nsec
$Xe^+ + Cl^- + Ar$	$\rightarrow XeCl^* + Ar$	} $\sim 10^{-6} cm^3 sec^{-1}$
$Xe_2^+ + Cl^-$	$\rightarrow XeCl^* + Xe$	
$XeCl^*$	$\rightarrow h\nu (3080 \text{ \AA}) + Xe + Cl$	16 nsec
$Hg + ArCl^*$	$\rightarrow HgCl^* + Ar$	
$Hg + XeCl^*$	$\rightarrow HgCl^* + Xe$	

NEUTRAL REACTION

$Hg^* + CCl_4$	$\rightarrow HgCl^* + CCl_3$	$\sigma = 34 (\text{\AA})^2$
----------------	------------------------------	------------------------------

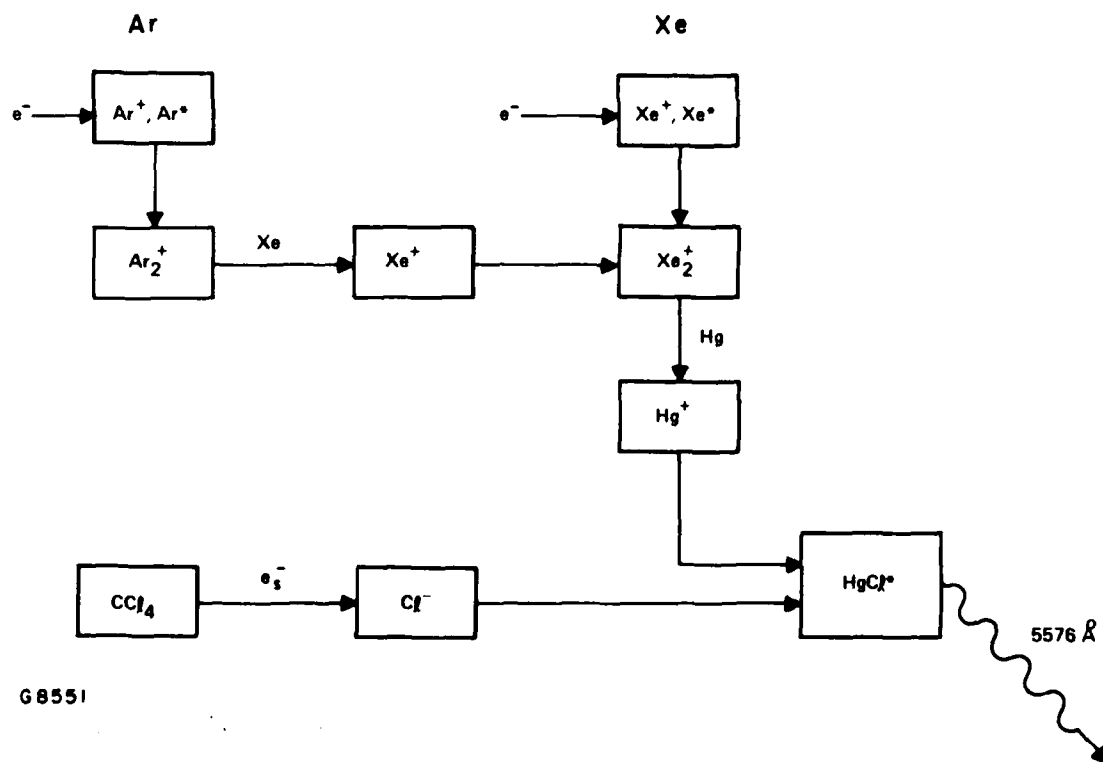
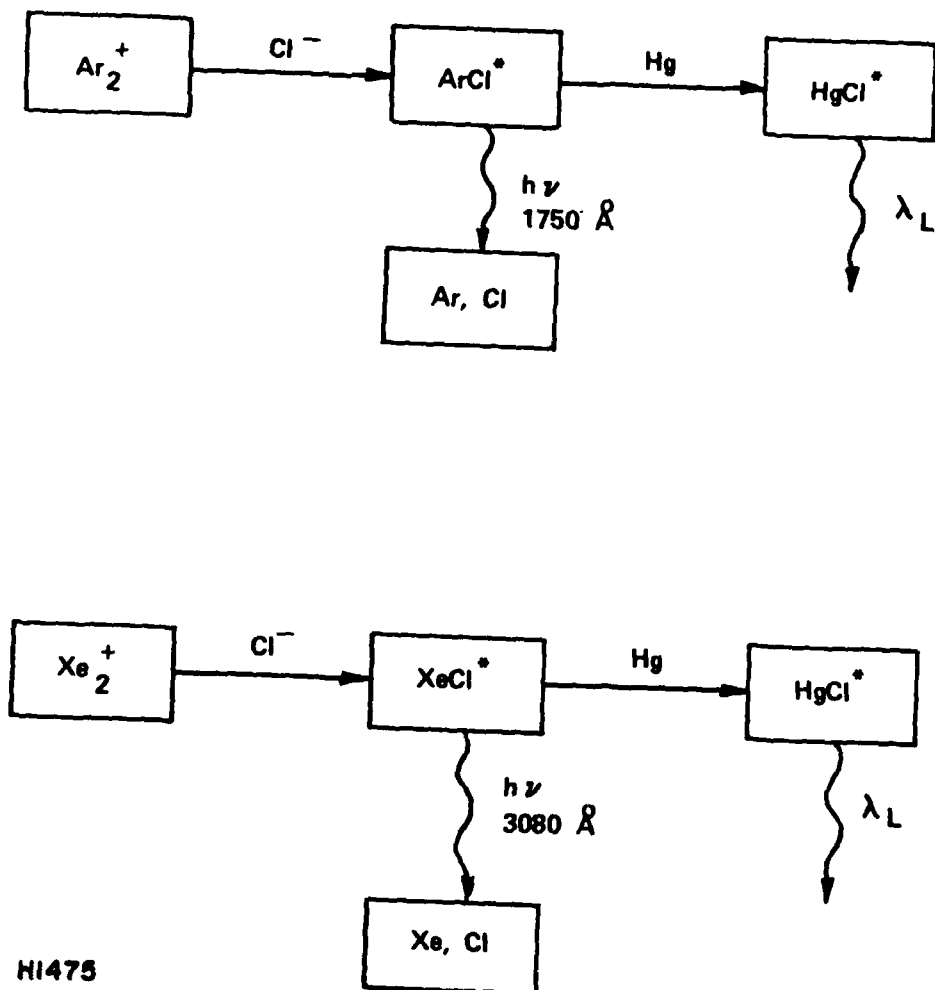


Figure 36. Ion-Ion Recombination Channel Suggested for HgCl^* Formation in Ar/Xe/Hg/CCl_4 Mixtures



HI475

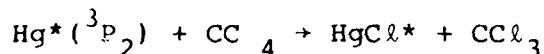
Figure 37. HgCl^* Formation via Exchange Reactions in Ar/Xe/Hg/ CCl_4 Mixtures

The rate constant for an analogous reaction involving Kr and ArF* has been measured⁽⁷²⁾ to be $6.5 \times 10^{-10} \text{ cm}^3/\text{sec}$. It is expected that XeCl* would be a more efficient precursor since dissociation to Xe + Cl* should have a smaller rate constant than the dissociation of ArCl* to Ar + Cl*. Although the relative importance of this HgCl* formation channel has not been determined, the competing radiative processes of ArCl* and XeCl* suggest that displacement reactions will not be dominant. A preliminary measurement of XeCl* quenching by Hg, performed in this program, indicates that the branching into HgCl* via $\text{XeCl}^* + \text{Hg} \rightarrow \text{HgCl}^* + \text{Xe}$ is between 10-50%.

The formation of a triatomic species, Kr₂F* in KrF laser mixtures has been observed.⁽⁷³⁾ In this case, the triatomic formation is saturable since Kr₂F* formation depends on the density of KrF* which is driven down by the intense laser flux. Similar processes could be present in mercury halide laser mixtures. If Hg₂Cl* is formed, it will probably fluoresce in the near infrared $\geq 7000 \text{ \AA}$.

3. Neutral Channels

The mercury metastable channel leading to HgCl* through reaction



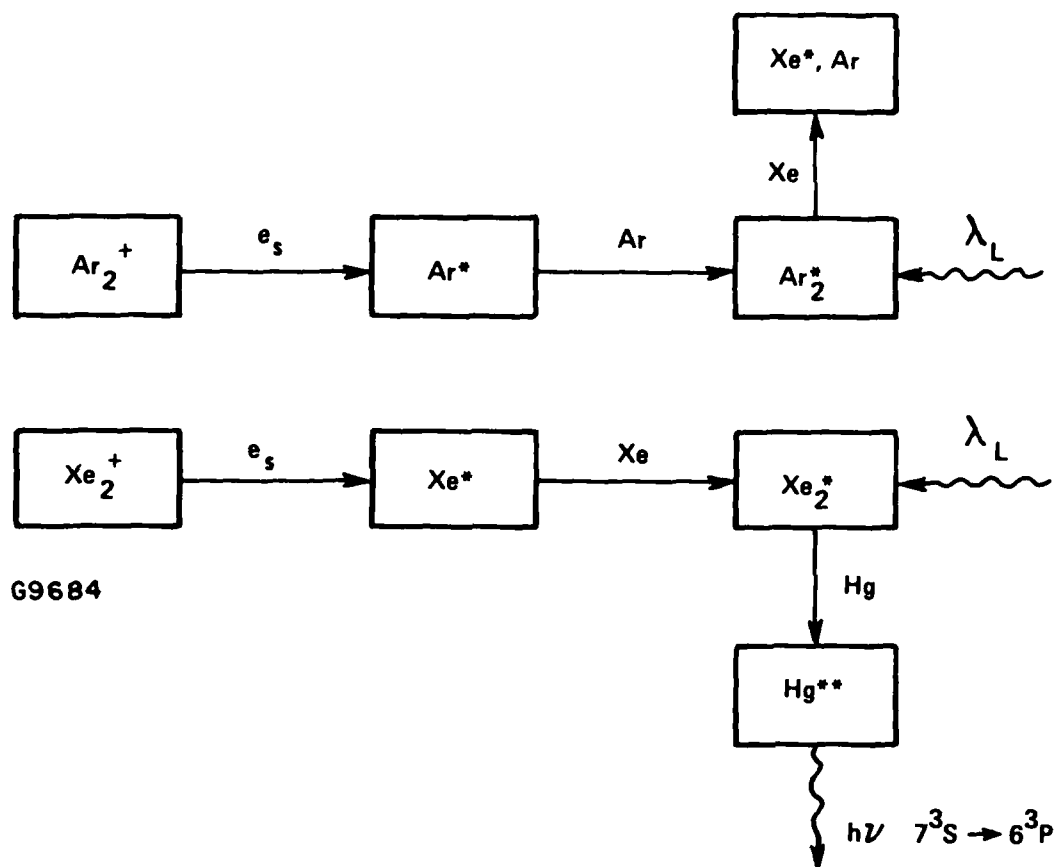
has been observed⁽⁶³⁾ to have a reactive cross section of $34 (\text{\AA})^2$ and a branching ratio into the upper laser level of near unity. Since the energies of the mercury metastables Hg*(6_p) are about 5 eV, this reaction suggests the possibility of efficient discharge pumping of HgCl*. However, this is probably not an important formation process for e-beam pumping. The fluorescence data from laser mixtures indicates only weak emission from higher lying mercury levels such as 7³S₁ which populate the 6³P metastables. When the CCl₄ density is decreased by an order of magnitude, to about 1 Torr, the emission from HgCl* shows a

comparable reduction but mercury emission from 7^3S_1 increases significantly. Thus, for laser gas mixtures the neutral channel kinetics do not appear to lead to efficient mercury metastable production under these excitation conditions. It is interesting to note that the use of HBr in HgBr lasing mixtures eliminates the Hg* metastable channel because the 3.8 eV H-Br bond strength renders the above neutral reaction endothermic by roughly .5 eV.

The absence of lasing in pure Ar mixtures and the observed weak lasing in pure Xe mixtures suggests the possibility that absorption by Ar_2^* and Xe_2^* may be competing with the $HgCl^*$ and $HgBr^*$ stimulated emission as outlined in Figure 38. The fluorescence from pure Ar and pure Xe mixtures were comparable for similar e-beam energy deposition. Strong visible absorption identified with these rare gas eximers has been observed⁽⁷⁴⁾ during e-beam excitation in high pressure Ar and also in Xe. However, in Ar/Xe/Hg/ CCl_4 gas mixtures the strong Ar_2^* absorption is possibly reduced via the rapid quenching^(75,76) of Ar_2^* by Xe.

4. HgX* Intrinsic Efficiency

Lasing on the $HgCl^*$ and $HgBr^*$ band transitions introduces new high-power laser sources at visible wavelengths. The detailed molecular kinetics in these gas mixtures have yet to be established in order to assess the possible efficiency and scalability of these lasers. The measured intrinsic efficiencies are the result of increased output coupling. The optimization of laser mixtures and pumping power presently underway should result in higher values. In pure e-beam pumping, the maximum effective quantum efficiency of 9% is limited by the 26 eV needed to form an argon ion. Thus, the observed value of 3.8% indicates efficient $HgCl^*$ formation. If a discharge were used to pump the Hg* (6_p) metastable levels directly and form HgX* via neutral reactions such as the effective quantum efficiency would be roughly 50%.



G9684

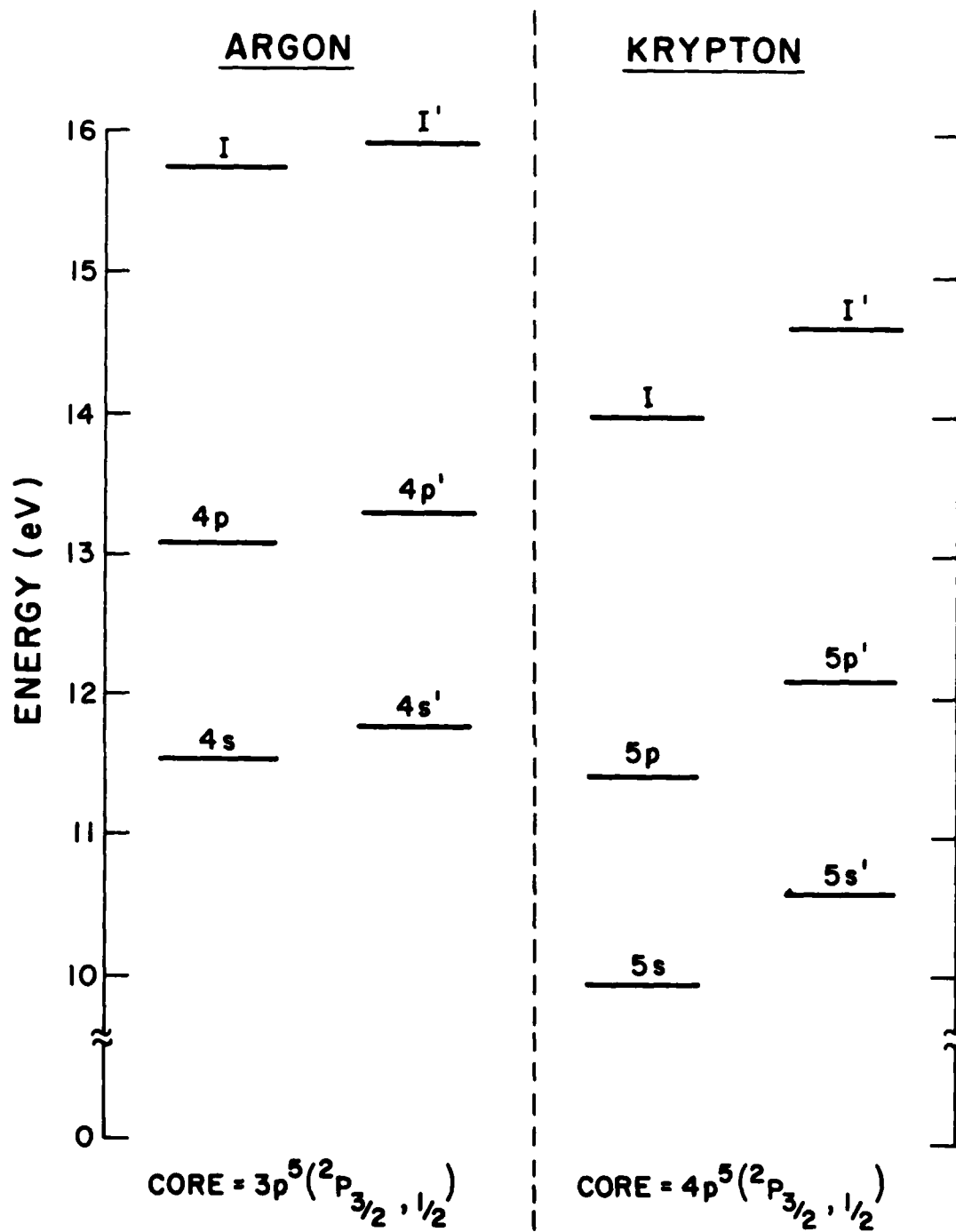
Figure 38. Suggested Formation Channels for Dominant Species which Absorb at the Laser Wavelength λ_L in Ar/Xe/Hg/ CCl_4 Mixtures

V. THEORETICAL EFFORT

A. RARE GAS METASTABLE PHOTOIONIZATION

In a typical laser mixture⁽⁷⁷⁾ consisting of $\sim 0.1\%$ $F_2/2\%$ Kr/ 97.9% Ar at atmospheric pressures, the most important photo-absorption processes in the KrF discharge laser are: (1) F_2 absorption, (2) photoionization of excited states of argon and krypton, and (3) possible absorption in the rare gas-halide "molecules" themselves. Absorption due to F_2 is fairly well understood,⁽⁷⁸⁾ and constitutes the major loss mechanism, while process (3) cannot be treated theoretically until accurate potential energy curves for the high-lying excited states of KrF and ArF are available. Photoionization of Ar^* and Kr^* is amenable to theory, and we have therefore calculated the relevant cross sections. Besides representing a loss mechanism for the $\lambda = 2486 \text{ \AA}$ laser radiation, the photoionization process produces additional free electrons, and may thus affect the discharge kinetics.

Partial energy level diagrams for argon and krypton are shown in Figure 39. Due to the large spin-orbit splitting in the core, the excited levels form two separate series, $np^5 \text{ } ^2P_{3/2} m_l'(J)$, converging toward two different ionization limits, I and I'. To simplify the calculation, we have averaged over the J-substates. When this is done, it is found that the binding energies, $I - E_{m_l}$ and $I' - E_{m_l}$, (which are the eigen-values required for determining the wavefunctions) are almost identical,⁽⁷⁹⁾ so that it is a good approximation to further average over the core states, $^2P_{1/2}$ and $^2P_{3/2}$. We then finally obtain the four excited states considered in the calculation: $Ar^* \equiv Ar(3p^5 4s)$, $Ar^{**} \equiv Ar(3p^5 4p)$, $Kr^* \equiv Kr(4p^5 5s)$, and $Kr^{**} \equiv Kr(4p^5 5p)$. The Ar^* and Kr^* states include the important metastable levels, while the Ar^{**} and Kr^{**} states are important due to the large cross sections for electron impact processes of the type



G3283

Figure 39. Partial Energy Level Diagrams for Argon and Krypton

$e + X^* \rightarrow e + X^{**}$ ($X = \text{Ar}, \text{Kr}$). Since the laser photon has an energy close to 5 eV ($\lambda = 2486 \text{ \AA}$), it is obvious from Figure 39 that all four states can be photoionized.

The cross section for photo-ionization of the m^{th} state is given by

$$\sigma(m^{\ell}) = 2.69 \times 10^{-18} (I_{m\ell} + \epsilon) \quad (3)$$

$$\left(\frac{\ell+1}{2\ell+1} R_{\ell+1}^2 + \frac{\ell}{2\ell+1} R_{\ell-1}^2 \right) (\text{cm}^2)$$

where $I_{m\ell}$ is the ionization energy and ϵ is the energy of the free electron [all energies are in Rydbergs (1 Ry = 13.6 eV)]. R is the radial matrix element, given by

$$R_{\ell \pm 1} = \int_0^{\infty} P_{m\ell}(r) r P_{\epsilon, \ell \pm 1}(r) dr, \quad (4)$$

and $P(r)$ is the solution of the radial Schrodinger equation.

$$\left[\frac{d^2}{dr^2} - \frac{\ell(\ell+1)}{r^2} + \epsilon + V(r) \right] P(r) = 0 \quad (5)$$

with $V(r)$ being the atomic potential. The differential Eq. (5) for the bound state $P_{m\ell}(r)$ and the continuum state $P_{\epsilon\ell}(r)$ is essentially the same, the main difference between the two being the boundary condition at $r \rightarrow \infty$:

$$\epsilon < 0, P_{m\ell}(r) \rightarrow 0 \quad (6)$$

$$\begin{aligned}
& > 0, P_{\ell+1}(r) \sim \epsilon^{-1/2} \epsilon^{-1/4} \sin \left[\epsilon^{1/2} r - i\pi/2 \right. \\
& \left. - 1/2 \ln(2\epsilon^{1/2} r) + \delta_{\ell}(\epsilon) + \delta_{\ell+1}(\epsilon) \right]
\end{aligned} \tag{7}$$

where $\delta_{\ell}(\epsilon) = \arg \Gamma(\ell + 1 - i\epsilon^{-1/2})$ and $\delta_{\ell}(\epsilon)$ is the phase shift. To solve Eq. (5), we must specify the potential, $V(r)$. We have adopted the central-field approximation, which is consistent with our method for obtaining the average excited-state energies; we thus obtain

$$V(r) = \frac{Z}{r} Y(r) + \frac{\alpha}{(r^2 + r_0^2)^2} \tag{8}$$

The first term in Eq. (8) is the central-field Hartree-Fock potential given by

$$Y(r) = Z - \sum_{\substack{n\ell \\ \text{(core)}}} \left[\int_0^r \psi_{n\ell}^2 dr' + r \int_r^{\infty} \psi_{n\ell}^2 dr' \right] \tag{9}$$

where Z is the nuclear charge, and the sum extends over all electrons in the ionic core. For the $\psi_{n\ell}$ we have used the analytic, Hartree-Fock functions of Clementi and Roetti.⁽⁸⁰⁾ The second term in Eq. (8) is the polarization potential,⁽⁸¹⁾ with α being the core polarizability and r_0 representing a cutoff radius. The core polarizabilities for Ar and Kr have not been measured or calculated, and we therefore used the scaling law⁽⁸²⁾ $\alpha \sim Z r_0^4$ to obtain the required values from the known^(83,84) polarizabilities of the alkali ions and halogens. The value of r_0 was taken to be the mean radius of the outer shell of the core:

$$r_0 = \bar{r}_{np} \int_0^{\infty} [\psi_{np}(r)]^2 r dr \quad (10)$$

where again ψ_{np} is the Hartree-Fock wavefunction⁽⁸⁰⁾ of the outer np electron. The final values used in $V(r)$ were: for the Ar core, $r_0 = 1.559 a_0$ and $\alpha = 8.85 a_0^3$, and for the Kr core, $r_0 = 1.843 a_0$ and $\alpha = 14.9 a_0^3$ (where a_0 is the Bohr radius).

The Schrodinger Eq. (5) was solved numerically for $P(r)$, and the cross section (1) was calculated over a range of energies. The results are shown in Figures 40 and 41, where the cross sections (in cm^2) are plotted against the free-electron energy (in Ry). In Figure 40, the solid curves represent the calculated cross sections for $\text{Ar}^* [\sigma(4s)]$ and $\text{Ar}^{**} [\sigma(rp)]$, while Figure 41 shows the cross section for $\text{Kr}^* [\sigma(5s)]$ and $\text{Kr}^{**} [\sigma(5p)]$. The results are very similar to the photo-ionization cross sections of the analogous alkali atomic states. The $\text{Ar}^* (4s)$ and $\text{Kr}^* (5s)$ curves both have the characteristic alkali-like minimum⁽⁸⁵⁾ just above threshold, where the matrix element, R , changes sign. Although, in the present approximation the cross sections go to zero, it is known⁽⁸⁵⁾ that the minimum has in fact a small non-zero value due to spin-orbit effects in the continuum. Again, as in the case of the alkalis, the cross sections for the next higher Ar^{**} and Kr^{**} p states are much larger than for the s states. This similarity between the rare gas excited states and the alkalis is not surprising, since the respective binding energies are almost identical. In addition, the rare gas metastables and corresponding alkalis have very similar polarizabilities.⁽⁸⁶⁾ Finally, the entire ionic-bonding structure of the rare gas-halide upper laser level is in direct analogy with the properties of the alkali-halides.⁽¹⁷⁾

To our knowledge, no data or previous calculations exist for these cross sections. Dunning and Stebbings⁽⁸⁷⁾ have reported measured values for the upper limit of the photo-ionization

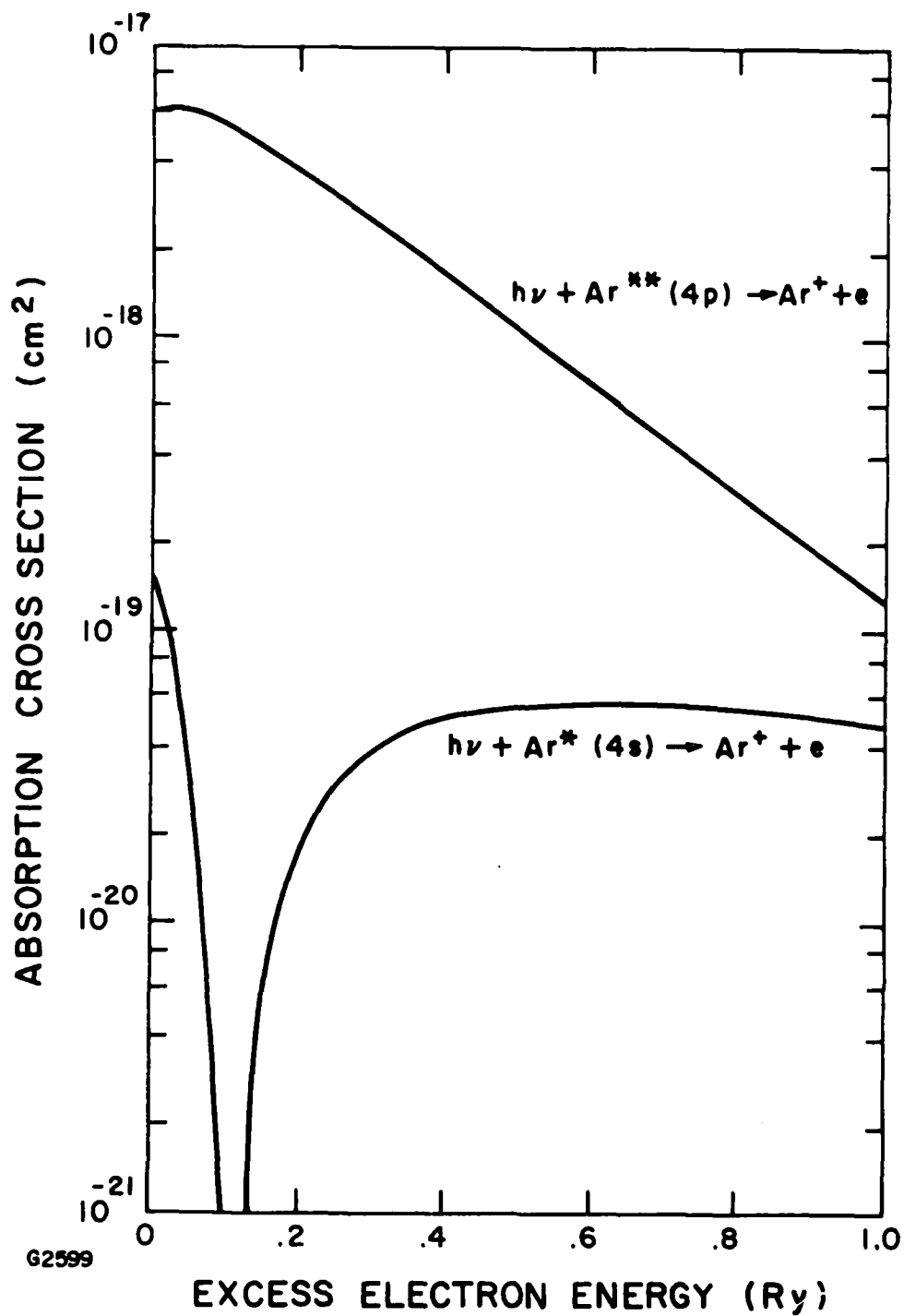


Figure 40. Photoionization Cross Sections for the Ar^* State, $\sigma(4s)$, and the Ar^{**} State, $\sigma(4p)$. The dashed curve represents the renormalized theory for Ar^* (see text).

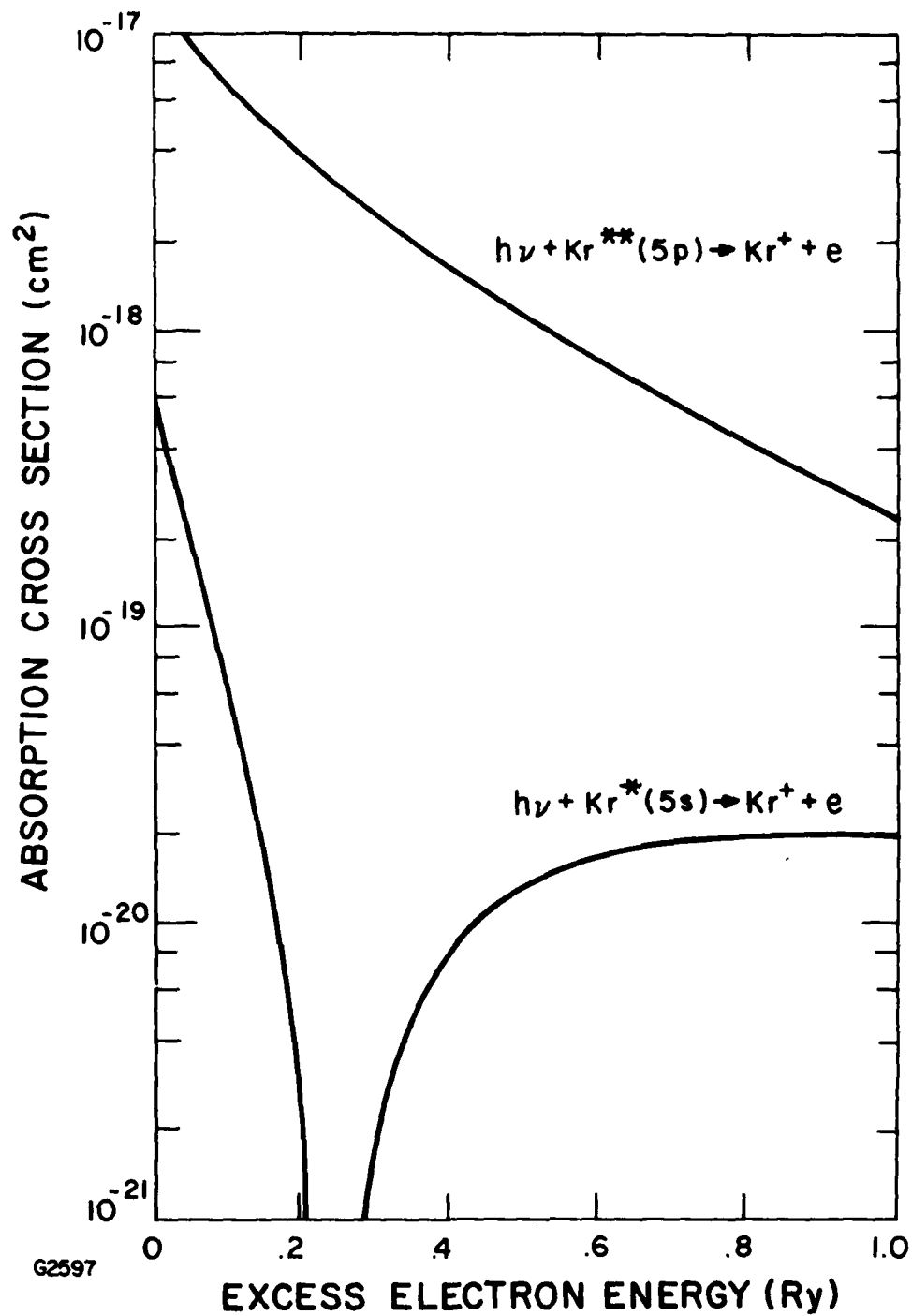


Figure 41. Photoionization Cross Sections for the Kr^* State, $\sigma(5s)$ and the Kr^{**} State, $\sigma(5p)$

cross sections at threshold for the Ar* and Kr*, $^3P_{0,2}$ metastable states, and these values are shown as the open circles in Figures 40 and 41. Although these are only upper limits, their accuracy is considered to be better than a factor of two,⁽⁸⁸⁾ and so they allow some comparison to be made between the theory and experiment. The agreement is very good for Kr*, but the Ar* theoretical value is considerably too low. Further analysis indicates that the calculations for the Ar* and Kr*, s state cross sections are extremely sensitive to the details of the model, particularly near threshold where the cross section is falling rapidly to zero. This, however, is not the case for the Ar** and Kr**, p state calculations. They are quite insensitive to the detailed model and therefore the theoretical values should be reliable. To obtain the absorption coefficient, we have renormalized the Ar* theoretical curve so as to agree with the experimental, upper-limit value at threshold. The dashed curve in Figure 40 represents the renormalized theory, extrapolated to $\epsilon = 0.061$ Ry ($\lambda = 2486 \text{ \AA}$). The other curves are sufficiently accurate so that they do not require further adjustment. The key result of the calculation is that, at $\lambda = 2486 \text{ \AA}$, the ratio of p state to s state cross sections is $\sim 30:1$, so that if the X** state (X = Ar, Kr) is significantly populated in the discharge, it will dominate the photo-ionization process.

To calculate the absorption length in the laser due to photo-ionization, it is necessary to know the population of the various excited states for the appropriate discharge conditions. Since this information is not available, we have plotted in Figure 42 the absorption length L (in cm) at $\lambda = 2486 \text{ \AA}$ vs the total excited-state number density $N(s) + N(p)$ (in cm^{-3}) for various possible relative populations. Defining

$$\eta = \frac{N(p)}{N(s)} \equiv \frac{[X^{**}]}{[X^*]} \quad (X = \text{Ar, Kr}) \quad (11)$$

we show in Figure 42 the results for $\eta = 0.01, 0.1$ and 1.0 for argon (dashed lines) and krypton (solid lines). It is estimated that $0.1 < \eta < 1$ and $N(s) + N(p) \sim 5 \times 10^{14} \text{ cm}^{-3}$ for both argon and krypton combined, so that $L \sim 2 \times 10^3 \text{ cm}$, giving an absorption of $\sim 5\%/m$ per pass; this is within a factor of 2 of the F_2 absorption loss. Since the major absorption due to the photo-ionization process is due to the X^{**} state, it is desirable to operate at fairly low values of $[X^{**}]/[X^*]$.

To summarize, we have calculated the photo-ionization cross sections for several excited states of argon and krypton. The absorption loss due to this process is found to be significant under typical discharge laser operating conditions, but the effect can be minimized by running at relatively low excited-state densities, a condition that is compatible with discharge stability. (89)

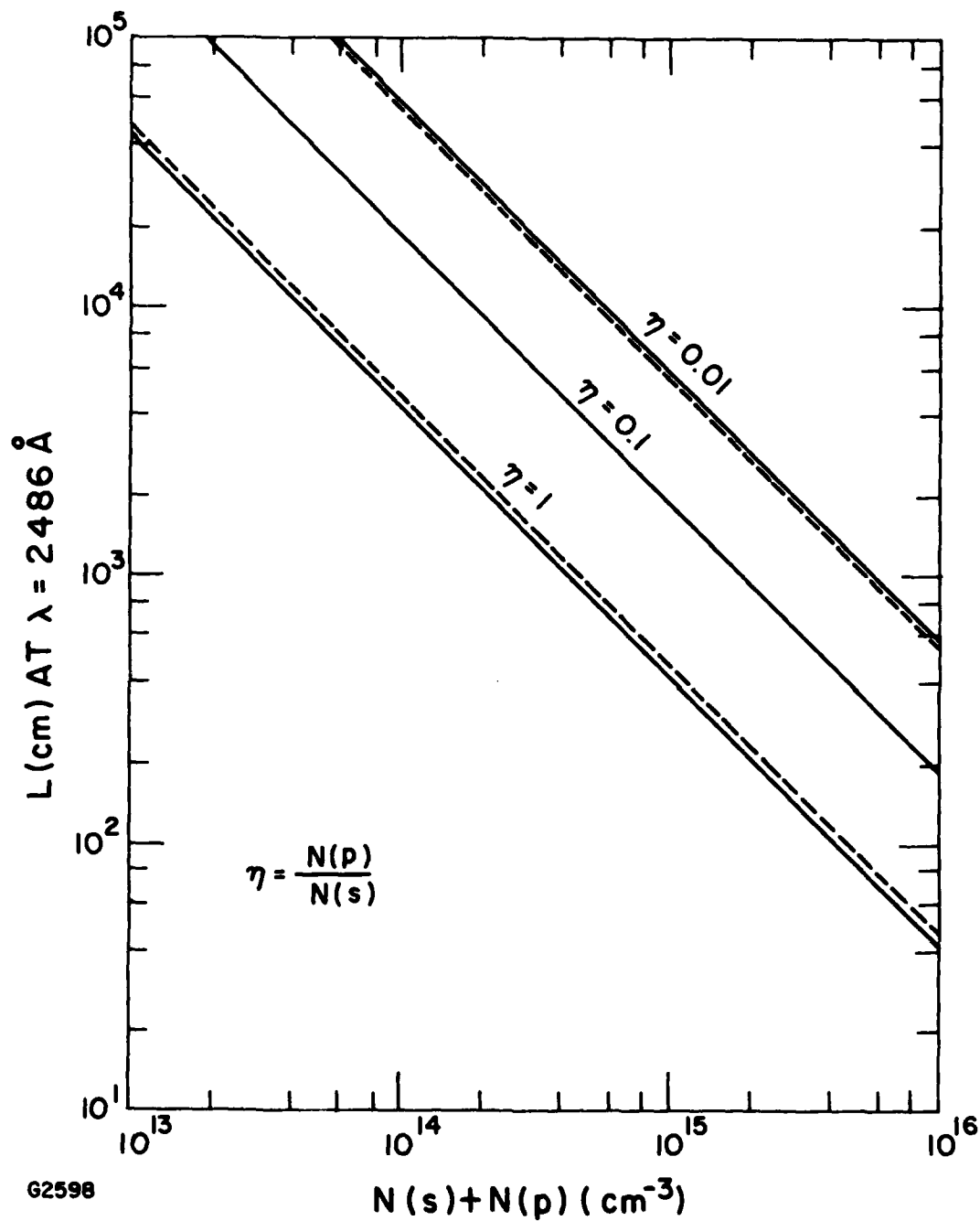


Figure 42. Absorption Length at $\lambda = 2486 \text{ \AA}$ vs Total Excited-State Number Density. The dashed lines are for argon and the solid lines for krypton.

B. MERCURY HALIDE RADIATIVE LIFETIMES

This section will discuss the application of a charge transfer model to calculate the oscillator strengths and radiative lifetimes for the mercury-monohalide laser transitions $B^2\Sigma_{1/2}^+ - X^2\Sigma_{1/2}^+$. To our knowledge, no previous calculations of the radiative lifetimes of these systems have been attempted. Dunning and Hay⁽⁹⁰⁾ have performed ab initio calculations for KrF, in which they computed both the potential energy curves and oscillator strengths. Their calculation involved an extensive configuration-interaction treatment, utilizing between 2000-3000 configurations. Although such calculations are valuable, they are enormously time consuming and must be applied individually to each state of each rare gas-halide pair. This approach is clearly not in a form from which general conclusions can be drawn and applied to the whole class of rare gas-halide systems. It would therefore be desirable to have available a simpler model, from which one can make fairly reliable predictions for a wide range of systems. The simple charge transfer theory developed originally by Mulliken⁽⁹¹⁾ and used by Zare and Herschbach⁽⁹²⁾ for the alkali halides, appears to be a scheme capable of being generalized to a wide variety of systems for which the "ionic-bonding" model holds, including the alkali halides, rare gas-halides, and mercury-monohalides. The alkali-halide analogy has been extremely successful⁽¹⁷⁾ in predicting the properties of the rare gas-halides, and the use of the charge transfer model to calculate the transition strengths can be thought of as simply an extension of the analogy.

The basic idea behind the charge transfer theory is that the electron initially localized around the halogen center, in the upper M^+X^- state, "jumps" or is transferred to the mercury positive ion, filling the p-state vacancy, and thus ending up in the MX atomic ground state. This is essentially a "valence bond" picture, in which the electron is transferred from one atomic center to the other. For example, in the mercury chloride

B → X transition an electron which is initially localized on the Cl atom, forming Cl^- , is transferred to the Hg^+ ion resulting in the ground state configuration of mercury chloride.

In general, the mercury-halides are closely analogous in structure to the rare gas-halides. The upper laser level is "ionic", while the ground state is primarily "atomic". There are, however, some significant differences between the two systems. The upper level of the mercury-halides correlates with the $\text{Hg}^+(^2\text{S}_{1/2}) + \text{X}^-(^1\text{S}_0)$ atomic states so that only a single $^2\Sigma_{1/2}$ ionic state is formed. The ground state correlates with the $\text{Hg}(^1\text{S}_0) + \text{X}(^2\text{P}_{3/2, 1/2})$ atomic limit, so that we obtain $^2\Pi_{1/2}$ and $^2\Sigma_{1/2}$ molecular states, as in the case of the rare gas-halides. A more important difference is that the ground states of the mercury-halides are essentially bound states with the binding energy ranging from⁽⁹³⁾ 0.36 eV for HgI to 1.04 eV for HgCl . With the exception of XeF , which is slightly bound, all of the rare gas-halide ground states are repulsive.

Although the upper and lower states are predominantly ionic and covalent, respectively, it proves to be essential to allow for mixing between these states in order to obtain reasonable results from the theory. The mixed X and B state wavefunctions can be expressed as

$$\begin{aligned}\psi_B &= N_B (\psi^i + \alpha \psi^c), \\ \psi_X &= N_X (\psi^c - \beta \psi^i),\end{aligned}\tag{12}$$

with $\alpha = (\beta - S)/(1 - \beta S)$, and where ψ^i and ψ^c are the purely ionic and covalent wavefunctions, N_B and N_X are normalization constants, S is the overlap integral between ψ^i and ψ^c , and β is the mixing coefficient. Except for very large values of the internuclear distance, S is non-zero so that S as well as β must appear in the expression for α in order to make the

initial and final wavefunctions orthogonal. A major difficulty in the theory is the specification of the mixing parameter β . Given the lack of data on the mercury-monohalides, we have used the procedure outlined by Coulson⁽⁹⁴⁾ to estimate the degree of ionic character of the ground state from the electronegativities of the mercury and halogen atoms. The values for the percent ionic character [i.e., $100 \beta^2 / (1 + \beta^2)$] obtained in this way are given in Table 12. The electronegativities can also be used to determine the so-called covalent-ionic resonance energy, Δ , which is simply the ionic contribution to the binding energy. The values of Δ (in eV) turn out to be 1.2, 0.81, and 0.36 for HgCl_2 , HgBr , and HgI , respectively, as compared to the experimental dissociation energies (in eV) of 1.0, 0.7, and 0.36. It may thus be inferred that the electronegativity method tends to overestimate the mixing parameter.

In order to complete the definition of the wavefunctions in Eq. (12) it remains to determine the one-electron orbitals that make up ψ^c and ψ^i . In keeping with the valence bond picture we have adopted, ψ^c and ψ^i are simply taken to be products of unperturbed atomic (ionic) wavefunctions. The analytic Hartree-Fock functions of Clementi and Roetti⁽⁹⁸⁾ were used for the atomic and ionic halogen wavefunctions. Unfortunately, no such functions exist for neutral or singly-ionized mercury. A further complication arises from the fact that relativistic effects are non-negligible for the mercury valence orbital. Since the valence electrons are in an s-state, the most important relativistic effect⁽⁹⁹⁾ is a contraction of the radial wavefunction toward the nucleus, due to the absence of a repulsive angular momentum barrier. We have therefore calculated a non-relativistic Hartree-Fock-Slater (HFS) wavefunction, utilizing the Herman-Skillman computer program,⁽¹⁰⁰⁾ and scaled the function according to the formula

$$P'(r) = \gamma^{1/2} P_{\text{non-rel.}}(\gamma r)$$

TABLE 12. PARAMETERS FOR THE B \rightarrow X TRANSITION IN THE Hg-HALIDES

	α	β	S	x^2_{Σ} Percent Ionic Character	B^2_{Σ} Internuclear Equilibrium Distance(\AA)	$\lambda(\text{\AA})$	$\mu(\text{Debye})$	τ (nsec)		Ref.
								Theory	Expt.	
HgCl	-.64	.53	.87	22	3.15	5576	-6.60	20	22.2	(95)
HgBr	-.59	.45	.82	17	3.24	5018	-6.32	16	23.7	(96,97)
HgI	-.51	.35	.73	11	3.50	4412	-5.92	12	27.3	(97)

so as to reproduce the expectation values $\langle r^n \rangle$ tabulated by Lu et al,⁽¹⁰¹⁾ from their relativistic HFS program. The calculation was made for $n = -1, 1, 2$ and in all cases $\gamma \approx 1.16$ for Hg; the same value was used for Hg^+ . The final function, $P'(r)$, were then represented by a sum of Slater-type orbitals (STOs) using a nonlinear least squares fitting procedure. The basis set for the 6s functions of Hg and Hg^+ consisted of eight STOs.

With the wavefunctions given in Eq. (12), the transition dipole moment can be reduced to an expression involving only one-electron terms. Consider that the ionic and covalent molecular wavefunctions ψ^i and ψ^c are expressed in terms of products of atomic wavefunctions ϕ for Hg, Hg^+ , X and X^- ($X = \text{Cl}, \text{Br}, \text{I}$) by

$$\begin{aligned}\psi^i &= (\phi_{\text{Hg}}^+) (\phi_X^-) \\ \psi^c &= (\phi_{\text{Hg}}) (\phi_X).\end{aligned}\tag{13}$$

These atomic wavefunctions ϕ are represented by Hartree-Fock functions composed of products of one-electron wavefunction, ϕ . Then, the transition dipole moment μ can be shown to be given by

$$\begin{aligned}\mu &= N_B N_X [\langle \phi_{\text{Hg}} | r | \phi_X^- \rangle (1-\alpha\beta) \chi \\ &\quad + \alpha \langle \phi_{\text{Hg}} | r | \phi_{\text{Hg}} \rangle - \beta \langle \phi_X^- | r | \phi_X^- \rangle],\end{aligned}\tag{14}$$

where ϕ_X^- is the initial wavefunction of the active electron centered on the negative halogen ion (X^-), ϕ_{Hg} is the final state one-electron wavefunction, r is the position vector, and χ is an overlap integral involving all of the electron orbitals not involved in the transition. All two-center integrals were evaluated from an expansion developed by Sharma⁽¹⁰²⁾ for the case of one-electron wavefunctions expressed as a sum of STOs.

The calculation of the overlap function $S = \langle \psi^i | \psi^c \rangle$ and the parameter α for various mercury monohalides are given in Table 12. All these calculations depend on a choice of molecular internuclear separation. An experimental value for the equilibrium internuclear distance exists⁽¹⁰³⁾ for the ionic state of HgCl, but not for the other halides. In order to estimate these distances, the relative sizes of the alkali halides were used as a guide. It was found that the internuclear separation of the alkali bromides are $\approx 3\%$ larger than those of the alkali chlorides while the iodides are $\approx 12\%$ larger. The internuclear distances of the Hg-halides were scaled accordingly, and are given in Table 12.

The results of the calculations for the B \rightarrow X transitions are summarized in Table 12. The radiative lifetime of the transition is given, in terms of the quantity μ , by $\tau = 3h\lambda^3/64\pi^4\mu^2$ where λ is the transition wavelength. The model predicts a decrease in lifetime with increasing halogen size due to the λ^3 dependence. There is a competing trend caused by a decrease in the dipole matrix element, but this effect is much weaker. In Table 12, we also show results of experimental measurements of the HgX radiative lifetimes. Theory and experiment are in good agreement for HgCl. The theoretical value is only $\sim 30\%$ lower than the measured value for HgBr and $\sim 50\%$ lower for HgI which is quite satisfactory considering the simplicity of the model. Further calculations were carried out to test the sensitivity of the results to the various parameters. When the internuclear distance was varied by 5%, the lifetime changed by less than 5% in all cases. As discussed earlier, the mixing coefficients are the parameters which contain the greatest uncertainty. To give some idea of the sensitivity of our calculation to the percent ionic character of the ground state, the radiative lifetime of each mercury monohalide is plotted as a function of the mixing coefficient in Figure 43. The value of the mixing coefficient inferred from the electronegativity is indicated for each molecule in

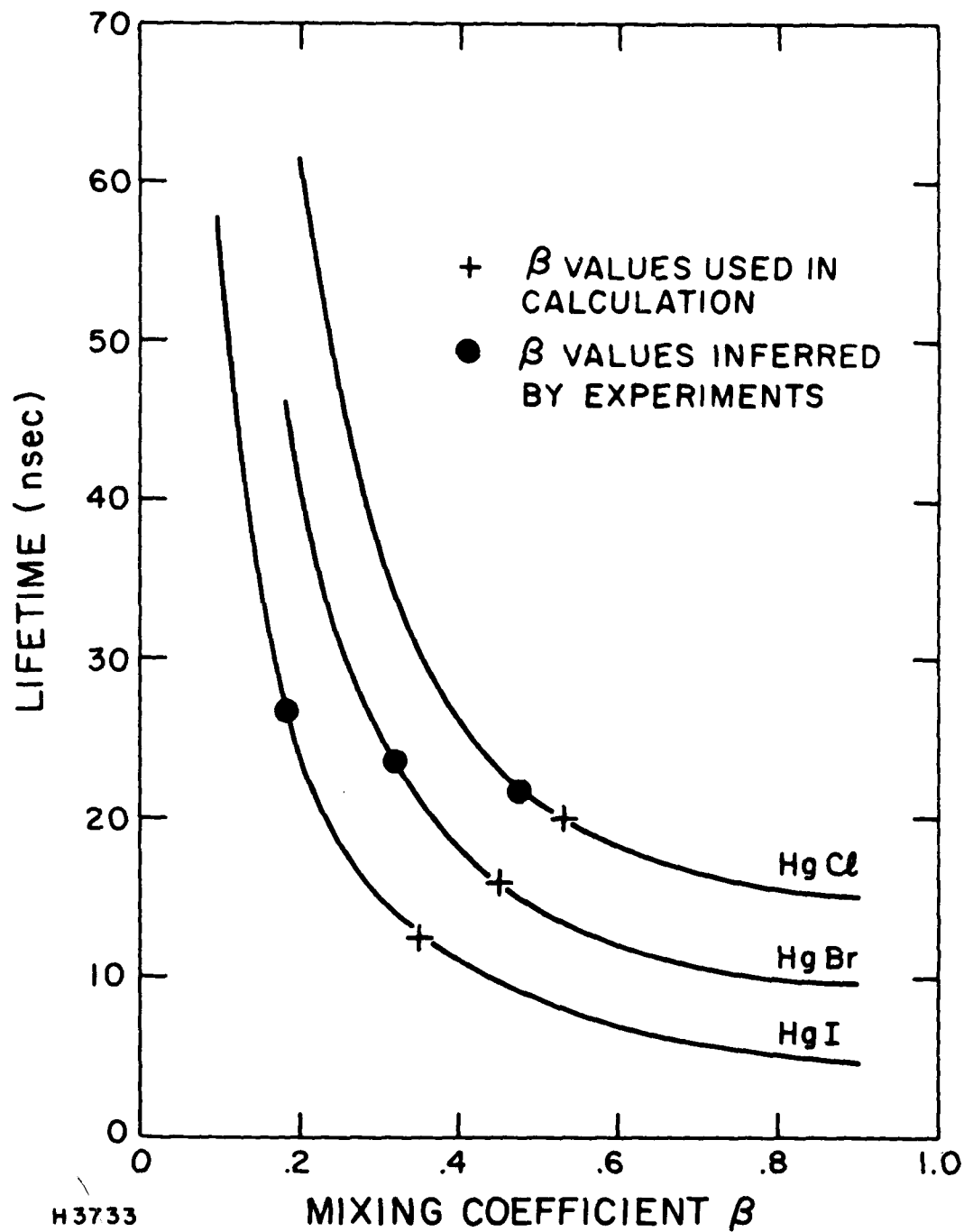


Figure 43. $B \rightarrow X$ Radiative Lifetime of HgX^* as a Function of the Ionic Mixing Coefficient, β

Figure 43 by the cross. From our earlier arguments, we expect these mixing coefficients in Table 12 to be overestimates, so that from Figure 43 the calculated lifetimes are expected to be somewhat too small. This is consistent with the comparison between theory and experiment for HgBr and HgI. The sensitivity of the radiative lifetime to a variation of the mixing coefficient β can be estimated from Figure 43. The β values used in the calculation are observed to be larger than the β values inferred by the experimental measurements consistent with earlier discussion.

Finally, an estimate of the importance of effects such as HgX* polarization and the broadband emission spectrum were considered and are included in Ref. 104. It should be pointed out that spin-orbit effects have been neglected. While this effect is expected to be small for HgCl, it may become more important for the heavier halides HgBr and in particular HgI.

VI. INTERHALOGEN RESEARCH

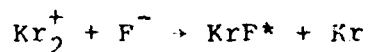
This section discusses interhalogen research carried out under this contract. The primary accomplishments are summarized in Table 13. The section will first develop the motivation for interhalogen research and proceed to describe the analytical model and experimental results.

A. CRITERIA FOR LASER CANDIDATES

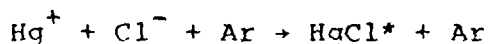
Experience gained from the rare gas and mercury monohalide lasers suggests several important criteria by which new laser candidates can be considered. These criteria are summarized in Table 14.

- Molecular excited states which are ionic in character provide the advantage of formation via long range reactive collisions which efficiently channel into the upper laser level.

For example, formation processes for the ionic states of HgCl^* and KrF^* include ion-ion recombination:



$$k \sim 2-3 \times 10^{-6} \text{ cm}^3/\text{sec}$$



$$k \sim 2 \times 10^{-6} \text{ cm}^3/\text{sec}$$

neutral reactions:

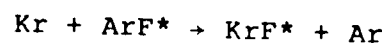


$$k = 8 \times 10^{-10} \text{ cm}^3/\text{sec}$$

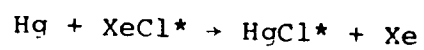


$$k = 3.8 \times 10^{-10} \text{ cm}^3/\text{sec}$$

and also replacement collisions:



$$k = 5 \times 10^{-10} \text{ cm}^3/\text{sec}$$



$$k \sim 3 \times 10^{-10} \text{ cm}^3/\text{sec}$$

TABLE 13. SUMMARY OF INTERHALOGEN RESEARCH

- FORMATION OF INTERHALOGEN SPECIES ICl^* , IBr^* , BrCl^* , BrF^*
IN ARGON/HALOGEN DONOR MIXTURES
 - EXCITED SPECIES DENSITY $10^{13} - 10^{14} \text{ cm}^{-3}$
 - EMISSION WAVELENGTHS 300 nm - 450 nm
 - FLUORESCENCE EFFICIENCY 1 - 3%
- INTERHALOGEN IONIC MODEL CALCULATED
 - TRANSITION WAVELENGTHS ESTIMATED
 - EXPERIMENTAL AGREEMENT WITHIN 10%
- NEUTRAL FORMATION CHANNEL OBSERVED IN ARGON MIXTURES
- ION-ION FORMATION CHANNEL PREDICTED FOR NEON MIXTURES

TABLE 14. CRITERIA FOR NEW LASER CANDIDATES

- IONIC UPPER LASER LEVEL
 - EFFICIENT FORMATION CHARACTERIZED BY LARGE CROSS SECTIONS AND NEAR UNIT BRANCHING RATIOS

- COVALENT/REPULSIVE OR SLIGHTLY BOUND LOWER LASER LEVEL
 - DEPLETION BY THERMAL DISSOCIATION (XeF)
IF SLIGHTLY BOUND ($T_g \geq \frac{1}{20} D_e$)
 - LARGE DIFFERENCE IN INTERNUCLEAR SEPARATION (HgCl)
VIBRATIONAL RELAXATION

- POSITION OF ATOMIC/MOLECULAR STATES RELATIVE TO IONIC POTENTIAL CURVE
 - IONIC STATE PREDISSOCIATION (ArI*, ArBr*)
 - FORMATION VIA METASTABLE REACTIONS

- POSITION OF HIGHER LYING ELECTRONIC LEVELS OF THE MOLECULE
 - LOW SELF ABSORPTION

The reaction rates shown above have been determined for both KrF* formation processes^(72,105,106) and for HgCl* formation^(63,107,108). The reaction branching ratios into the ionic excited state of KrF* are near unity for all of the above formation channels.

- Molecular ground states which are repulsive or characterized by a strong covalent bond avoid rapid bottlenecking during the laser pulse.

The lower state need only be repulsive enough for rapid molecular dissociation and may even be relatively flat as in the case of KrF shown in Figure 44. In fact, a strongly repulsive lower state, such as the Xe₂ ground state, may not be desirable since this could broaden the transition bandwidth and hence decrease the gain.

A strong covalent ground state may be acceptable for candidate molecules having a bound-bound transition. As a rule, covalent bonds exhibit much smaller internuclear equilibrium separations than ionic bonds. As shown in Figure 45 for HgCl, this results in a lower laser level which is a high lying vibrational level. In the case of HgCl, the lower level, $v'' = 22$, has been observed to be rapidly relaxed in high-pressure laser gas mixtures during laser pulses of 100 nsec. If the well depth is adequately large the manifold of lower state vibrational levels can be large enough to maintain a negligible population in the lower laser level even in the presence of rapid relaxation. In this way, bottlenecking of a bound lower laser level may be avoided for pulses the order of 1 μ sec. This constraint on the lower laser level eliminates the alkaline earth monohalides as scalable laser candidates since the ground state as well as the first excited state are ionic character. For example, in CaCl the internuclear separations for the ground and excited states are identical. In this case, the most intense transition in a high pressure laser medium is $v' = 0 \rightarrow v'' = 0$ and this would incur rapid bottlenecking.

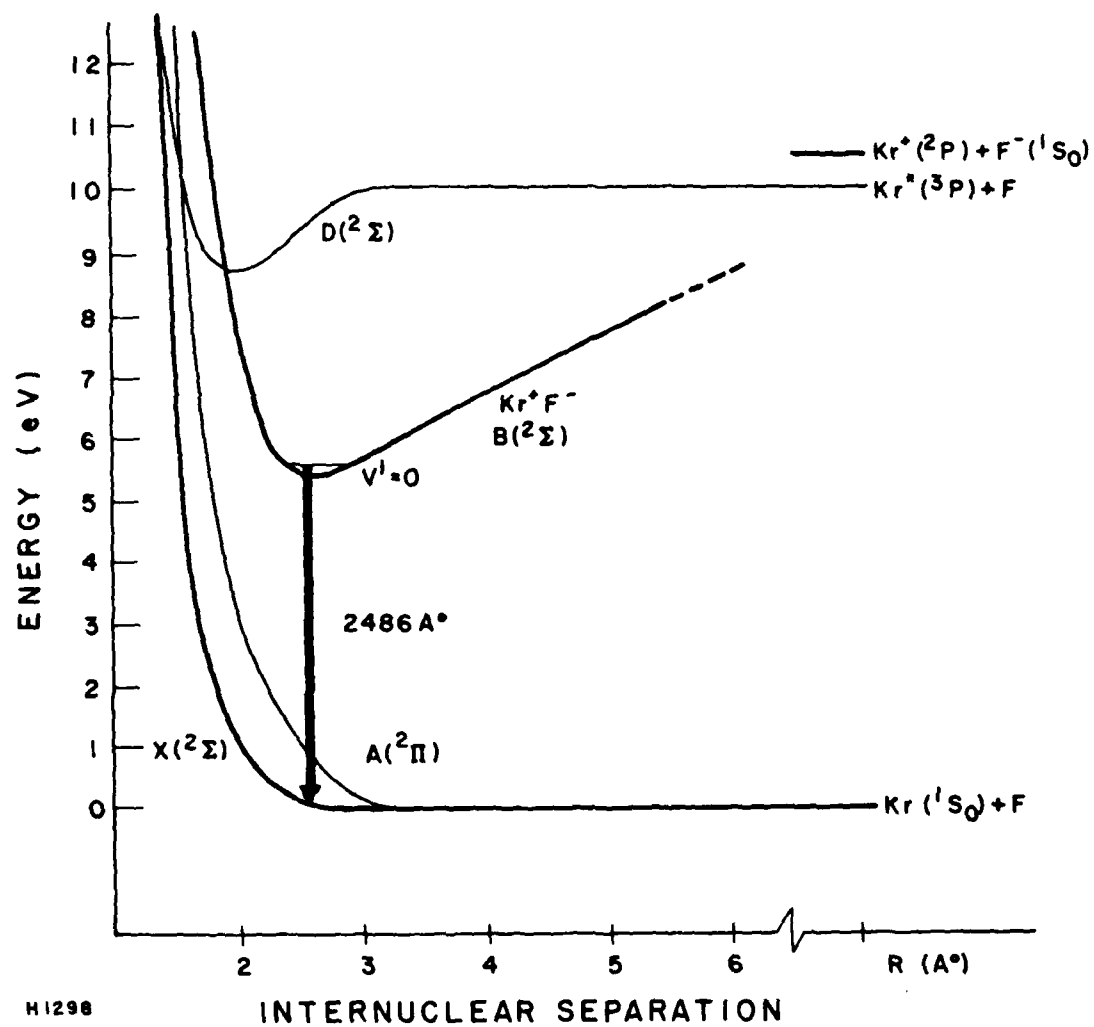


Figure 44. Estimated Potential Curves for KrF

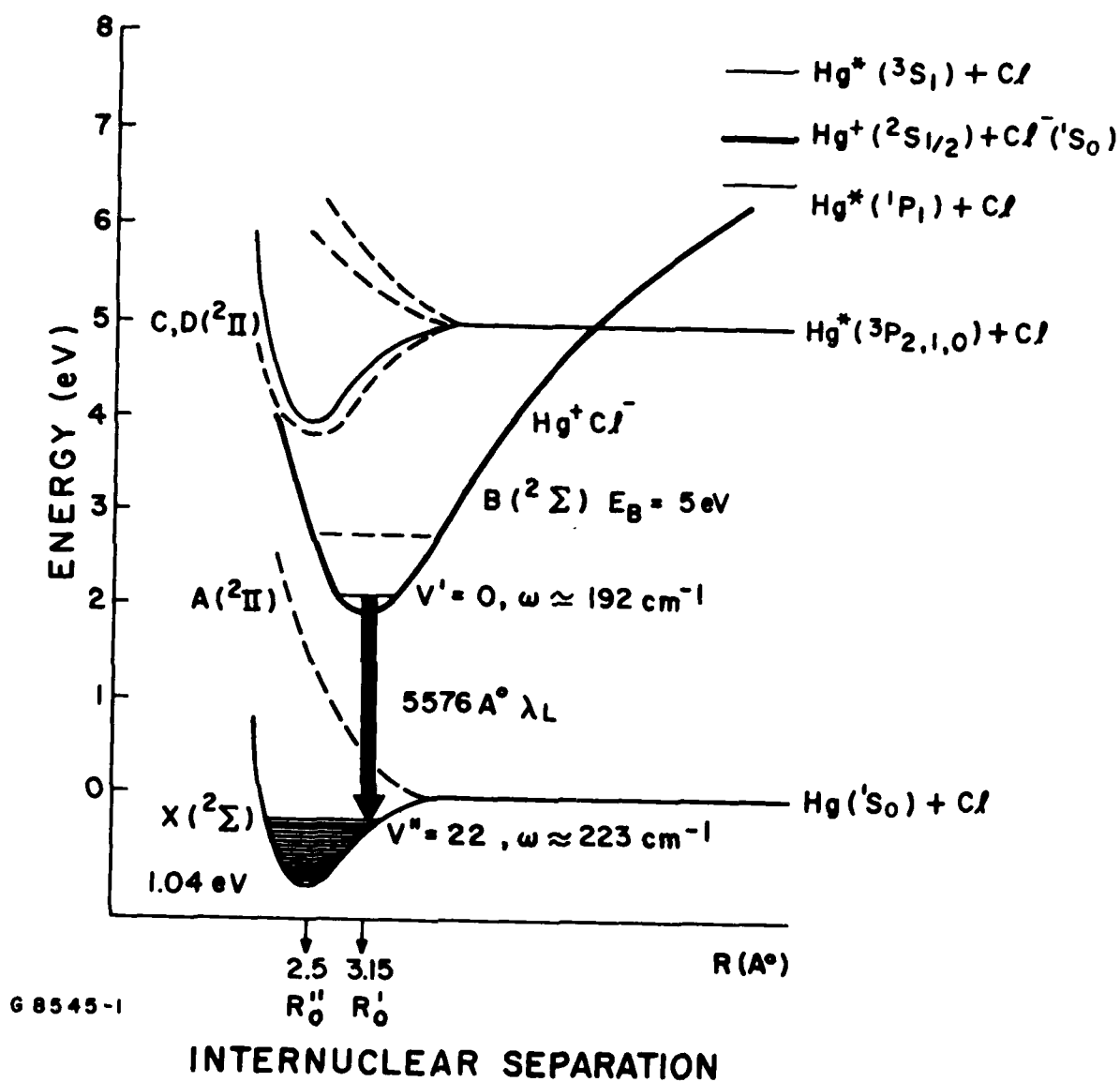
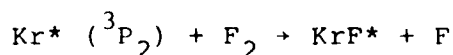


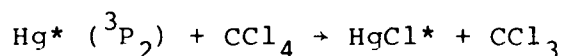
Figure 45. Estimated Potential Curves for HgCl

- The position of molecular states below the ionic excited state is critical to both formation and quenching of this excited state via potential curve crossing.

States whose potential curve cross the ionic potential curve far above the minimum may be useful in the formation of the ionic molecular state via neutral, or harpoon reactions. As shown in Figures 44 and 45, metastable Kr* and Hg* atoms open the respective formation channels:



$$k = 8 \times 10^{-10} \text{ cm}^3/\text{sec}$$



$$k = 2 \times 10^{-10} \text{ cm}^3/\text{sec}$$

It should be cautioned that excited states which cross the ionic potential curve near its minimum can lead to rapid dissociation of the ionic molecule. An example of this is indicated by the potential curves for ArI shown in Figure 46. In fact, ArI* emission is totally quenched by this predissociation and every ArI* simply leads to the creation of an excited iodine atom, I*. A similar situation occurs for ArBr*, resulting in Br* production. In fact this predissociation has been suggested⁽⁵⁴⁾ as the primary formation process for the Br₂* laser.

Clearly, if the ionic curve minimum is far enough above lower molecular states, branching into these lower states can be avoided. This condition can be satisfied in molecules composed of atoms have a ground state configuration which is closed shell, ¹S₀, namely the rare gases, Zn, Cd, and Hg, and the alkaline earths; or atoms with one electron less than a closed shell, the halogens. With the exception of iodine, these atomic species do not contribute states lying several

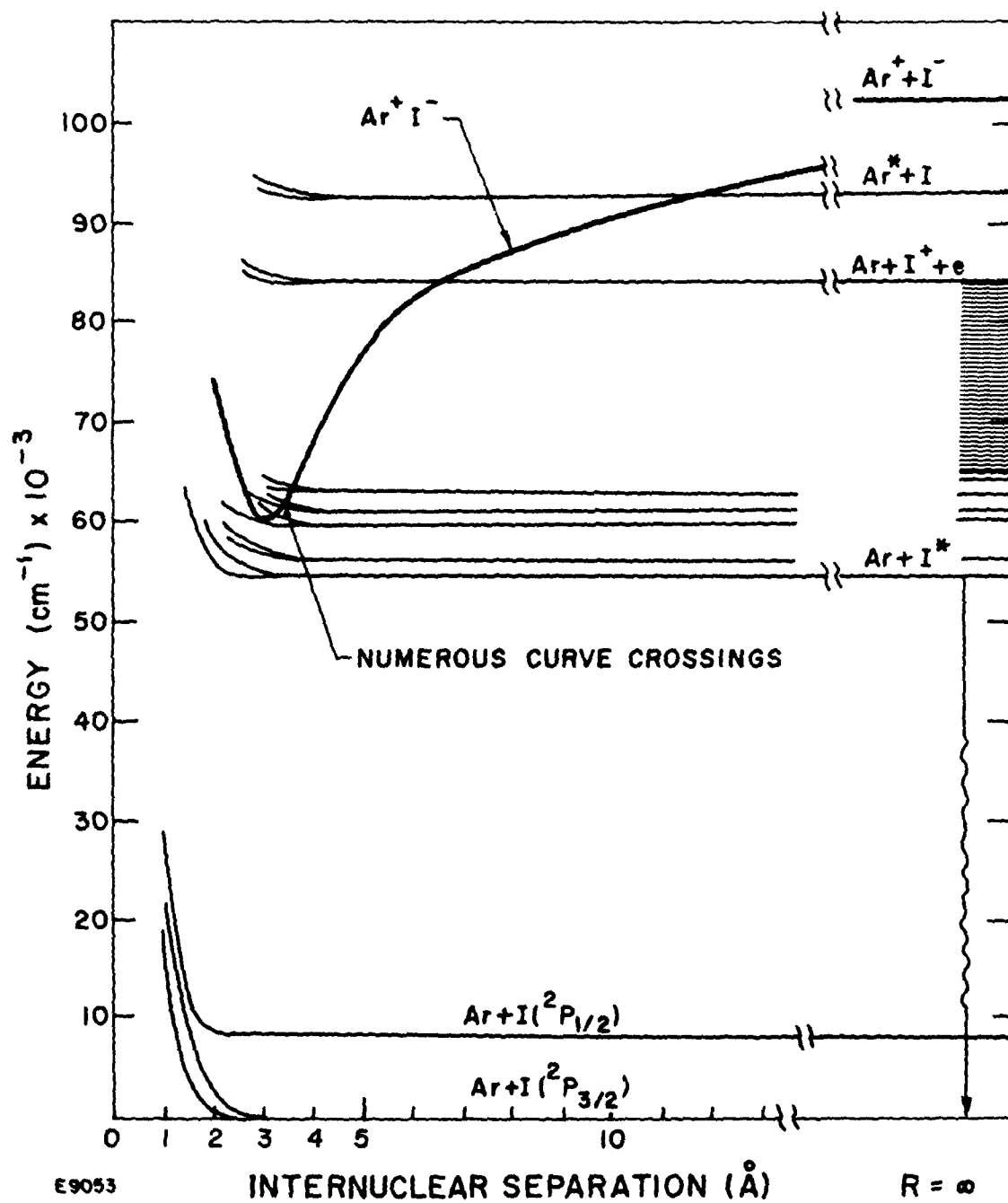
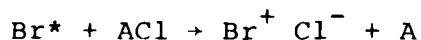


Figure 46. Estimated Potential Curves for ArI

electron volts above the ground states from which lower molecular potentials can be formed. Thus, the excited state ionic molecular curve can extend down to an energy of several eV without crossing many lower molecular curves. Transitions from the lowest vibrational levels of such ionic potentials result in visible and near UV wavelengths. In contrast, $(np)^4$ outer shell electron configurations such as oxygen, selenium and sulfur have 1D and 1S states which lie within 1-3 eV of the ground state. These will lead to molecular potentials which cross the ionic excited state curves and possibly incur predissociation in a species such as ClO .

B. INTERHALOGEN SPECTROSCOPY

The existence of ionic excited states in the homonuclear halogen molecules is well established.⁽⁵²⁾ The halogen lasers Br_2 ,⁽⁹⁾ and I_2 ⁽¹⁰⁾ and F_2 ⁽⁸⁾ have ionic upper levels and are generally consistent with the candidate criteria discussed previously. The larger class of interhalogens should also be considered as laser candidates since the presence of ionic excited states in these molecules provides the possibility of efficient formation, visible laser transitions, and room temperature operation. The similarity of the excited ionic states of the interhalogens to the ground state alkali halides derives from the fact that an excited halogen atom has a tightly bound core similar to that of the neighboring ground state alkali atom. For example, the electron configuration of excited $\text{Br}^*:(4p)^4 5s$ and ground state $\text{Rb}:(4p)^6 5s$ both include a core of tightly bound 4p electrons and a loosely bound 5s valence electron. The ionization potential of the 5s electron, 3.98 eV for Br^* and 4.18 eV for Rb, are quite close as well as the second ionization potential of a 4p electron, 27.5 eV for Rb and 19.2 eV for Br^* . This will result in a chemistry which is kinetically and generically similar for Br^* and Rb. One consequence of this is the ability to form an excited ionic state via the neutral or harpoon reaction:



which occurs via the $\text{Br}^* + \text{Cl}$ curve crossing with the $\text{Br}^+ + \text{Cl}^-$ potential curve. This crossing is ensured since the $\text{Br}^*(^4p_{5/2})$ metastable energy of 7.86 eV is below the asymptote of the lowest ionic curve for $\text{Br}^+(^3p_2) + \text{Cl}^-(^1s_0)$ at 8.23 eV.

The interhalogen ground electronic state $^1\Sigma^+$ has been well characterized as shown in Table 15. There is much less information about the low lying excited molecular $^3\Pi_{0,1,2}$ states resulting from combination of halogen atoms in the ground spin-orbit states $^3p_{1/2}$ and $^3p_{3/2}$. Figures 47, 48 and 49

TABLE 15. INTERHALOGEN GROUND STATE 1_{Σ}^{+} PARAMETERS

	R_0'' (\AA)	ω'' (cm^{-1})	D_0'' (ev)	References
BrCl	2.14	443	2.25	(26)
ICl	2.33	382	2.19	(27)
IBr	2.49	267	1.84	(28)
FCI	1.63	784	2.59	(29)
FBr	1.76	673	2.42	(26)
FI	1.91	612	2.91	(26)

R_0'' : equilibrium internuclear separation

ω'' : vibrational level separation

D_0'' : dissociation energy

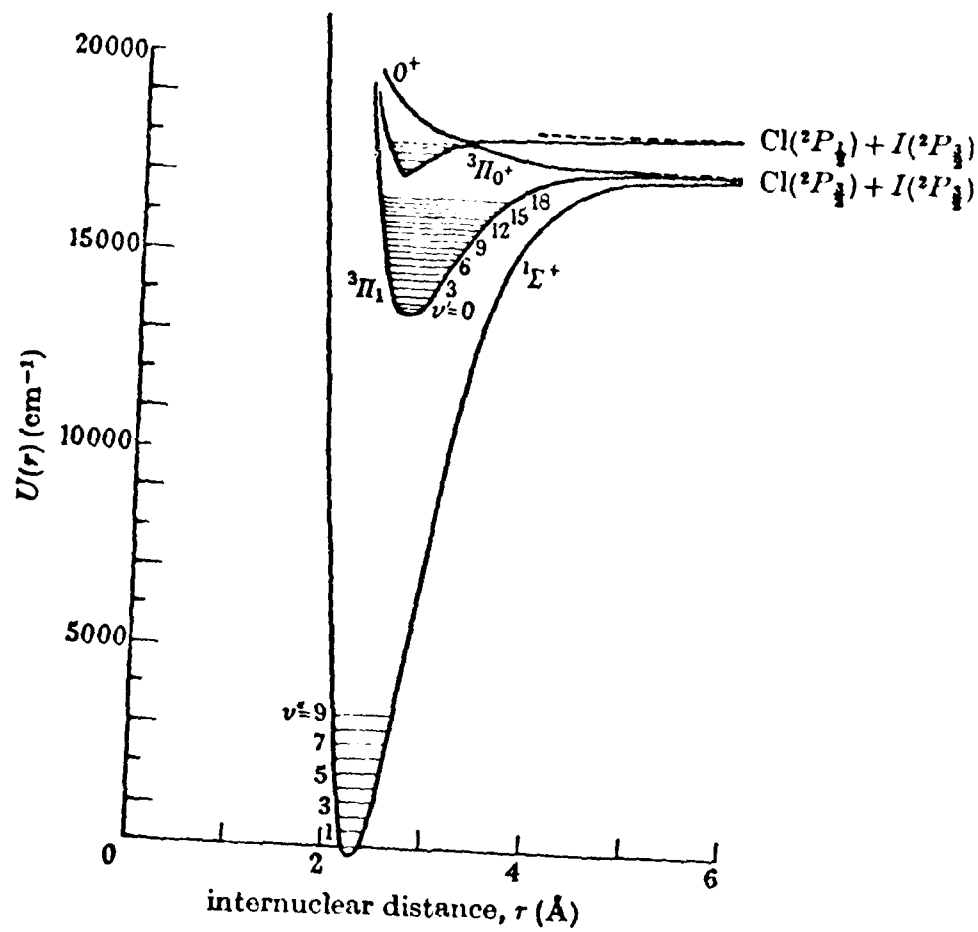


Figure 47. Morse Potential Energy Functions for ICl

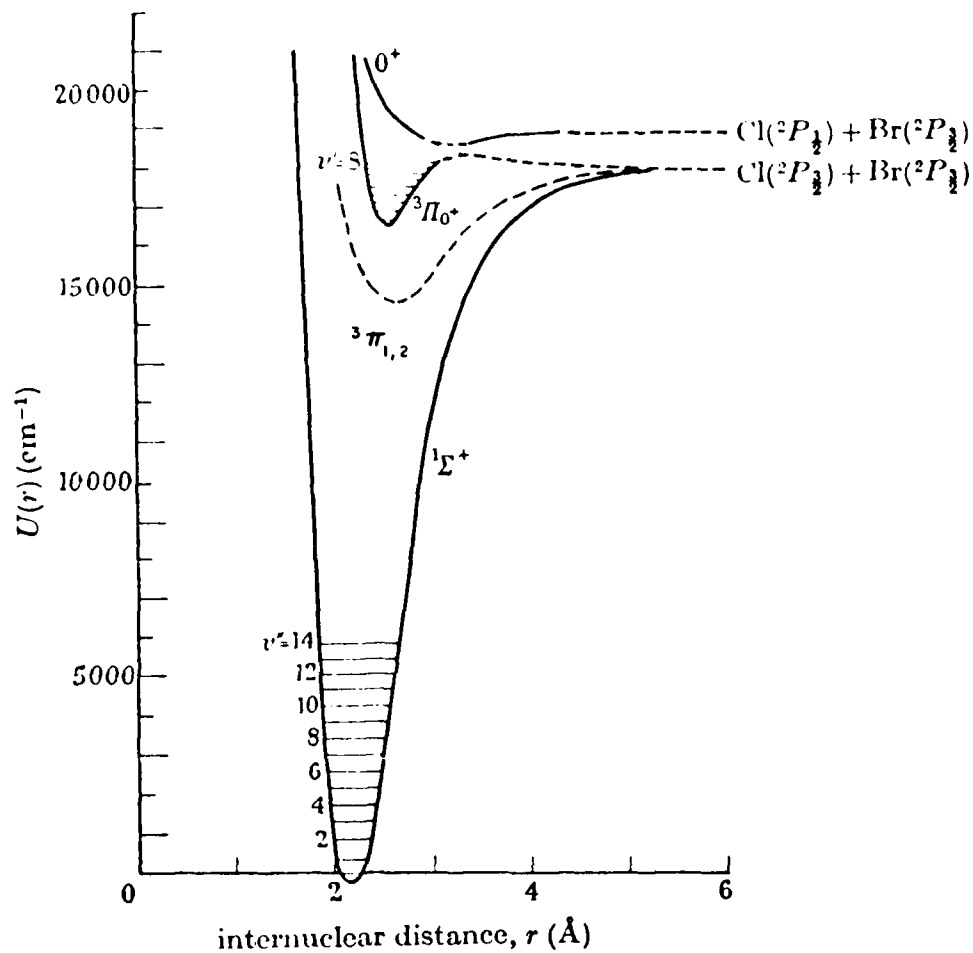


Figure 48. Morse Potential Energy Functions for BrCl (Broken Lines Indicate the Estimated Positions of Unobserved States.)

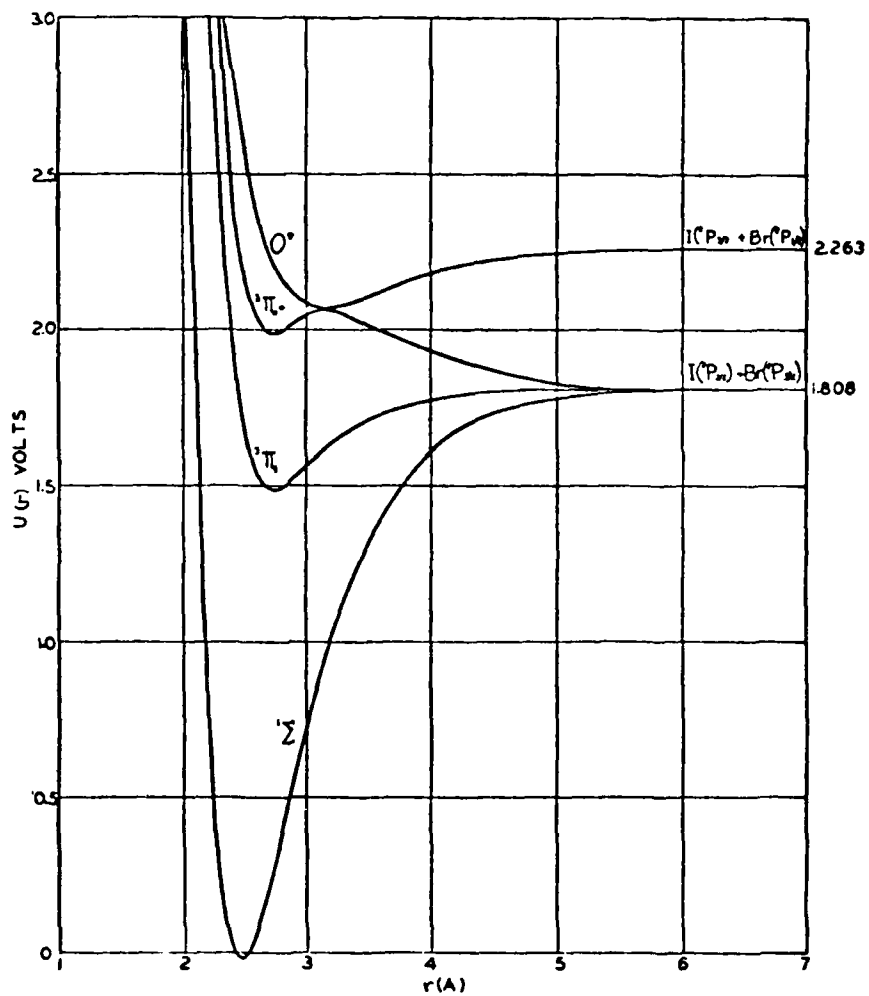


Figure 49. Approximate Potential Energy Curves for IBr

show these lower excited molecular states for I Cl, ⁽¹⁰⁹⁾ Br Cl ⁽¹⁰⁹⁾ and I Br. ⁽¹¹⁰⁾ The excited ion-pair states of these molecules has not been considered previously.

The following analysis predicts the features of the interhalogen ion-pair excited states and the wavelengths of expected laser transitions. It is assumed for these purposes that the lowest ion-pair states correlating with the lowest halogen positive ion states $X^+ (^3P_{2,1,0})$ have the same shape and are separated at the potential minima by the $^3P_{2,1,0}$ level separations.

The excited state ion-pair potential curve for interhalogen diatomics has been approximated by a truncated Rittner potential ⁽¹¹¹⁾ with a repulsive term of the Born-Mayer form. ⁽¹¹²⁾ This approximation includes the ion-ion polarization terms which are important for the interhalogen $X^+ Y^-$ pairs due to the sizeable positive ion polarizability. These polarizabilities for halogen atoms can be estimated from the negative ion polarizabilities by methods discussed elsewhere. ⁽¹¹³⁾ A comparison of these polarizabilities in Table 16 shows the halogen positive ion polarizabilities are a factor of ~ 2 greater than those of the corresponding alkali atoms. ⁽¹¹¹⁾ As an example, the polarization terms contribute $\sim 16\%$ to the calculation of the ion-pair binding energy for $Cl^+ F^-$.

Table 17 lists the results of these calculations and compares the interhalogen ion-pair state features to those of the alkali halides. ⁽¹¹¹⁾ In general, note that the interhalogen equilibrium separation is small and the binding energy is greater than the corresponding alkali halide. This is a result of the stronger ion-ion polarization interaction between halogen ion pairs.

To estimate the interhalogen wavelengths expected to exhibit strong lasing transitions, assumptions concerning the lower levels are necessary. Analogous to the identification ⁽⁴⁸⁾ of the lasing transitions in I_2 and Br_2 , it will be assumed that the strong interhalogen transitions will also occur between $^3\pi_2 \rightarrow ^3\pi_2$ molecular states. As shown in Section III, the I_2

TABLE 16. HALOGEN POLARIZABILITIES

	$\alpha_{-}(\text{\AA}^{\circ})^3$	$\alpha_{+}(\text{\AA}^{\circ})^3$		$\alpha_{+}(\text{\AA}^{\circ})^3$
F^{-}	1.28	.456	Na^{+}	.18
Cl^{-}	3.00	1.51	K^{+}	.84
Br^{-}	4.50	2.56	Rb^{+}	1.42
I^{-}	7.00	4.05	Cs^{+}	2.44

TABLE 17. INTERHALOGEN IONIC STATE COMPARISON

INTERHALOGEN			ALKALI HALIDE		
	$R_e (A^\circ)^{(a)}$	$E_B (ev)^{(b)}$		$R_e (A^\circ)$	$E_B (ev)$
FCl	2.13	6.52	NaCl	2.36	5.75
FBr	2.34	6.09	NaBr	2.50	5.54
FI	2.40	6.22	NaI	2.71	5.22
Cl F	2.16	6.32	KF	2.17	6.04
Cl Br	2.55	5.63	KBr	2.82	4.93
Cl I	2.63	5.69	KI	3.05	4.60
BrF	2.38	5.86	RbF	2.27	5.79
BrCl	2.56	5.56	RbCl	2.79	4.92
BrI	2.87	5.18	RbI	3.18	4.42
IF	2.46	5.82	C _s F	2.35	5.66
ICl	2.66	5.50	C _s Cl	2.91	4.87
IBr	2.89	5.08	C _s Br	3.07	4.71

(a) R_e is the equilibrium internuclear separation

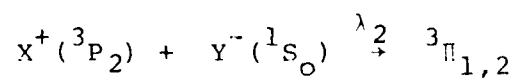
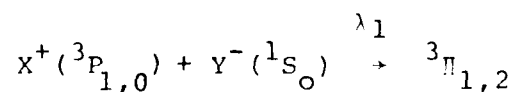
(b) E_B is the ion-pair binding energy

lower laser level $^3\pi_2$ is a low lying excited state nested within the ground electronic state manifold. The low lying excited states shown in Figures 47-49 indicate similar nested states for the interhalogens. It will be assumed that the $^3\pi_1$ and $^3\pi_2$ curves are as close for interhalogens as they are⁽²³⁾ for I_2 ($\sim .1$ eV) and this difference will be neglected here.

Table 18 lists the predicted laser wavelengths for the interhalogen molecules. The wavelengths have been indicated for transitions originating from the two lowest ion-pair states which correlate with the separate atoms $X^+(^3P_2) + Y^-(^1S_0)$ and $X^+(^3P_{1,0}) + Y^-(^1S_0)$. Also listed are the strongest fluorescence bandheads observed in our e-beam pumping experiments and also the demonstrated laser transitions.^(14,15) The largest variation is $\leq 10\%$ and results from the uncertainty in estimating the lower state of the transition. In these calculations the lower energy level is taken to be the $^3\pi_2$ potential minimum. The observed transitions appear to be originating on the higher ion-pair state. This is consistent with possible formation channels and will be discussed below in the kinetics section. Figure 50 shows an estimated potential curve for $I\ Cl$ based upon the analysis of this section. Figures 51 and 52 show microdensitometer traces of $I\ Cl^*$ and $Br\ Cl^*$ spectra for different gas mixture compositions. Note that the strong interhalogen bands overlap the weaker Br_2^* and I_2^* bands. Fluorescence data was also obtained for $I\ Br^*$ and BrF^* .

TABLE 18. COMPARISON OF PREDICTED/OBSERVED
INTERHALOGEN SPECTRA

● ESTIMATE TRANSITION BAND WAVELENGTHS



X^+Y^-	λ_1 (nm)	λ_2 (nm)	λ_{OBS} (nm)
IF	480	700	491 ⁽¹⁵⁾
ICl	450	670	430
IBr	380	510	390
BrF	350	400	355
BrCl	340	370	315
BrI	270	300	---
ClF	310	320	284 ⁽¹⁴⁾
ClBr	260	270	---
ClI	250	260	---
FCI	160		---
FBr	150		---
FI	140		

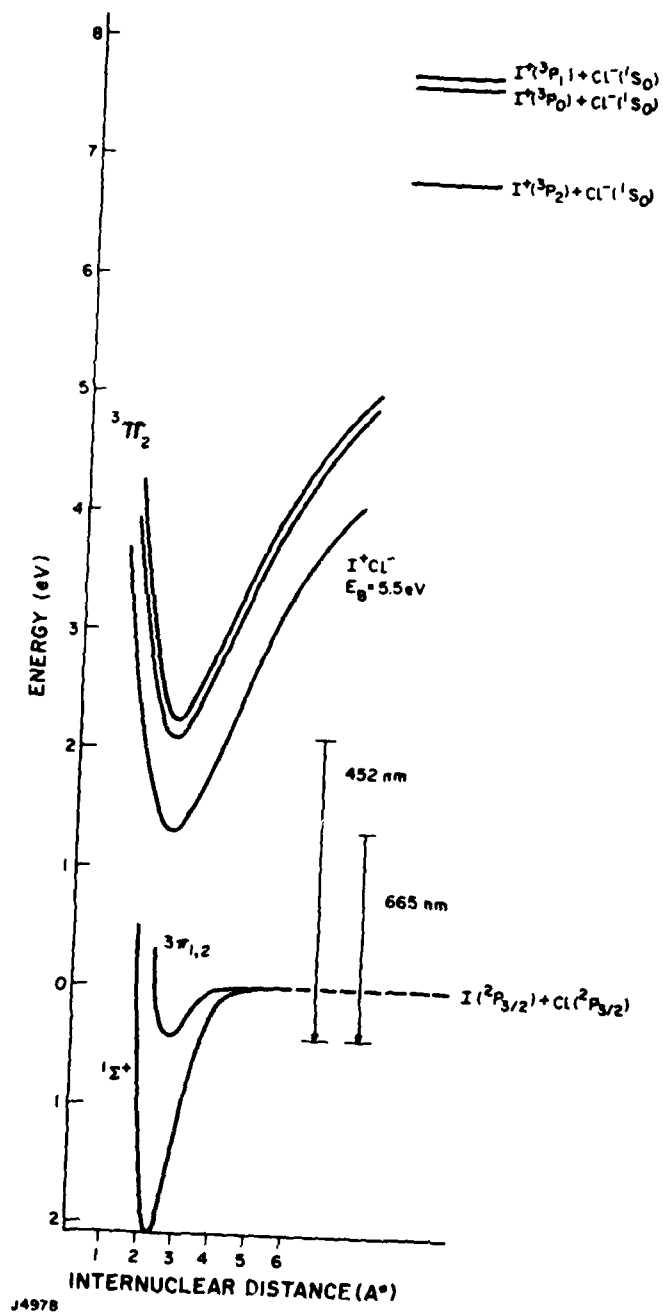


Figure 50 Estimated Potential Curves for ICl

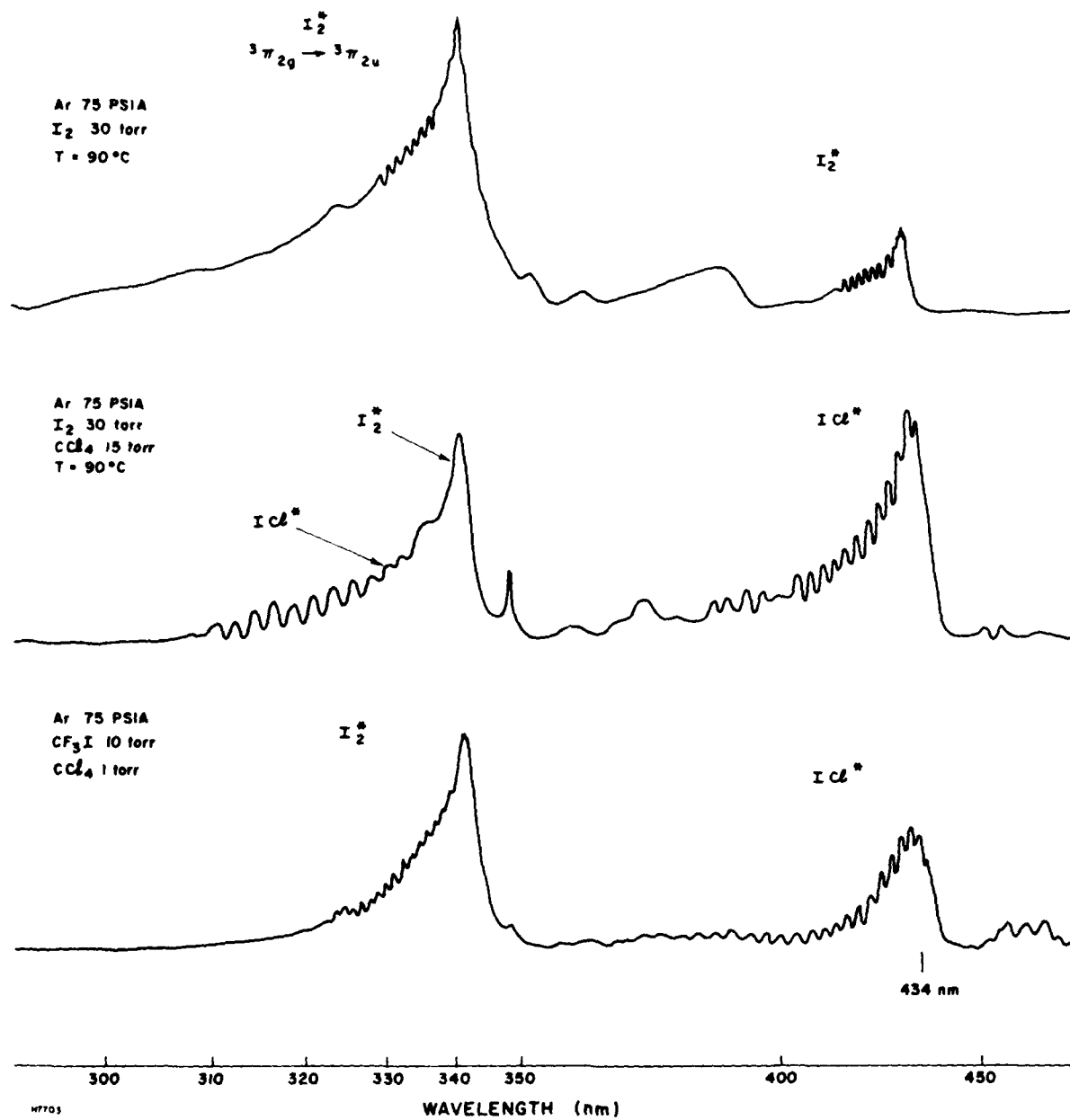


Figure 51. E-Beam Excited ICl^* Fluorescence

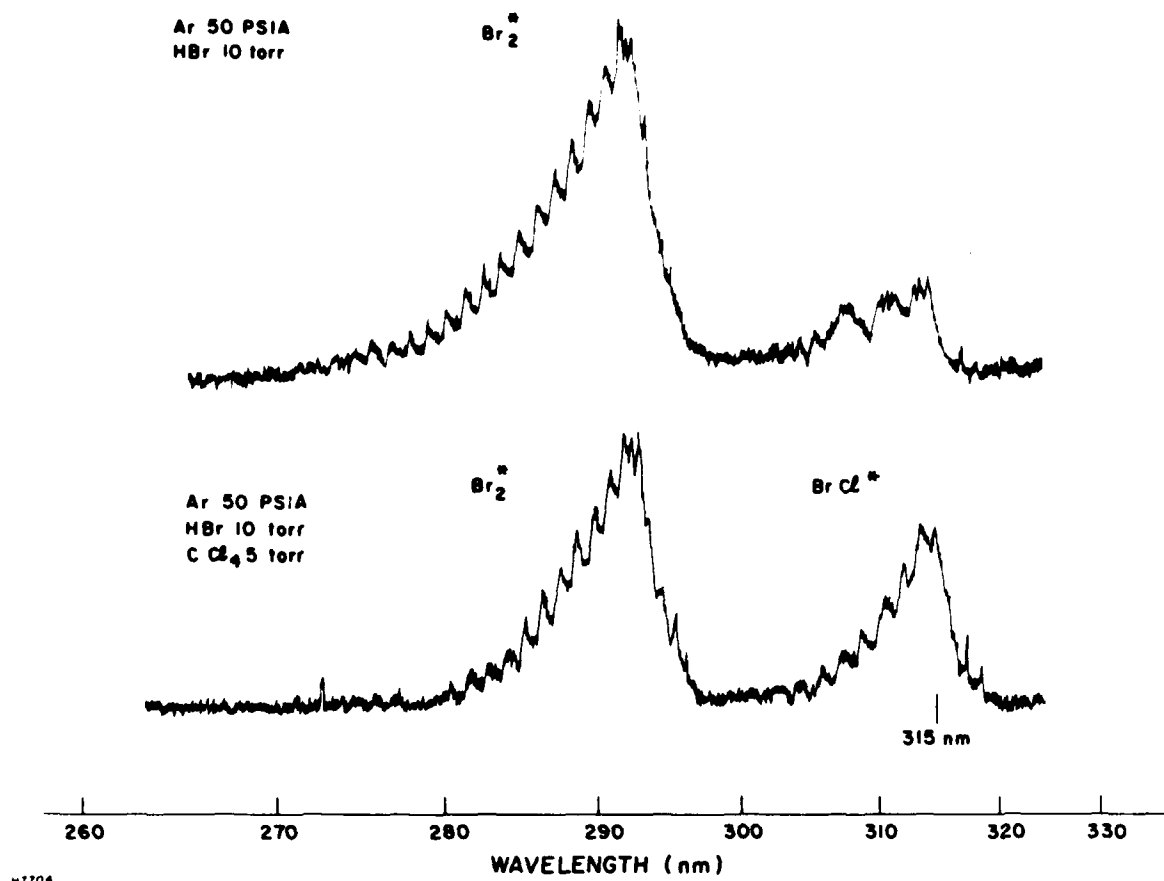


Figure 52. E-Beam Excited BrCl^* Fluorescence

C. INTERHALOGEN KINETICS

Two possible formation channels into the ionic state may be used to advantage in direct e-beam pumping of high pressure gas mixtures. These formation processes leading to the interhalogen excited ion-pair species $XY^* = X^+ Y^-$ include ion-ion recombination

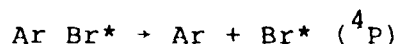


and the neutral reaction

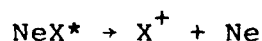
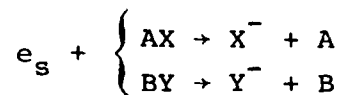
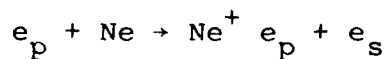


1. Ion Formation Channel

The ion pathways may be accessed through the predissociation of neon halide species into halide positive ions. It is well established⁽⁵⁴⁾ that $Ar^+ Br^-$ predissociates



into the manifold of bromine 4P states. Similar processes occur for $Ar Cl^*$, $Ar I^*$ and $Ne F^*$ to yield Cl^* , I^* and F^* . This predissociation follows from the curve crossings shown in Figure 53 which occurs at the minimum of the $Ar I^*$ potential curve. Similar predissociation is predictable for the neon halides $Ne Br^*$, $Ne Cl^*$ and $Ne I^*$. However, in this case, the predissociation should yield Br^+ , Cl^+ and I^+ as indicated in Figure 54. The predicted interhalogen formation kinetics for $Ne/AX/BY$ mixtures of high pressure Ne and halogen bearing molecules AX , BY is characterized by the example



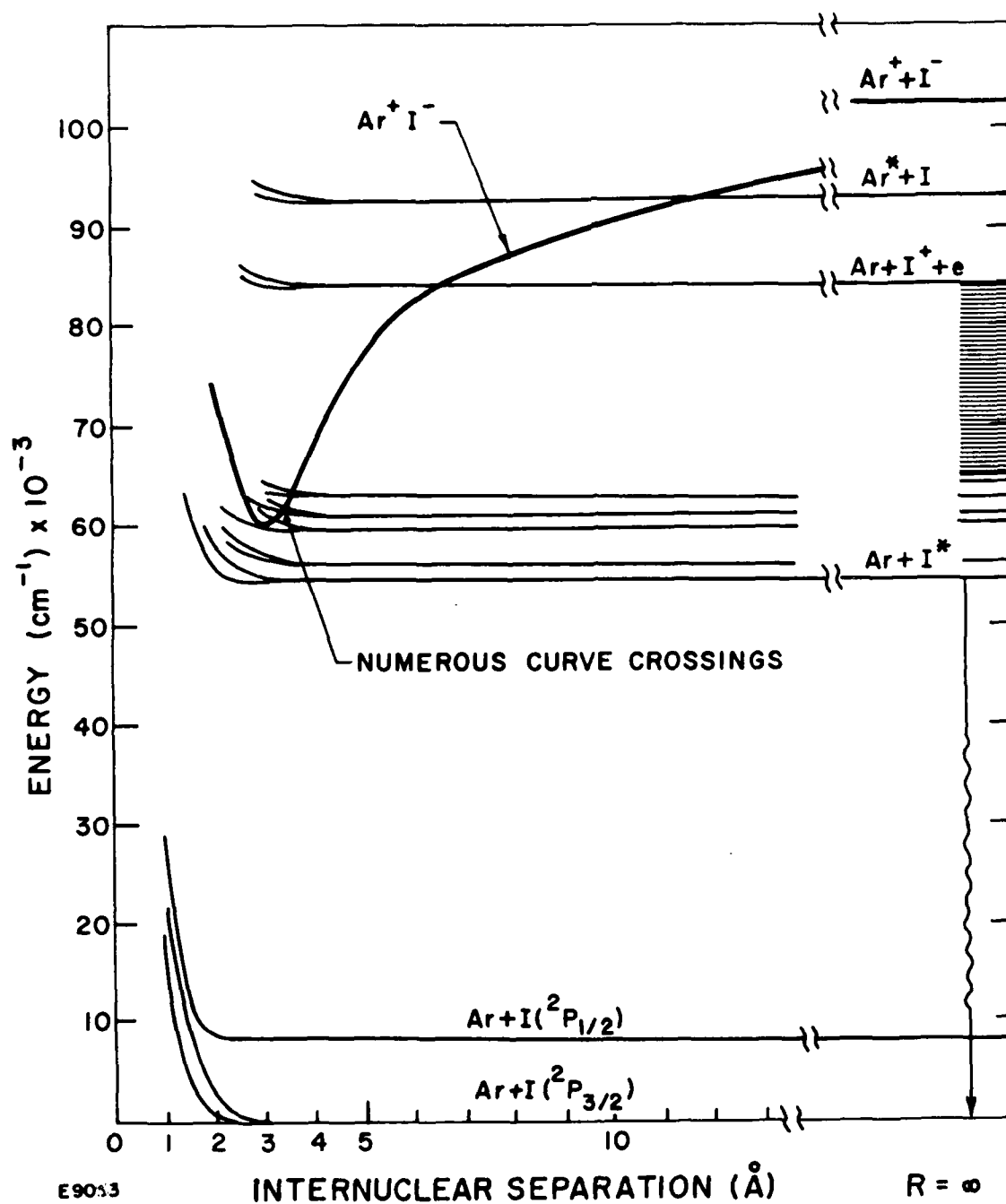
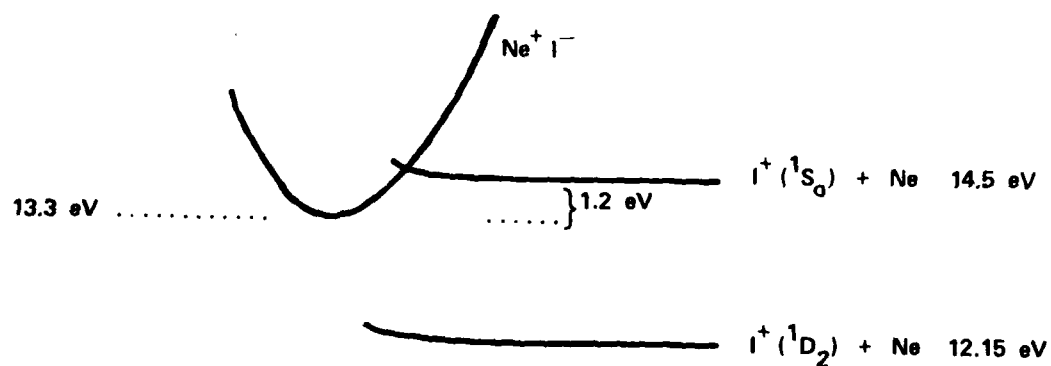
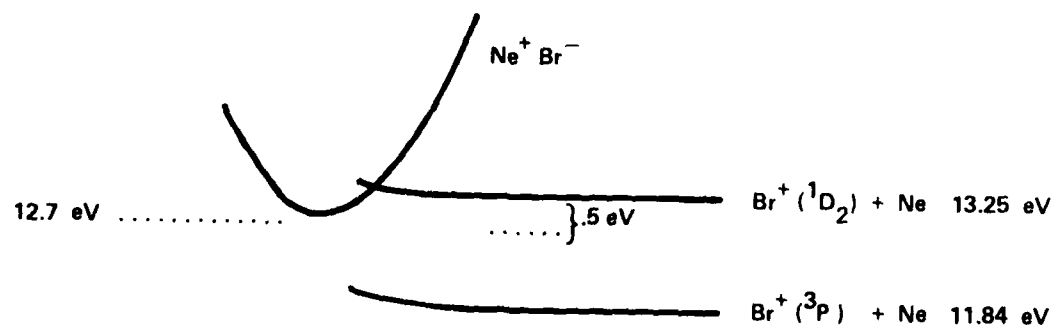
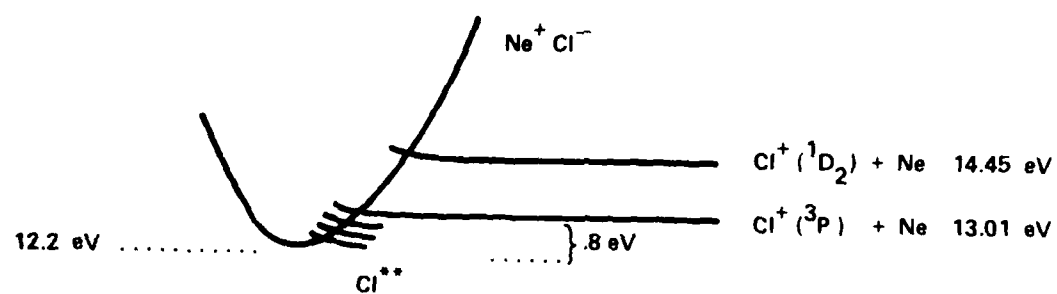


Figure 53. Estimated Potential Curves for ArI



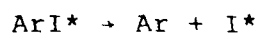
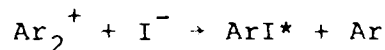
J 4977

Figure 54. Predicted Neon Halide Predissociation

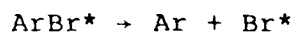
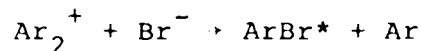
Many pathways have been ignored in this simple example, however, such a scheme can describe the recent ClF* laser demonstration⁽¹⁴⁾ in Ne/F₂/Cl₂.

2. Neutral Formation Channel

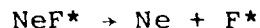
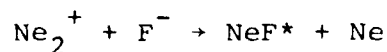
In general, the neutral reaction channel is not easily accessed in direct e-beam excitation. However, as mentioned above, mixtures excited halogen atoms may readily be formed in rare gas/halogen mixtures by



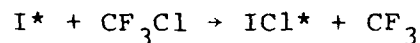
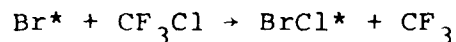
as indicated in Figure 46, and also by



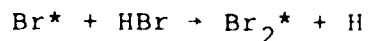
and



In this case, the formation of an ionic state via the neutral reactions



become accessible. Analogous neutral reactions have been identified⁽⁵⁴⁾ as the formation channels for Br₂* excited states in Ar/Br₂ and Ar/BrI mixtures. The interhalogen formation channels indicated above should be comparable to those processes observed in Ref. 54. These neutral kinetics rely on finding the optimum halogen donors and mixture composition such that dissociative electron attachment forms primarily I⁻ and Br⁻. It is also important to recognize that competing neutral reactions will be present such as

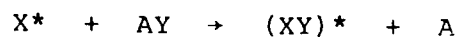


Examples of candidate molecules and gas mixture components favorable for formation via natural reactions are shown in Table 19.

The experimental results shown above in Section II.B are consistent with the neutral formation channels indicated in Tables 20 and 21. Particularly in the case of ICl^* formation, the emission appears to be originating on the ionic potential curve correlating with $\text{I}^+(^3\text{P}_0) + \text{Cl}^-(^1\text{S}_0)$ which is the second ion-pair state. The excited I^* levels produced in the predissociation of ArI^* have energies $^4\text{P}_{5/2}$ (6.77 eV), $^4\text{P}_{3/2}$ (7.66 eV), $^4\text{P}_{1/2}$ (7.55 eV). The details of the dynamics depend on the ^4P branching ratios but it is evident that selective excitation of the $\text{I}^+(^3\text{P}_0)$ ion state is possible and also is consistent with the shorter wavelengths predicted by the ionic state model.

TABLE 19. GAS MIXTURES FOR INTERHALOGEN
FORMATION VIA NEUTRAL CHANNELS

- FORMATION OF $(XY)^* = (X^+Y^-)$



<u>IONIC STATE</u>	<u>GAS MIXTURE</u>
I^+Cl^-	Ar/HI/CF ₃ Cl
I^+F^-	Ar/HI/CF ₄
I^+Br^-	Ar/HI/HBr
Br^+Cl^-	Ar/HBr/CF ₃ Cl
Br^+F^-	Ar/HBr/CF ₄
Br^+I^-	Ar/HBr/CF ₃ I
F^+Cl^-	Ne/F ₂ /CF ₃ Cl
F^+Br^-	Ne/F ₂ /CF ₃ Br
F^+I^-	Ne/F ₂ /CF ₃ I

TABLE 20. NEUTRAL FORMATION CHANNEL CONSISTENT
WITH BrF*, BrCl* FLUORESCENCE RESULTS

Ar/HBr/CCl₄, NF₃ : 50 PSIA/10t/2t

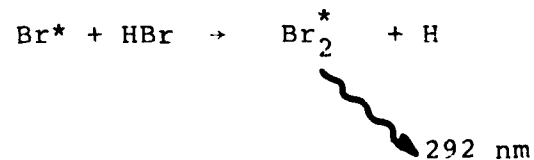
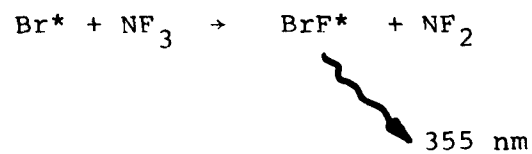
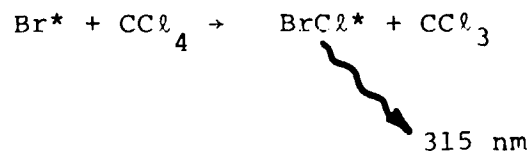
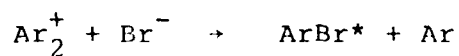
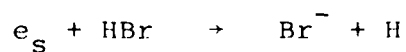
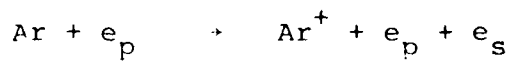
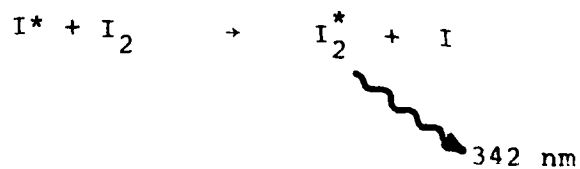
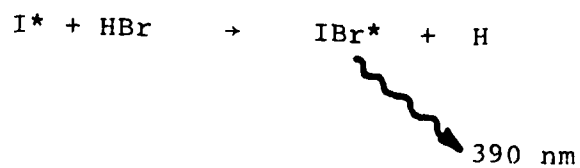
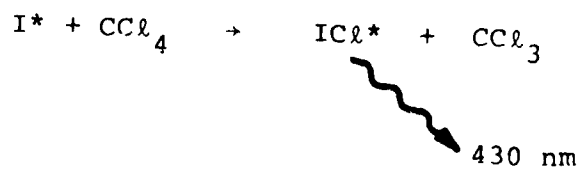
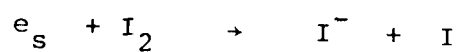
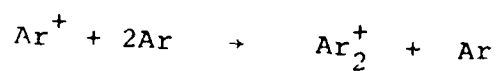
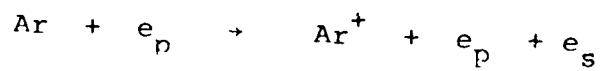


TABLE 21. NEUTRAL FORMATION CHANNEL
CONSISTENT WITH ICl*/IBr* FLUORESCENCE RESULTS

Ar/I₂/CCl₄, HBr : 50 PSIA/30t/10t



REFERENCES

1. Hoffman, J.M., Hays, A.K. and Tisone, G.C., Appl. Phys. Lett. 28, 538 (1976).
2. Murray, J.R. and Powell, H.T., Appl. Phys. Lett. 29, 252 (1976).
3. Searles, S., private communication.
4. Ewing, J.J. and Brau, C.A., Appl. Phys. Lett. 27, 350 (1975).
5. Searles, S.K. and Hart, G.A., Appl. Phys. Lett. 27, 243 (1975).
6. Brau, C.A. and Ewing, Appl. Phys. Lett. 27, 435 (1975).
7. Hill, R.M., paper TUA5, Excimer Lasers, Sept 11-13, 1979, Charleston, S.C.
8. Rice, J.K., Hays, A.K., Woodworth, JR., Appl. Phys. Lett. 31 31 (1977).
9. Murray, J.R., Swingle, J.C., and Turner, C.E., Appl. Phys. Lett. 27, 557 (1975).
10. Ewing, J.J. and Brau, C.A., Appl. Phys. Lett. 27, 557 (1975).
11. Burnham, R. Appl. Phys. Lett 33, 156 (1978).
12. Parks, J.H., Appl. Phys. Lett. 31, 297 (1977).
13. Parks, J.H., Appl. Phys. Lett. 31, 192 (1977).
14. Diegelmann, M. and Hokla, K., Kompa, K.L., Opt. Commun. 29, 334 (1979).
15. Diegelmann, M., Grieneisen, and Hokla, Kompa, K.L., Karsinsiki, J., Laser Focus p. 52, March 1980.
16. Burnham, R., Harris, N.W. and Djeu, N., Appl. Phys. Lett. 28, 86 (1976).
17. Ewing, J.J. and Brau, C.A., Phys. Rev. A12, 129 (1975).
18. Brau, C.A. and Ewing, J.J., J. Chem. Phys. 63, 4640 (1975).

19. Mangano, J.A. and Jacob, J.H., Appl. Phys. Lett. 27, 495 (1975).
20. Jacob, J.H. and Mangano, J.A., Appl. Phys. 28, 724 (1976).
21. Daugherty, J.D., Mangano, J.A., Jacob, J.H., Appl. Phys. Lett. 28, 581 (1976).
22. Brau, C.A. and Ewing, J.J., "Rare Gas Monohalide Lasers: Performance and Spectroscopy," Second Summer Colloquium on Electronic Transition Lasers, Woods Hole, Massachusetts, Sept. 1975).
23. Hsia, J.C., Mangano, J.A., Jacob, J.H., Rokni, M. Appl. Phys. Lett. 34, 208 (1979).
24. Hsia, J.C., Mangano, J.A., Jacob, J.H., Rokni, M., "Interim Report - One Meter KrF* Laser," Semi Annu. Tech. Rep., August 1976 - February 1977.
25. Ewing, J.J., Jacob, J.H., Mangano, J.A., and Brown, H., Appl. Phys. Lett. June 1976.
26. King, D.L. and Setser, D.W., "Quenching Studies of Ar ($3p0$, $3p2$) Metastable Atoms by Chlorine Atoms," presented at 4th Conference on Chemical and Molecular Lasers, St. Louis, MD (October 21-23, 1974).
27. Golde, M.F. and Thrush, B.A., Chem. Phys. Lett. 29, 486 (1974).
28. Velazco, J.E. and Setser, D.W., J. Chem. Phys. 62, 1990 (1975).
29. Bartlett, N. and Sladky, F.U., "The Chemistry of Krypton, Xenon and Radon," in Comprehensive Inorganic Chemistry, Vol. I, A.F. Trotman-Dickenson, executive-ed. (Pergamon Press, Oxford, 1973).
30. Millikan, R.C. White, D.R., J. Chem. Phys. 39, 3209 (1963).
31. Golde, M.F. and Thrush, B.A., Chem. Phys. Lett. 29, 486 (1974).
32. Golde, M.F., J. Mol. Spectry 58, 261 (1975).
33. Dunning, T.H., Jr. and Hay, P.J., Los Alamos Scientific Laboratory Report LA-UR-76-411, and J. Chem. Phys. 66, 1306 (1977).
34. Tellinghuisen, J., Hoffman, J.M., Tisone, G.C., and Hays, A.K., J. Chem. Phys. 64, 2484 (1976).

35. Gordon, R.G., Harvard University, private communication.
36. Tellinghuisen, J., Vanderbilt University, private communication.
37. Lee, Y.T., (U.C. Berkely), private communication.
38. See Ref. 18 for a complete discussion.
39. Krauss, M., National Bureau of Standards, private communication.
40. Searles, S.K. and Hart, G.A., Appl. Phys. Lett. 27, 243 (1975).
41. Davidovits, P. and Broadhead, D.C., J. Chem. Phys. 46, 2968 (1967).
42. Canguli, P.S. and Kaufman, M. Chem. Phys. Lett. 25, 221 (1974).
43. For a discussion of the alkali/halogen reactions see for example Kieth J. Laidler, "Theories of Chemical Reaction Rates," McGraw Hill Book Co., New York (1969).
44. Krenos, J.R. and Tully, J.C., J. Chem. Phys. 62, 420 (1975).
45. Gundel, L.A., Setser, D.W., Clyne, M.A.A., Coson, J.A., and Nip, W. "Rate Constants for Specific Product Channels from Ar($^3P_{2,0}$) Reactions and Spectrometer Calibration in the Vacuum Ultraviolet," J. Chem. Phys. 64, 4390 (1976).
46. Velazco, J.E. and Setser, D.W., Chem. Phys. Lett. 25, 197 (1974).
47. Piper, L.G., Velazco, J.E. and Setser, D.W., J. Chem. Phys. 59, 333 (1973).
48. Tellinghuisen, J., Chem. Phys. Lett. 49, 485 (1977).
49. Wilkerson, A.K. and Tisone, Thirtieth Symposium on Molecular Structure and Spectroscopy, Columbus, Ohio, 1975m Paper No. TH10 (unpublished).
50. McCusker, M.V., Hill, R.M., Huestis, D.L., Lorenes, D.C., Gutchek, R.A., and Nakano, H.H., Appl. Phys. Lett. 27, 363 (1975).
51. Tellinghuisen, J. Chem. Phys. Lett. 29, 359 (1974).

52. Mulliken, R.S., J. Chem. Phys. 55, 288 (1971).
53. Venkateswarlu, P., Phys. Rev. 81, 821 (1951).
54. Kolts, J.H., Setser, D.W., J. Appl. Phys. 48, 409 (1977).
55. Elliott, A., Proc. R. Soc. (Lond.) A174, 273 (1940).
56. Wadt, W.R., Cartwright, D.C., Cohen, J.S., Appl. Phys. Lett. 31, 672 (1977).
57. Champagne, L.F., Harris, N.W., Appl. Phys. Lett. 31, 513 (1977).
58. Rokni, M., Jacob, J.H., Mangano, J.A., Appl. Phys. Lett. 32, 622 (1978).
59. Rokni, M., Jacob, J.H., Mangano, J.A., Brochu, R., Appl. Phys. Lett. 32, 223 (1978).
60. Yavorsky, B., Bull. Acad. Sci. U.S.S.R. 9, 233 (1945).
61. Kenty, C., J. Appl. Phys. 21, 1309 (1950).
62. Document, B. and Phipps, M.K., J. Chem. Phys. 22, 110 (1954).
63. Krause, H.F., Johnson, S.G., Datz, S. and Schmidt-Bleek, F.K., Chem. Phys. Lett. 31, 577 (1975).
64. Wodarczyk, F.J., Harlser, A.B., Chem Phys. Lett. 62, 529 (1979).
65. Medhekar, A.K., Rokni, M., Trainor, D.W., Jacob, J.H., Chem. Phys. Lett. 65, 600 (1979).
66. Mandl, A., Parks, J.H., Roxlo, C., J. Chem. Phys. 72, 504 (1980).
67. Smith, D., Dean, A.G., and Plumb, I.C., J. Phys. B5, 2134 (1972).
68. Biondi, M.A., Mercury Halide Kinetics Review, Univ. So. Calif. March 1, 1979.
69. Bohme, D.K., Adams, N.G., Moselman, M., Dunkin, D.B., and Ferguson, E.E., J. Chem. Phys. 52, 5094 (1970).
70. Christophorou, L.G. and Stockdale, J.A.D., J. Chem. Phys. 48, 1956 (1968). Spence, D. and Schulz, G.J., J. Chem. Phys. 58, 1800 (1973).

71. Flannery, M.R., Chem. Phys. Lett. 56, 143 (1978).
72. Rokni, M., Jacob, J.H., Mangano, J.A., and Borchu, R., Appl. Phys. Lett. 31, 79 (1977).
73. Mangano, J.A., Jacob, J.H., Rokni, M. and Hawryluk, A., Appl. Phys. Lett. 31, 26 (1977).
74. Zamir, E., Huestis, D.L., Lorents, D.C. and Nakano, H.H., in Electronic Transition Lasers II edited by L.E. Wilson, S.N. Sucharó, and J.I. Steinfeld, MIT Press, Cambridge, Massachusetts 1977, p. 69.
75. Gleason, R.E., Bonifield, T.D., Keto, J.W. and Walters, G.K., J. Chem. Phys. 66, 1589 (1977).
76. Gedanken, A. Jortner, J., Rax, B. and Szoki, A., J. Chem. Phys. 57, 3456 (1972).
77. Mangano, J.A. and Jacob, J.H., Appl. Phys. Lett. 27, 495 (1975).
78. Calvert, J.G. and Pitts, J.N., Jr., Photochemistry, (Wiley, New York, 1966), p. 184.
79. Ganas, P.S. and Green, A.E.S., Phys. Rev. A4, 182 (1971).
80. Clementi, E. and Roetti, C., Atomic Data and Nuclear Data Tables 14, 177 (1974).
81. Bates, D.R., Proc. R.Soc. A 188, 350 (1947).
82. Klein, M.M. and Brueckener, K.A., Phys. Rev. 111, 1115 (1958).
83. Dalgarno, A., Adv. Phys. 11, 281 (1962).
84. Teachnour, R.R. and Pack, R.T., Atomic Data 3, 195 (1971).
85. Seaton, M.J., Proc. R. Soc. A 208, 418 (1951).
86. Robinson, E.J., Levine, J. and Bederson, B., Phys. Rev. 146, 95 (1966).
87. Dunning, F.B. and Stebbings, R.F., Phys. Rev. A9, 2378 (1974).
88. Stebbings, R.F., (Rice University), private communication.
89. Mangano, J.A., (AERL), private communication.
90. Hay, P. and Dunning, T., Jr., J. Chem. Phys. 66, 1306 (1977).

91. Mulliken, R.S., J. Chem. Phys. 7, (1939) 20.
92. Zare, R.N. and Herschbach, D.R., J. Mol. Spectry. 15 (1965) 462.
93. Herzber, G. Spectra of Diatomic Molecules, 2nd ed. (Van Nostrand, Princeton, 1950).
94. Coulson, C.A., Valence, 2nd ed. (Oxford Univ. Press, London, 1961) pp. 139-141.
95. Eden, J.G., Appl. Phys. Lett. 33, 495 (1978).
96. Dkeu, N., Mazza, C., Chem Phys. Lett 46, 172 (1977).
97. Waynant, R.W., Eden, J.G., Appl. Phys. Lett. 33, 708 (1978).
98. Clementi, E. and Roetti, C., At. Nucl. Data Tables 14 (1974) 177.
99. Burke, V.M. and Grant, I.P., Proc. Phys. Soc. (London) 90 (1967) 297.
100. Herman, F. and Skillman, S., Atomic Structure Calculations (Prentice-Hall, Englewood Cliffs, 1963).
101. Lu, C.C., Carlson, T.A., Malik, F.B., Tucker, T.C. and Nestor, C.W., Jr., At. Data 3 (1971) 1.
102. Sharma, R.R., Phys. Rev. A13 (1976) 517.
103. Wieland, K., Helv. Phys. Acta 14 (1941) 420.
104. Duxy, C., Hyman, H.A., Chem. Phys. Lett. 52, 345 (1977).
105. Flannery, M.R., in Case Studies in Atomic Collision Physics 2, edited by E.W. McDaniel and M.R.C. McDowell, North Holland, Amsterdam 1972, p. 3.
106. Velazco, J.E., Kolts, J.H. and Setser, D.W., J. Chem. Phys. 65, 3468 (1976).
107. Flannery, M.R., J. Chem. Phys. 56, 143 (1978).
108. Parks, J.H., preliminary data unpublished.
109. Clyne, M.A.A. and Coxon, J.A., Proc. Rev. Soc. 298, 424 (1967).
110. Brown, W.G., Phys. Rev. 42, 355 (1932).

111. Brumer, P. and Karplus, M., J. Chem. Phys. 58, 3903 (1972).
112. Abrahamson, A.A., Phys. Rev. 178, 76 (1969).
113. Klein, M.M. and Breukener, K.A., Phys. Rev. 111, 1115 (1958).

DISTRIBUTION LIST

Office of Naval Research, Department of the Navy, Arlington, VA 22217 - Attn: Physics Program (1 copy)
 Naval Research Laboratory, Department of the Navy, Washington, D.C. 20375 - Attn: Technical Library (1 copy)
 Office of the Director of Defense, Research and Engineering, Information Office Library Branch, The Pentagon
 Washington, D.C. 20301 - (1 copy)
 U.S. Army Research Office, Box CM, Duke Station, Durham, N.C. 27706 - (1 copy)
 Defense Documentation Center, Cameron Station, Alexandria, VA 22314 - (1 copy)
 Defender Information Analysis Center, Battelle Memorial Institute, 505 King Avenue, Columbus, OH 43201 - (1 copy)
 Commanding Officer, Office of Naval Research Branch Office, 536 South Clark Street, Chicago, IL 60615 - (1 copy)
 New York Area Office, Office of Naval Research, 715 Broadway (5th Floor), New York, NY 10003 -
 Attn: Dr. Irving Rowe (1 copy)
 Air Force Office of Scientific Research, Department of the Air Force, Washington, D.C. 22209 - (1 copy)
 Office of Naval Research Branch Office, 1030 East Green Street, Pasadena, CA 91106 - Attn: Dr. Robert Behringer
 (1 copy)
 Defense Advanced Research Projects Agency, 1400 Wilson Blvd., Arlington, VA 22209 - Attn: Strategic Technology
 Office (1 copy)
 Office Director of Defense, Research and Engineering, The Pentagon, Washington, D.C. 20301 - Attn: Asst. Dir.
 (Space and Adv. Systems) (1 copy)
 Office of the Assistant Secretary of Def., System Analysis (Strategic Programs), Washington, D.C. 20301 -
 Attn: Mr. Gerald R. McNichols
 U.S. Arms Control and Disarmament Agency, Dept. of the State Bldg., Rm. 4931, Washington, D.C. 20451 Attn: Dr. Charles Henkin- (1 copy)
 Energy Research Development Agency, Division of Military Applications, Washington, D.C. 20545 - (1 copy)
 National Aeronautics and Space Admin., Lewis Research Center, Cleveland, Oh 44135 - Attn: Dr. John W. Dunning, Jr.
 Aerospace Research Engineer
 (1 copy)
 National Aeronautics & Space Admin., Code RR, FOB 10B, 600 Independence Ave., SW, Washington, D.C. 20546 - (1 copy)
 National Aeronautics and Space Admin., Ames Research Center, Moffit Field, CA 94035 - Attn: Dr. Kenneth W. Billman
 (1 copy)
 Department of the Army, Office of the Chief of RD&A, Washington, D.C. 20310 - Attn: DARD-DD (1 copy)
 Department of the Army, Office of the Chief of RD&A, Washington, D.C. 20310 - Attn: DAMA-WSM-T (1 copy)
 Department of the Army, Office of the Deputy Chief of Staff for Operations and Plans, Washington, D.C. 20310
 Attn: DAMO-RQD (1 copy)
 U.S. Army Missile Command, Research and Development Division, Redstone Arsenal, AL 35809 - Attn: Army High
 Energy Laser Programs (1 copy)
 Commanding Officer, U.S. Army Mobility Equipment R&D Center, Ft. Belvoir, VA 22060 - Attn: SMEFB-MW (1 copy)
 Commander, U.S. Army Armament Command, Rock Island, IL 61201 - Attn: AMSAR-RDT (1 copy)
 Director, Ballistic Missile Defense Adv. Technology Center, P.O. Box 1500, Huntsville, AL 35807 -
 Attn: ATC-O (1 copy)
 Director, Ballistic Missile Defense Adv. Technology Center, P.O. Box 1500, Huntsville, AL 35807 -
 Attn: ACT-T
 Commanding General, U.S. Army Munitions Command, Dover, NH 17801 - Attn: Mr. Gilbert F. Chesnov (AMSMU-R) (1 copy)
 Director, U.S. Army Ballistics Res. Lab., Aberdeen Proving Ground, MD 21005 - Attn: Dr. Robert Eichenberger (1 copy)
 Commandant U.S. Army, Air Defense School, Ft. Bliss, TX 79916 - Attn: Air Defense Agency (1 copy)
 Commandant, U.S. Army, Air Defense School, Ft. Bliss, TX 79916 - Attn: ATSA-CTD-MS (1 copy)
 Commanding General, U.S. Army Combat Dev. Command, Ft. Belvoir, VA 22060 - Attn: Director of Material,
 Missile Div. (1 copy)
 Commander, U.S. Army Training and Doctrine Command, Ft. Monroe, VA 23651 - Attn: ATCD-CF (1 copy)
 Commander, U.S. Army Electronics Command, Ft. Monmouth, NJ 07703, Attn: AMSEL-CT-L, Dr. R.G. Buser (1 copy)
 Commander, U.S. Army Combined Arms Combat Dev. Act., Ft. Leavenworth, KS 66027 - (1 copy)
 National Security Agency, Ft., Geo. G. Meade, MD 20755 - Attn: R.C. FOSS A763 (1 copy)
 Deputy Commandant - For Combat and Training Developments, U.S. Army Ordnance Center and School,
 Aberdeen Proving Ground, MD 21005 - Attn: ATSL-CTD-MS-R (1 copy)
 Department of the Navy, Office of the Chief of Naval Operations, The Pentagon 50739, Washington, D.C. 20350 -
 Attn: (OP 982F3)
 Boston Branch Office, Bldg. 114, Section D, 666 Summer Street, Boston, MA 02210 (1 copy)
 Department of the Navy, Deputy Chief of Navy Material (Dev.), Washington, D.C. 20360 -
 Attn: Mr. R. Gaylord (MAT 032B) (1 copy)
 Naval Missile Center, Point Mugu, CA 93042 - Attn: Gary Gibbs (Code 5352) (1 copy)
 Naval Research Laboratory, Washington, D.C. 20375 - Attn: Electro Optical Technology, Program Office,
 Code 1409 (1 copy)
 Naval Research Laboratory, Washington, D.C. 20375 - Attn: Dr. P. Livingston - Code 5560 (1 copy)
 Naval Research Laboratory, Washington, D.C. 20375 - Attn: Dr. A.I. Schindler - Code 6000 (1 copy)
 Naval Research Laboratory, Washington, D.C. 20375 - Attn: Dr. John L. Walsh - Code 5503 (1 copy)
 High Energy Laser Project Office, Department of the Navy, Naval Sea System Command, Washington, D.C. 20360 -
 Attn: Capt. A. Skolnick, USN (PM 22) (1 copy)
 Superintendent, Naval Postgraduate School, Monterey, CA 93940 - Attn: Library (Code 2124) (1 copy)
 Navy Radiation Technology, Air Force Weapons Lab (NLO), Kirtland AFB, NM 87117 (1 copy)
 Naval Surface Weapons Center, White Oak, Silver Spring, MD 20910 - Attn: Dr. Leon H. Schindel
 (Code 310) (1 copy)

DISTRIBUTION LIST (Continued)

Naval Surface Weapons Center, White Oak, Silver Spring, MD 20910 - Attn: Dr. E. Leroy Harris (Code 313) (1 copy)
 Naval Surface Weapons Center, White Oak, Silver Spring, MD 20910 - Attn: Mr. K. Enkenhaus (Code 034) (1 copy)
 Naval Surface Weapons Center, White Oak, Silver Spring, MD 20910 - Attn: Mr. J. Wise (Code 047) (1 copy)
 Naval Surface Weapons Center, White Oak, Silver Spring, MD 20910 - Attn: Technical Library (1 copy)
 U.S. Naval Weapons Center, China Lake, CA 93555 - Attn: Technical Library (1 copy)
 HQ AFSC/XRLW, Andrews AFB, Washington, D.C. 20331 - Attn: Maj. J.M. Walton (1 copy)
 HQ AFSC (DLCAW), Andrews AFB, Washington, D.C. 20331 - Attn: Maj. H. Axelrod (1 copy)
 Air Force Weapons Laboratory, Kirtland AFB, NM 87117 - Attn: LR (1 copy)
 Air Force Weapons Laboratory, Kirtland AFB, NM 87117 - Attn: AL (1 copy)
 HQ Aeronautical Systems Div., Wright Patterson AFB, OH 45433 - Attn: XRF - Mr. Clifford Fawcett (1 copy)
 Rome Air Development Command, Griffiss AFB, Rome, NY 13440 - Attn: Mr. R. Urtz (OCSE) (1 copy)
 HQ Electronics Systems Div. (ESL), L.G. Hanscom Field, Bedford, MA 01730 - Attn: Mr. Alfred E. Anderson (XRT) (1 copy)
 HQ Electronics Systems Div. (ESL), L.G. Hanscom Field, Bedford, MA 01730 - Attn: Technical Library (1 copy)
 Air Force Rocket Propulsion Lab., Edwards AFB, CA 93523 - Attn: B.R. Bornhorst, (LKCG) (1 copy)
 Air Force Aero Propulsion Lab., Wright Patterson AFB, OH 45433 - Attn: Col. Walter MOE (CC) (1 copy)
 Dept. of the Air Force, Foreign Technology Division, Wright Patterson AFB, OH 45433 - Attn: PDTN (1 copy)
 Commandant of the Marine Corps., Scientific Advisor (Code RD-1), Washington, D.C. 20380 (1 copy)
 Aerospace Research Labs., (AP), Wright Patterson AFB, OH 45433 - Attn: Lt. Col. Max Duggins (1 copy)
 Defense Intelligence Agency, Washington, D.C. 20301 - Attn: Mr. Seymour Berler (DTIB) (1 copy)
 Central Intelligence Agency, Washington, D.C. 20505 - Attn: Mr. Julian C. Nall (1 copy)
 Aircsearch Maunuf. Co., 9851-9951 Sepulveda Blvd., Los Angeles, CA 90009 - Attn: Mr. A. Colin Stancliffe (1 copy)
 Atlantic Research Corp., Shirley Highway at Edsall Road, Alexandria, VA 22314 - Attn: Mr. Robert Naismith (1 copy)
 Battelle Columbus Laboratories, 505 King Avenue, Columbus, OH 43201 - Attn: Mr. Fed Tietzel (STPIAC) (1 copy)
 Bell Aerospace Co., Buffalo, NY 14240 - Attn: Dr. Wayne C. Solomon (1 copy)
 Boeing Company, P.O. Box 3999, Seattle, WA 98124 - Attn: Mr. M.I. Gamble (2-460,MS 8C-88) (1 copy)
 Electro-Optical Systems, 300 N. Halstead, Pasadena, CA 91107 - Attn: Dr. Andrew Jensen (1 copy)
 General Electric Co., Space Division, P.O. Box 8555, Philadelphia, PA 19101 - Attn: Dr. R.R. Sigismonti (1 copy)
 General Electric Co., 100 Plastics Avenue, Pittsfield, MA 01201 - Attn: Mr. D.G. Harrington (Rm. 1044) (1 copy)
 Hercules, Inc., Industrial Dept., Wilmington, DE 19899 - Attn: Dr. R.S. Voris (1 copy)
 Hercules, Inc., P.O. Box 210, Cumberland, MD 21502 - Attn: Dr. Ralph R. Preckel (1 copy)
 Hughes Research Labs., 3011 Malibu Canyon Road, Malibu, CA 90265 - Attn: Dr. D. Forster (1 copy)
 Hughes Aircraft Co., Aerospace Group-Systems Division, Canoga Park, CA 91304 - Attn: Dr. Jack A. Alcalay (1 copy)
 Hughes Aircraft Co., Centinela and Teale Streets, Building 6, MS E-125, Culver City, CA 90230 -
 Attn: Dr. William Yates (1 copy)
 Institute for Defense Analyses, 400 Army-Navy Drive, Arlington, VA 22202 - Attn: Dr. Alvin Schnitzler (1 copy)
 Lawrence Livermore Laboratory, P.O. Box 808, Livermore, CA 94550 - Attn: Dr. R.E. Kiddle (1 copy)
 Lawrence Livermore Laboratory, P.O. Box 808, Livermore, CA 94550 - Attn: Dr. E. Teller (1 copy)
 Lawrence Livermore Laboratory, P.O. Box 808, Livermore, CA 94550 - Attn: Dr. Joe Fleck (1 copy)
 Los Alamos Scientific Laboratory, P.O. Box 1663, Los Alamos, NM 87544 - Attn: Dr. Keith Boyer (1 copy)
 Lockheed Palo Alto Research Lab., 3251 Hanover Street, Palo Alto, CA 94303 - Attn: L.R. Lunsford,
 Orgn. 52-24, Bldg. 201 (1 copy)
 Mathematical Sciences Northwest, Inc., P.O. Box 1887, Bellevue, WA 98009 - Attn: Dr. Abraham Hertzberg (1 copy)
 Massachusetts Institute of Technology, Lincoln Laboratory, P.O. Box 73, Lexington, MA 02173 -
 Attn: Dr. S. Edelberg (1 copy)
 Massachusetts Institute of Technology, Lincoln Laboratory, P.O. Box 73, Lexington, MA 02173 -
 Attn: Dr. L.C. Marquet (1 copy)
 McDonnell Douglas Astronautics Co., 5301 Bolsa Avenue, Huntington Beach, CA 92647 -
 Attn: Mr. P.L. Klevatt, Dept. A3-830-BBFO, M/Sq (1 copy)
 McDonnell Douglas Research Labs., Dept. 220, Box 516, St. Louis, MO 63166 - Attn: Dr. D.P. Ames (1 copy)
 Dr. Anthony N. Pirri, 30 Commerce Way, Woburn, MA 01801 (1 copy)
 Rand Corp., 1700 Main Street, Santa Monica, CA 90406 - Attn: Dr. C.R. Culp/Mr. G.A. Carter (1 copy)
 Raytheon Co., 28 Seyon Street, Waltham, MA 02154 - Attn: Dr. F.A. Horrigian (Res. Div.) (1 copy)
 Raytheon Co., Boston Post Road, Sudbury, MA 01776 - Attn: Dr. C. Sonnenschien (Equip. Div.) (1 copy)
 Raytheon Co., Bedford Labs, Missile Systems Div., Bedford, MA 01730 - Attn: Dr. H.A. Mehlhorn (1 copy)
 Riverside Research Institute, 80 West End Street, New York, NY 10023 - Attn: Dr. L.H. O'Neill (1 copy)
 Riverside Reserach Institute, 80 West End Street, New York, NY 10023 - Attn: Dr. John Bose (1 copy)

DISTRIBUTION LIST (Continued)

Riverside Research Institute, 80 West End Street, New York, NY 10023 - Attn: (HPEGL Library) (1 copy)

Rockwell International Corporation, Rocketdyne Division, Albuquerque District Office, 3636 Menaul Blvd.,
Ne, Suite 211, Albuquerque, NM 87110 - Attn: C.K. Kraus, MGR. (1 copy)

Sandia Corp., P.O. Box 5800, Albuquerque, NM 87115 - Attn: Dr. Al Narath (1 copy)

Stanford Research Institute, Menlo Park, CA 94025 - Attn: Dr. F.T. Smith (1 copy)

Science Applications, Inc., 1911 N. Ft. Meyer Drive Arlington, VA 22209 - Attn: L. Peckham (1 copy)

Science Applications, Inc., P.O. Box 328, Ann Arbor, MI 48103 - Attn: R.E. Meredith (1 copy)

Science Applications, Inc., 6 Preston Court, Bedford, MA 01703 - Attn: R. Greenberg (1 copy)

Science Applications, Inc., P.O. Box 2351, La Jolla, CA 92037 - Attn: Dr. John Asmus (1 copy)

Systems Science and Software, P.O. Box 1620, La Jolla, CA 92037 - Attn: Alan F. Klein (1 copy)

Systems Consultants, Inc., 1050 31st Street, NW, Washington, D.C. 20007 - Attn: Dr. R.B. Keller (1 copy)

Thiokol Chemical Corp., Wasatch Division, P.O. Box 524, Brigham City, UT 84302 - Attn: Mr. J.E. Hansen (1 copy)

TRW Systems Group, One Space Park, Bldg. R-1, Rm. 1050, Redondo Beach, CA 90278 - Attn: Mr. Norman Campbell (1 copy)

United Technologies Research Center, 400 Main Street, East Hartford, CT 06108 - Attn: Mr. G.H. McLafferty (1 copy)

United Technologies Research Center, Pratt and Whitney Aircraft Div., Florida R&D Center, West Palm Beach, FL 33402,
Attn: Dr. R.A. Schmidke (1 copy)

United Technologies Research Center, Pratt and Whitney Aircraft Div., Florida R&D Center, West Palm Beach, FL 33402,
Attn: Mr. Ed Pinsley

Varian Associates, EIMAC Division, 301 Industrial Way, San Carlos, CA 94070 - Attn: Mr. Jack Quinn (1 copy)

Vought Systems Division, LTV Aerospace Corp., P.O. Box 5907, Dallas, TX 75222 - Attn: Mr. F.G. Simpson, MS254142
(1 copy)

Westinghouse Electric Corp., Defense and Space Center, Balt-Wash. International Airport, Box 746,
Baltimore, MD 21203 - Attn: Mr. W.F. List (1 copy)

Westinghouse Research Labs., Beulah Road, Churchill Boro, Pittsburgh, PA 15235 - Attn: Dr. E.P. Riedel (1 copy)

United Technologies Research, East Hartford, CT 06108 - Attn: A.J. DeMaria (1 copy)

Aireborne Instruments Laboratory, Walt Whitman Road, Melville, NY 11746 - Attn: F. Pace (1 copy)

General Electric R&D Center, Schenectady, NY 12305 - Attn: Dr. Donald White (1 copy)

Cleveland State University, Cleveland, OH 44115 - Attn: Dean Jack Soules (1 copy)

Exxon Research and Engineering Co., P.O. Box 8 Linden, NJ 07036 - Attn: D. Grafstein (1 copy)

University of Maryland, Department of Physics and Astronomy, College Park, MD 20742 - Attn: D. Currie (1 copy)

Sylvania Electric Products Inc., 100 Ferguson Drive, Montian View, CA 94040 - Attn: L.M. Osterink (1 copy)

North American Rockwell Corp., Autonetics Division, 3370 Miraloma Avenue, Anaheim, CA 92803 -
Attn: R. Gudmundsen (1 copy)

Massachusetts Institute of Technology, 77 Massachusetts Avenue, Cambridge, MA 02138 - Attn: Prof. A. Javan (1 copy)

Lockheed Missile & Space Co., Palo Alto Research Laboratories, Palo Alto, CA 94304 - Attn: Dr. R.C. Ohlman (1 copy)

Polytechnic Institute of New York, Rt. 110, Farmingdale, NY 11735 - Attn: Dr. William T. Walter (1 copy)